Title
X-Ray Spectroscopy of Liquids and Interfaces

Author
Lam, Royce Ka-Jun

Publication Date
2017

Peer reviewed|Thesis/dissertation

X-Ray Spectroscopy of Liquids and Interfaces

by

Royce Ka-Jun Lam

A dissertation submitted in partial satisfaction of the

requirements for the degree of

Doctor of Philosophy

in

Chemistry

in the

Graduate Division

of the

University of California, Berkeley

Committee in charge:

Professor Richard J. Saykally, Chair
Professor Daniel M. Neumark
Professor Roger W. Falcone

Fall 2017

X-Ray Spectroscopy of Liquids and Interfaces

Abstract

X-Ray Spectroscopy of Liquids and Interfaces

by

Royce Ka-Jun Lam

Doctor of Philosophy in Chemistry

University of California, Berkeley

Professor Richard J. Saykally, Chair

The molecular structure of liquids and solutions and the behavior of solvated species, both in solution and at interfaces, play a vital role in a wide range of systems and phenomena. While much has been done to characterize these systems, significant advances are still needed to extend existing experimental methodologies to those which were previously inaccessible. For example, while the introduction of liquid microjets into soft X-ray spectroscopy enabled the study of liquids by this element-selective technique, studies of highly volatile liquids were impractical due to the high vapor background perturbing the liquid signal. The development of a new detection scheme, presented herein, enabled the studies of such systems. In this dissertation, I describe the development of new liquid microjet techniques, including a detailed study elucidating the mechanism of electrokinetic energy conversion, studies exploring the liquid structure of prototypical volatile liquids and binary mixtures, and hydration and interfacial fractionation in the aqueous carbonate system using soft X-ray absorption (XAS) and photoemission spectroscopy (XPS), as well as the development of a new interface-specific soft X-ray spectroscopy, soft X-ray second harmonic generation (SHG).

In Chapter 2, I detail the use of liquid microjet electrokinetics for energy conversion, exploring thermal energy as a pressure source, the mechanism of charge separation in the liquid microjets, and techniques for tuning the microjet properties through targeted use of surface coatings via silanization.

In Chapter 3, I investigate high vapor pressure liquids using liquid microjet XAS, focusing on the structure of liquid alkanes (n-nonane and n-decane). This study required the development of a new detection scheme, which significantly reduced the vapor contribution to the measured signal. The detection scheme employed a straightforward modification of our standard liquid microjet assembly and leveraged a detection methodology similar to that of the electrokinetic energy conversion experiments, wherein a signal can be detected both upstream and downstream of the point of charge separation.

In Chapter 4, water-alcohol mixtures are characterized by XAS, providing new insight into the hydrogen bonding environments, with methanol- and ethanol-water exhibiting appreciable differences to that of isopropanol-water. The measured spectra evidence a signifi-

cant enhancement of hydrogen bonding originating from the methanol and ethanol hydroxyl groups upon the addition of water. These additional hydrogen bonding interactions would strengthen the liquid-liquid interactions, resulting in additional ordering in the liquid structures and leading to a reduction in entropy and a negative enthalpy of mixing, consistent with existing thermodynamic data. In contrast, the spectra of the isopropanol-water mixtures exhibit an increase in the number of broken alcohol hydrogen bonds for mixtures containing up to 0.5 water mole fraction, an observation consistent with existing enthalpy of mixing data, suggesting that the measured negative excess entropy is a result of clustering or micro-immiscibility.

In Chapter 5, the aqueous carbonate system is investigated, characterizing the hydration environment by XAS and the interfacial fractionation of the species by XPS. Studying the aqueous carbonate system necessitated the development of a new fast-flow liquid microjet mixing system, which facilitated generation of short-lived species immediately prior to interaction with the X-ray probe. This advance permitted the continuous generation of aqueous carbonic acid through the protonation of bicarbonate in solution. The decomposition of the generated acid further enabled the characterization of dissolved CO_2 by XAS. Utilizing XPS, which exploits attenuation length of the emitted photoelectrons to achieve depth profiling, the relative fractionation of carbonate, bicarbonate, and carbonic acid at the liquid/vapor interface, finding that both carbonate and carbonic acid are present in higher concentrations than bicarbonate in the interfacial region – a surprising result as the concentration of the doubly charged, strongly hydrated carbonate anion was found to be enhanced relative to the singly charged, less strongly hydrated bicarbonate and in apparent contrast to current models for ion adsorption to hydrophobic interfaces.

In Chapter 6, the development of a new surface and interface sensitive soft X-ray spectroscopy, soft X-ray SHG, is detailed. The experimental results and accompanying first principles theoretical analysis highlight the effect of resonant enhancement and show the technique to be interfacially sensitive in a centrosymmetric sample, with second harmonic intensity arising primarily from the first atomic layer at the open surface. This technique and the associated theoretical framework demonstrate the ability to selectively probe interfaces, including those that are buried, with elemental specificity, thus providing a new tool for a range of scientific applications. Additionally, the transmission of the soft X-ray pulses from the FERMI free electron laser through carbon films of varying thickness was examined to quantify other nonlinear effects of high intensity pulses above and below the carbon K-edge.

To my friends and family

Contents

List of Figures

List of Tables

Acknowledgments

None of this would have been possible without Rich. WHILE, HE, TRIED, TO, TEACH, ME, MANY, THINGS,,, MOST, RELATING, TO, SCIENCE, SOME, STUFF, JUST, DIDN'T, STICK, LIKE, THE, PROPER, USE, OF, COMMA$$$$, AND CAPITALIZATION (THE GREEN LIGHT ON THE CAPS LOCK BUTTON = COMPUTER WORKING PROPERLY???)..... THANXXX $$$$$ RICH!!!!!!

In all seriousness though, I really do need to thank Rich. His seemingly endless enthusiasm for essentially everything non-administrative and his willingness to allow me to explore new ideas and projects made working for him incredible experience. I would also be remiss if I didn't thank Naomi Ginsberg, who pointed me in the direction of Rich's group when I was an undergraduate in her statistical mechanics class at Berkeley. I certainly wouldn't be where I am now if it wasn't for that.

Next, I would like to thank my fellow labmates in the Saykally group. All of you have always been around to answer all of potentially dumb questions and to distract me from doing actual work. Jacob and Orion who I worked with in the X-ray group. Tony, Chris, and Sumana who were not directly involved in the X-ray experiments at the ALS but helped with all of the beam time shifts without ever complaining about the strange and obnoxiously long work hours. If it weren't for your help beam times would have been especially miserable. As the X-ray project moved towards free electron laser experiments, you were there to answer all my questions related to nonlinear optics. Will who was always willing to go to lunch with me, Hikaru for being perfect replacement for Tony or, as Sumana would put it, "Tony 2.0 now 100% more Japanese," and Michael for always showing up and eating all of our food... all of the food.

The work presented here also would not have been possible without the many collaborators who contributed. The bulk of my experimental work was done at X-ray light sources (ALS and FERMI) where the staff play a significant role in the success of an experiment, working tirelessly to ensure our success as users. From the ALS – Wanli Yang, Jon Spear, Hendrik Bluhm, Osman Karslıoğlu, David Kilcoyne, Bruce Rude, Doug Taube, David Malone, and the rest of the general support staff. At FERMI, the list is longer than the number of people we met while there with many of them working late into the nights with us. Emiliano Principi, Laura Foglia, Alberto Simoncig, Marcello Coreno, Luca Giannessi who worked with us directly at the EIS-TIMEX beamline. Luca and his collaborators – Enrico Allaria, Giovanni De Ninno, Bruno Diviacco, Eleonore Roussel, Simone Spampinati, Giuseppe Penco, Simone Di Mitri, Mauro Trovò, and Miltcho Danailov – worked to keep the FEL running throughout our experiment in an entirely new configuration. Luca Poletto, Paolo Miotti, and Nicola Fabris installed, aligned, and tested the spectrometer used in the experiment. Our experiments would not have been successful without all of their efforts.

Calculations and a model developed in collaboration with Nadine Schwierz and Phill Geissler furthered our understanding of the electrokinetic energy conversion studies presented in Chapter 2. Computational support for the X-ray experiments has been provided by David Prendergast, Tod Pascal, and Das Pemmaraju at the Molecular Foundry. In our numerous

discussions, they have provided important insight and direction, in addition to the code support, for the analysis and also for planning future research directions. Tod and Das also invested a significant amount of time developing new methods for interpreting our X-ray SHG data.

Finally, I would like to thank my family and friends. To my parents, mom and dad, thank you for all of your support. To my sister, Joyce, and my cousins, Lisa and Charles, our annual trips to Disneyland is something I look forward to each year. We always end up with such entertaining pictures. To Simba, my four-legged niece, who has replaced me or Joyce as the favorite child. To my friends, without you these past few years would have been a lot less fun. The list below will be far from comprehensive, but know that it is not because I forgot anyone, just that I lost interest in writing...

This work was supported by the Office of Science, Office of Basic Energy Sciences, Division of Chemical Sciences, Geosciences, and Biosciences of the US Department of Energy at the Lawrence Berkeley National Laboratory under Contract No. DE-AC02-05CH11231. X-ray absorption and photoemission experiments were conducted at the Advanced Light Source, which is a DOE Office of Science User Facility. Calculations were performed as part of a User Project at the Molecular Foundry utilizing computational resources there and from the National Energy Research Scientific Computing Center (NERSC). The Molecular Foundry is supported by the Office of Science, Office of Basic Energy Sciences, and NERSC is a DOE Office of Science User Facility supported by the Office of Science of the U.S. Department of Energy. The soft X-ray SHG and TPA measurements were conducted at the EIS-TIMEX beamline at FERMI (Trieste, IT).

Chapter 1

Introduction

1.1 Electrokinetic Energy Conversion

Electrokinetic energy conversion in micro- and nano-fluidic devices has received significant attention in recent years. Such an effect can be observed by forcing water through a porous material or through well-defined micrometer or nanometer diameter channels [1–18]. The use of liquid microjet electrokinetics facilitates the direct conversion of hydrostatic pressure to electrical energy and hydrogen gas without interference from back conduction via electroosmotic flow. Conversion efficiencies of >10% have previously been reported using this approach [1, 2]. The hydrostatic pressure necessary for driving these liquid microjets can be generated from a number sources (e.g., mechanical pumps, gas pressure, thermal pressure, etc.). The development of the a thermally driven liquid microjet system is detailed in Chapter 2.1 [19].

Although it is widely recognized that the streaming current in these systems arise from the asymmetric distribution of anions and cations at an interfacial double layer, whether such a current in a pure water system results from the selective adsorption of hydroxide ions to a solid interface [1], or whether the electrostatic interactions of hydronium and hydroxide with surfaces charges might play an important role had yet to be addressed. This subject is elaborated in Chapter 2.2 wherein a modified Poisson-Boltzmann description, continuum hydrodynamic equations, and microjet electrokinetic experiments are employed to gain detailed insight into the origin of the streaming current produced using pure water [20].

The streaming current is found to originate from a combination of specific ion adsorption to the solid/liquid interface and long-ranged electrostatic interactions, with the latter dominating at charged interfaces. In fact, the portion of the streaming current resulting from specific ion adsorption amounts to only -1.8 pA, which is 3–4 orders of magnitude smaller than what is observed in a fused silica capillary.

This study also explored the use of targeted functionalization of the microjet surface via silanization to modify the surface charge density and surface hydrophobicity. Changing the

sign of the surface charge reverses the streaming current and switches between hydronium and hydroxide as the primary charge carrier. Similarly, tuning the surface coating to minimize the surface charges resulted in a significant decrease in the streaming current and can by exploited to minimize the interference from the streaming potential in liquid microjet X-ray and UV photoemission experiments [21–23]. Moreover, increasing the surface hydrophobicity was shown to reduce the energy loss from fluid/surface frictional forces, thereby increasing the conversion efficiency.

1.2 Liquid Microjet X-Ray Absorption and Photoemission Spectroscopy

The introduction of liquid microjets [24, 25] into soft X-ray absorption spectroscopy (XAS and EXAFS) by Wilson *et al.* enabled the windowless study of liquids by this powerful high vacuum methodology [26, 27]. Soft X-ray absorption spectroscopy is an element-specific probe that is sensitive to both the inter- and intramolecular environments, making it an ideal probe for studying liquid structure and ion solvation. Since its introduction, the Saykally Group has employed this methodology to study a wide variety of phenomena in liquid systems, including ion solvation and ion pairing in water [28, 29] and the solvation of the lithium ion in propylene carbonate, a prototypical battery electrolyte system [30].

In Chapters 3–5, I detail a new electrokinetic-based detection scheme enabling the use of liquid microjet technology with high vapor pressure liquids [31], a study of hydrogen bonding interactions in alcohol-water binary mixtures [32], and extended studies of the aqueous carbonate system, focusing on the solvation environment of carbonic acid and dissolved CO_2 and the use of liquid microjet X-ray photoemission spectroscopy (XPS) to characterize the relative fractionation of carbonate, bicarbonate, and carbonic acid at the vacuum/water interface [33–35].

While liquid microjet technology enabled the study of liquids via XAS, weakly interacting liquids produce large vapor backgrounds that strongly perturb the liquid signal. Consequently, many solvents (e.g., hydrocarbons, ethers, ketones, etc.) have been inaccessible by this technology. Using a straightforward modification to our standard liquid microjet setup and a detection scheme motivated by the electrokinetic energy conversion experiments described in Chapter 2, a new detection scheme, *upstream detection*, was designed to significantly attenuate the vapor background observed with standard total electron yield detection. In a water microjet, spectra measured using the upstream detection scheme exhibited a five-fold increase in the liquid/vapor signal; upstream detection was then successfully applied to the study of n-nonane and n-decane. This work is presented in Chapter 3.

In Chapter 4, water-alcohol binary mixtures are characterized via liquid microjet X-ray absorption spectroscopy at the oxygen K-edge. It is well established that non-ideal liquid-liquid binary mixtures can exhibit negative excess entropies of mixing, with water-alcohol mixtures being a prominent and extensively studied example. This effect in water-alcohol

mixtures was first characterized experimentally by Butler *et al.* in 1933 [36]; subsequently, a number of different models for the liquid structure have been proposed, ranging from enhanced hydrogen bonding around hydrophobic groups to microscopic immiscibility, without obtaining consensus [37–40]. In our work, mixtures of methanol-, ethanol-, and isopropanol-water were characterized using O K-edge XAS. The pre-edge region of the O K-edge spectrum of both water and the alcohols is associated with broken hydrogen bonds. Thus, examining changes to these features as a function of alcohol concentration provides valuable insight into the changes in liquid structure.

Chapter 5 details solvation of aqueous carbonate, bicarbonate, carbonic acid, and carbon dioxide and the relative fractionation of these species in the interfacial region by XAS and XPS, respectively. While carbonate and bicarbonate were previously characterized using XAS by England *et al.* [41], aqueous carbonic acid and dissolved CO_2 remained elusive. The short-lived nature of carbonic acid in solution ($t_{1/2} \approx 26$ ms) had previously precluded detailed studies of its solvation environment [42, 43]. In fact, despite carbonic acid being the centerpiece of the global carbon cycle and physiological buffer systems [44–49], there have only a few successful spectroscopic studies of the aqueous acid [42, 50, 51]. To study carbonic acid in solution, a new fast-flow mixing system was developed. This system, detailed in Section 5.1, exploits the rapid protonation of bicarbonate relative to the slower decomposition of carbonic acid to generate the neutral acid directly in solution, immediately prior to interaction with the X-ray beam. The implementation of this system in the aqueous carbonic acid study also enabled the characterization of dissolved CO_2 (Section 5.2) by XAS.

Using XPS (Section 5.3), relative fractionation of the of carbonate, bicarbonate, and carbonic acid are characterized finding that both carbonate and carbonic acid are present at higher concentrations than bicarbonate in the probed interfacial region. While the interfacial enhancement of a neutral acid relative to a charged ion is expected [52], the interfacial enhancement of the doubly charged, strongly hydrated carbonate anion over the singly charged, less strongly hydrated bicarbonate ion is surprising [53–55]. As vibrational sum frequency generation experiments have concluded that both carbonate and bicarbonate anions are largely excluded from the air/water interface [56–58], the results presented herein suggest that there exists a significant accumulation of carbonate below the depletion region, outside of the area probed by vibrational sum frequency generation.

1.3 Soft X-ray Nonlinear Spectroscopy

The development of ultrafast lasers capable of producing intense pulses has enabled the general study of matter by nonlinear spectroscopic methods [59]. While this field has heretofore been limited to optical wavelengths, extension to X-ray wavelengths could provide an element- and chemical-specific probe yielding vital new information [60, 61]. Specifically, the extension of second order nonlinear spectroscopies in the soft X-ray regime would enable a powerful new approach for surface and interface analysis with broad applicability. The recent development of new high peak power X-ray light sources, X-ray free electron lasers (FEL), has

extended the field of nonlinear effects to hard X-ray energies. At these energies, second- and third-order nonlinear spectroscopies, including second harmonic generation (SHG) [62], sum frequency generation (SFG) [63], two-photon absorption (TPA) [64], and inelastic Compton scattering [65], have been demonstrated. However, current hard X-ray FELs lack the longitudinal and temporal coherence necessary for efficiently satisfying the phase-matching conditions required for nonlinear spectroscopies, thus making the exploitation of some of these techniques very difficult [66, 67]. Furthermore, at hard X-ray wavelengths SHG and SFG can be generated even within centrosymmetric samples, effectively making the method a bulk, rather than interfacial, probe [68].

Using the FERMI free electron laser (FEL), a high intensity, highly coherent, soft X-ray light source base on high-gain harmonic generation (HGHG) of a longer wavelength seed laser, we performed the first demonstration of soft X-ray second harmonic generation experiment, exploiting the carbon K-edge on graphite films of varying thicknesses (Section 6.1) and demonstrating that the second harmonic signals exhibit no bulk volume dependence. Additionally, these first experiments showed that the SH response is highly sensitive to resonance effects. Simultaneous direct monitoring of the transmitted FEL beam also enabled characterization of other nonlinear effects (Section 6.2).

To interpret the X-ray SHG spectra, we adapted a first principles density functional theory (DFT) approach for calculating second-order nonlinear spectra in the X-ray regime. Our approach is broadly applicable for calculating electronic SHG and SFG spectra across a wide range of wavelengths. Using this approach, the SH response for graphite was calculated for an 8-layer slab. By isolating the signal from each layer to determine the exact degree of surface specificity, we show that the SH intensity in graphite arises from primarily from the first molecular layer and that $\sim$87% of the signal is generated from the first 2 layers. This result stands in stark contrast to traditional *surface specific* soft X-ray spectroscopies (i.e., X-ray absorption/photoemission spectroscopy), which effectively probe the first few nanometers of a sample as they are restricted by inelastic mean free paths of the photoelectrons or photoions.

This new spectroscopy provides a powerful new tool for characterizing the electronic properties of interfaces and surfaces, effectively combining the surface specificity of optical second-order nonlinear spectroscopy with the element-specificity of X-ray spectroscopy. This essentially enables X-ray absorption spectroscopy of just the first few molecular layers of an exposed bulk sample or either side of a buried interface. Additionally, as the laser pulses and the generated SHG signals remain fully coherent, it should be possible to combine this technique with existing lensless coherent imaging techniques [69] allowing for simultaneous monitoring of interfacial electronic structure and bulk structural properties of nanoparticles.

Chapter 2

Electrokinetic Energy Conversion

2.1 Thermally Driven Electrokinetic Energy Conversion with Liquid Water Microjets

The material in this section was reproduced, with permission, from: Lam, R. K.; Gamlieli, Z.; Harris, S. J.; Saykally, R. J. Thermally Driven Electrokinetic Energy Conversion with Liquid Water Microjets. *Chem. Phys. Lett.* **2015**, *640*, 172–174.

Introduction

As described in the 2014 US DOE Report, *The Water-Energy Nexus: Challenges and Opportunities* [70], cooling of thermoelectric power plants accounts for 40% of US freshwater usage and dissipates tremendous quantities (27 quads/year) of primary energy as waste heat due to fundamental inefficiencies in converting thermal energy to electricity; internal combustion engines generate similarly prodigious amounts of waste heat (21.3 quads/year). Devices for mitigating this energy loss employing thermoelectric conversion schemes (i.e., solid-state thermoelectric generators and thermophotovoltaics) exist, but typically require high operating temperatures. An interesting alternative is to exploit the large coefficient of thermal expansion of liquid water to utilize waste heat via the production of high hydrostatic pressures, which can, in turn, drive recently demonstrated electrokinetic energy conversion and hydrogen production processes in fast-flowing liquid microjets [1, 2].

Electrokinetic conversion of mechanical energy with liquid microjets and nanojets comprises a potentially important, but largely unexplored, technology. There have been numerous studies on producing electrokinetic currents by forcing water through both porous materials or individual channels [8–16, 18]. The electrokinetic streaming current originates from the overlap between the liquid flow profile and the charge distribution near the solid/liquid interface. The streaming current I_s generated by a circular channel can be described by the integral of the product of the velocity profile $v(r)$ and the charge density distribution $\rho(r)$

$$I_s = 2\pi R \int_0^R v(r)\rho(r)dr \tag{2.1}$$

where R is the channel radius and r is the distance from the channel wall [1, 2]. Typically, these experiments generate streaming currents by moving liquid from one reservoir to another through a porous membrane or a single channel by applying pressure to a single side. The direct connection between the two reservoirs introduces significant inefficiencies in the energy conversion due to back-conduction through the liquid [10, 17, 71]. More recently, Miljkovic *et al.* have demonstrated that water droplets jumping between hydrophobic and hydrophilic surfaces can attain a positive electrostatic charge and generate electrical power via a similar charge separation mechanism [72, 73].

The inefficiencies resulting from back-conduction through the liquid in the reservoir systems are eliminated when liquid jets are employed. Under the laminar flow conditions of this study, the streaming current can be described by

$$I_s = -8\pi R\varepsilon_0 K v\zeta \tag{2.2}$$

where ε_0 is the permittivity of free space, K is the dielectric constant of the liquid, v is the area-averaged flow velocity, and ζ is the zeta-potential [5]. Preliminary studies conducted at Berkeley have demonstrated a conversion efficiency >10% with a peak power of ∼6 mW in water flowing from a 10 μm inner diameter aperture under turbulent flow conditions [2] and have shown that the electrical energy production can be accompanied by simultaneous gaseous hydrogen generation [1]. Here, electrical efficiency η is calculated as electrical power divided by the input kinetic energy as a function of volumetric flow rate Q and the applied pressure differential ΔP

$$\eta = \frac{I_s^2 R_L}{Q\Delta P} \tag{2.3}$$

where R_L is the load resistance. In this construct, the efficiency of the system is decoupled from the efficiency of refilling and heating the cylinder which is dependent on a variety of factors (i.e., location of the water source, thermal conductivity of the reservoir, heat capacity of the reservoir, etc.). A patent has been issued for this concept and device design [74]. Using a similar system to drive a droplet beam into a region of high electric field, up to 48% efficiency has been reported for in the conversion of the liquid's kinetic energy to potential energy [75].

High pressures (>500 PSI) are required to force water through the microjets and generating these pressures substantially reduces the wall-plug efficiency. Here we address this problem by demonstrating that such pressures can easily be generated by exploiting water's relatively large volumetric thermal expansion coefficient ($a_v(20°\text{C}) = 2.07 \cdot 10^4\ K^{-1}$) and moderate bulk modulus ($K_T = 3.16 \cdot 10^5$ PSI). The resulting pressure change ΔP induced by the temperature increase ΔT can therefore be approximated by

$$\Delta P = a_v K_T \Delta T \tag{2.4}$$

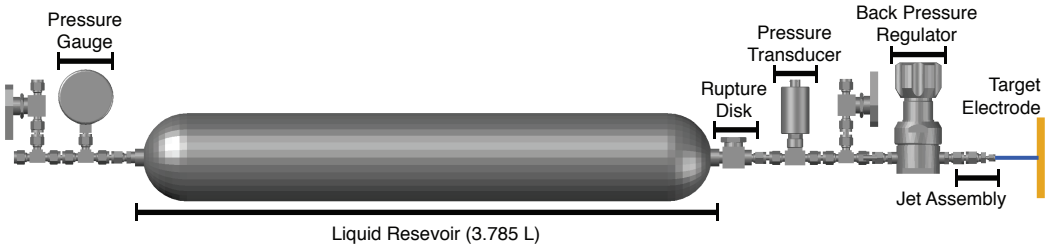

Figure 2.1: Schematic of the thermal electrokinetic microjet apparatus. The streaming current is collected at a copper target electrode placed ∼5 cm away from the silica capillary using a current amplifier.

For liquid water in a rigid container, we can therefore expect to generate 65.41 PSI/°C. Below we describe the design and construction of practical devices that can produce useful amounts of electricity while simultaneously generating hydrogen gas from flowing water, using simple passive thermal sources to produce the requisite high water pressures.

Experimental Design and Discussion

Figure 2.1 presents a schematic of the experimental configuration employed in this exploratory study. A 3.785 L double-ended stainless steel sample cylinder, filled with deionized water, is used for the liquid reservoir. In the current design, the sample cylinder limits the maximum pressure to below 1450 PSI. A digital pressure transducer (Heise Model DXD) provides pressure and temperature readings prior to the jet assembly, which has been described in detail previously in our recent electrokinetic energy conversion [1, 2] and interfacial ion affinity studies [76]. Briefly, the liquid microjet is produced by ejecting the pressurized water from a 30 μm inner diameter silica capillary rather than the Pt/Ir electron microscope apertures used in our previous energy conversion experiments. Silica capillaries were employed here due to their intrinsic chemical stability. However, due to the laminar flow profile and the significantly lower ζ potential of silica relative to that of the metal apertures, the electrokinetic conversion efficiency was not measured for this system. The liquid beam travels ∼5 cm in ambient air at average linear flow velocities of ∼20 m/s before impinging on a copper plate connected to an ammeter.

In order to maintain the necessary backing pressure, the temperature must slowly be increased as the water is expelled from the tank. The heating and liquid flow are controlled using a feedback loop which couples the heating element, the liquid flow as a function of pressure, and the tank pressure. In this scheme, the heating element is activated or deactivated when the pressure falls below 1200 PSI or rises above 1300 PSI, respectively. The back pressure regulator is set to open when the pressure rises above ∼1200 PSI. The current generated is monitored within this feedback loop. Internal temperature measurements are collected using a T-type thermocouple inserted into the center of the cylinder. The external temperature is measured using a digital temperature probe (Thorlabs TSP01). The cylinder

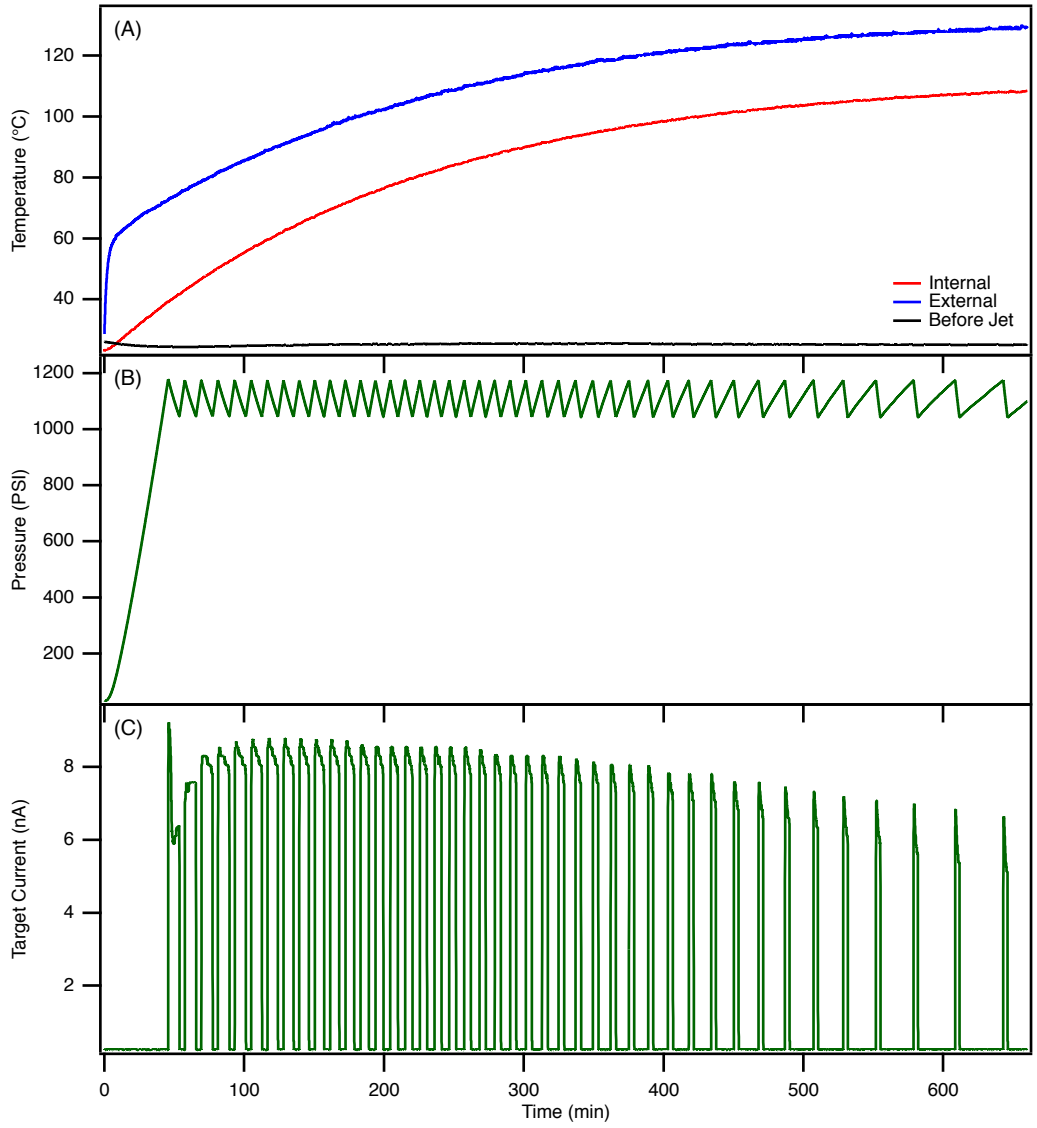

Figure 2.2: Typical data from a single experiment. (A) Internal (red), external (blue), and before jet (black) temperature vs. time. (B) Pressure vs. time. (C) Target current vs. time. All measurements were collected simultaneously with a time step of 1 s.

is heated resistively using a heating tape system coupled to a digital AC switch (CPS U-X3) and the system pressure. The generated current is measured using a current amplifier connected to the copper target electrode (FEMTO DDPCA-300). Instrument control and data acquisition are managed using Labview.

Figure 2.2 shows the temperature, pressure, and current measured for an individual experiment. The temperature (Figure 2.2A) is monitored in three different locations on the cylinder – internal (red), external (blue), and behind the silica capillary (black). During a

typical experiment, the initial liquid temperature is ∼25°C and ultimately reaches temperatures of above 100°C. The pressure generated from the heating is shown in Figure 2.2B. The sample cylinder is initially filled with deionized water at a backing pressure of ∼30–35 PSI and is allowed to reach a maximum pressure of ∼1350 PSI. The initial pressurization, defined as the time required to reach 1200 PSI, typically takes ∼50 min and requires a temperature change of ∼20°C (∼60 PSI/°C) which is in good agreement with our estimate from Equation 2.4. Figure 2.2C shows the current generated by the system as a function of time for a single experiment. The on/off behavior of the generated current is a direct result of the opening and closing of the back pressure regulator. In our present system, wherein the reservoir is not insulated, the pressure rise resulting from the heating does not keep pace with the pressure drop resulting from the liquid microjet. This can easily be corrected in practical situations.

Conclusions

We envision using EK power stations to supply or supplement power to buildings and devices, while concurrently employing hydrogen fuel cells that utilize the co-produced hydrogen. High pressures are required to drive water through the microjets, but such pressures (∼60 PSI/°C) can be obtained 'for free' (from waste heat sources) by taking advantage of water's large thermal expansion coefficient and heating it in a rigid (e.g., metal) chamber with solar energy or with waste heat. In this way, electrokinetic jets can work in tandem with more conventional thermoelectric devices, which typically require much higher temperatures for good efficiency [74].

2.2 Hydrogen and Electric Power Generation from Liquid Microjets: Design Principles for Optimizing Conversion Efficiency

The material in this section was reproduced, with permission, from: Schwierz, N.; Lam, R. K.; Gamlieli, Z.; Tills, J. J.; Leung, A.; Geissler, P. L.; Saykally, R. J. Hydrogen and Electric Power Generation from Liquid Microjets: Design Principles for Optimizing Conversion Efficiency. *J. Phys. Chem. C* **2016**, *120* (27), 14513–14521.

Introduction

Micro- and nano-fluidic devices have shown promise for energy conversion and have received significant attention over the last few years. For instance, electrokinetic currents can be produced by forcing water through porous materials or through well-defined micrometer- or nanometer-sized channels [1–18]. Liquid microjet electrokinetics allow for the conversion of hydrostatic pressure directly into electrical energy and molecular hydrogen, and also increase the conversion efficiency (>10%) by eliminating back conduction due to electroosmotic flow [1, 2]. Xie *et al.* have recently reported up to 48% efficiency in the conversion of kinetic energy to potential energy for a droplet train driven into a strong electric field [75].

It has long been recognized that streaming currents arise from the asymmetric distribution of anions and cations in an interfacial electric double layer. At charged interfaces, this double layer is formed from electrostatic interactions of the ions with the charged surface. Specific ion adsorption or repulsion at a solid/electrolyte interface also contributes to the asymmetric charge distribution, leading to anomalous ion-specific electrokinetic effects in uncharged channels [77]. However, the question of whether the streaming current in pure water results from the selective adsorption of hydroxide ions to a solid interface [1], or whether the electrostatic interactions of hydronium and hydroxide with surface charges might play an important role, has not yet been addressed.

We employ a combination of modified Poisson-Boltzmann (PB) theory, including non-electrostatic ion-surface interactions, continuum hydrodynamics, and microjet electrokinetic measurements to identify the origin of the streaming current. This approach identifies the contributions to the streaming current from long-ranged electrostatic interactions and specific adsorption of hydronium and hydroxide at the solid/liquid interface. At charged surfaces, the contribution from long-ranged electrostatic interactions results in streaming currents that are significantly larger than those induced by specific ion adsorption to uncharged interfaces. The detailed understanding afforded by this theory and the close match between the theoretical and the experimental results allows us to adjust surface properties and apparatus design to optimize power generation and conversion efficiency. In particular, targeted functionalization of the microjet surface via silanization is used to vary the surface charge density and the surface hydrophobicity. Changing the sign of the surface charge reverses the sign of the streaming current and switches between hydronium and hydroxide as the

primary charge carrier, and therefore between the production of molecular hydrogen or oxygen. Additionally, increasing the surface hydrophobicity reduces energy loss resulting from fluid/surface frictional forces, thereby increasing the conversion efficiency.

Methods

A. Streaming Current for Liquid Microjets

Electrokinetic streaming currents originate from the overlap between the fluid velocity profile with the charge distribution at solid/liquid interfaces. For a charged or biased surface, an electric double layer forms as counterions are attracted to the surface while similarly charged ions are repelled. In addition, specific ion adsorption or depletion at the interface contributes to the ionic distribution. The latter can lead to the formation of an electric double layer at an uncharged surface if the anions and the cations have unequal surface affinities and thereby induce ion-specific electrokinetic effects in uncharged channels. Quantitatively, the streaming current in a circular channel of radius R can be calculated from the integral of fluid velocity profile $v(z)$ and the net charge distribution $\rho(z)$

$$I = \int_0^R v(z)\rho(z)2\pi(R-z)\mathrm{d}z \tag{2.5}$$

where $z = R - r$ is the distance from the channel wall. The net charge density $\rho(z)$ is the sum of the individual ion number densities

$$\rho(z) = \sum_i q_i n_i(z) \tag{2.6}$$

In pure water, $n_i(z)$ corresponds to the number densities of hydronium and hydroxide from autoionization with a bulk concentration of 10^{-7} M. The distribution of the ions in the channel is obtained from the analytical solution of a modified Poisson-Boltzmann equation in a flat plane approximation, as detailed further below. Note that the liquid microjet employed in our experimental design breaks up into droplets (via Rayleigh instabilities) before reaching the target electrode thereby disrupting the system's electrical continuity and eliminating back conduction. Therefore, electroosmotic flow is not included in the present theoretical description.

In the following, we consider the two flow profiles that arise in our experimental designs, top hat flow and laminar flow. The characteristic length scale L_c over which flow profile develops is

$$L_c/(2R) \approx 0.06R_e \quad \text{(laminar flow)}, \quad L_c/(2R) \approx 4.4R_e^{1/6} \quad \text{(turbulent flow)} \tag{2.7}$$

where R_e is the Reynolds number – the ratio between the inertial forces to the viscous forces – defined as

$$R_e = \frac{2R\overline{v}\rho_W}{\eta_W} \tag{2.8}$$

where $\overline{v}$ is the average bulk velocity and ρ_W and η_W are the density and viscosity of water, respectively [78].

For our Pt/Ir aperture, a channel length L of 0.09–0.12 mm is insufficient for developing either completely turbulent or laminar flow at sufficiently high flow velocities. The velocity profile comprises a laminar sublayer close to the metal wall of thickness δz in which the fluid velocity increases linearly until it reaches the bulk fluid velocity [79, 80]. The resulting top hat velocity profile is given by

$$v_x(z) = \begin{cases} \overline{v}z/\delta z & \text{for } z < \delta z \\ \overline{v} & \text{otherwise} \end{cases} \tag{2.9}$$

with a laminar sublayer thickness $\delta z = 116RR_e^{-7/8}$. For our silica capillary channels, a channel length of 1–1.5 cm is sufficient for developing laminar flow. Under these conditions, the velocity profile is given by

$$v_x(z) = \frac{\Delta p}{4\eta_W L}(2Rz - z^2) \tag{2.10}$$

where Δp is the pressure differential between the inlet and outlet. In both cases, the average fluid velocity v follows from the volumetric flux

$$Q = v\Omega = \int_\Omega v(z)\mathrm{d}a \tag{2.11}$$

where Ω is the cross sectional area of the channels.

B. Streaming Current in the Limit of Large Diameter Channels ($\kappa R >> 1$)

If the channel diameter is large compared to the width of the electrostatic double layer ($\kappa R >> 1$), the streaming current can be approximated as

$$I = -4\pi v_0 \epsilon \zeta \quad \text{(laminar flow)}, \quad I = -\frac{2\pi \overline{v} \epsilon R \zeta}{\delta z} \quad \text{(top hat flow)} \tag{2.12}$$

where ζ is the zeta potential [79, 81]. Commonly, ζ is interpreted as the electrostatic potential at the shear plane – the position near the wall where the hydrodynamic flow velocity vanishes [82]. From here forward, we cease using the empirical description in terms of the zeta potential. Instead, we make use of the Navier boundary condition to quantitatively account for the effect of surface slippage on ion transport. Consequently, the fluid velocity results from a balance between the driving force induced by applying a pressure differential along the channel and the viscous frictional forces on the surface, as discussed in more detail below. Note that in pure water, the Debye length κ^{-1}, corresponding to the characteristic double layer thickness, is 0.974 μm. As a result, Equation 2.12 is only valid for channels much larger than employed in our current design or for higher bulk salt concentrations.

C. Slip Length and Surface Friction

The slip length l_b characterizes the hydrodynamic boundary condition of the fluid at the confining surface. It is defined by

$$l_b \partial_z v_x(z) = v_x(z) \tag{2.13}$$

where $v_x(z)$ is the tangential fluid velocity field [83]. The slip length is a measure of the friction of the fluid at the interface, where larger slip lengths are associated with lower surface friction. Experiments and theoretical predictions indicate that the slip length depends critically on the surface wettability measured by the water contact angle [84, 85]. Depending on surface hydrophobicity, typical values for the slip length range from a few tens of nanometers for hydrophobic surfaces to negative values of similar magnitude for hydrophilic surfaces. The negative slip length at hydrophilic surfaces is important for modeling surface conductivities when specific ion adsorption is considered [86]. As such, tuning the surface hydrophobicity provides an avenue for modifying the microfluidic and charge transport properties of a substrate. At a solid/water interface, the following relation between the water contact angle Θ and the slip length l_b has been obtained from atomistic MD simulations [84, 85]

$$l_b = 0.63\ nm \cdot (1 + \cos\Theta)^2 \tag{2.14}$$

Taking slippage effects into account by applying the Navier boundary condition (Equation 2.13) for laminar flow, yields

$$v(z) = \frac{\Delta p}{4\eta_W L}(2l_b R + 2Rz - z^2) \tag{2.15}$$

The dissipation associated with the fluid/solid friction is [87]

$$P_{\text{diss}} = \frac{128 Q^2 \eta L}{\pi(16R^4 + 64 l_b R^3)} \tag{2.16}$$

Increasing the slip length reduces energy dissipation and provides a major advantage when using large arrays of micro-channels for energy conversion or desalination. Moreover, in carbon nanotubes, the slip length can be two orders of magnitude larger than in other hydrophobic channels and even larger than the diameter of the nanotubes [88]. Miniaturization of our micro-channels toward nanometer sized channels is therefore especially promising as the energy dissipation scales inversely with the slip length.

D. Solution of the Linearized Poisson-Boltzmann Equation Including Specific Ion-Surface Interactions

The ionic distribution in the micro-channels is derived from a 1D modified Poisson Boltzmann equation [89, 90]. Ion-surface interactions are explicitly included by choosing square-well potentials for the interaction between the ions and the surface

$$V_i(z) = V_{i0}\Theta(b_i - z) \tag{2.17}$$

Here, V_{i0} corresponds to the ionic surface affinity for ions of type i, b_i is the interaction range, and $\Theta(b_i - z) = 1$ for $z < b_i$ and $\Theta(z) = 0$ otherwise. Since the full PB equation including specific ion adsorption can only be solved quasi-analytically [91], we have restricted the scope of our current model to small bulk salt concentrations and low ion-surface affinities. For $q\Phi \ll k_BT$, the PB equation can be linearized

$$\frac{d^2\Phi(z)}{dz^2} = -\sum_i \frac{q_i c_{i0} a_i(z)}{\epsilon}\left(1 - \frac{q_i\Phi(z)}{k_BT}\right) = \kappa'(z)^2\Phi(z) - J(z) \tag{2.18}$$

where z is the distance perpendicular to the interface, q_i is the charge of ions of type i, c_{i0} the bulk salt concentration for ionic species i, $\Phi(z)$ the local electrostatic potential, and ϵ the dielectric constant of water. Ion-specificity is accounted for by $a_i(z) = e^{-V_i(z)/k_BT}$ which depends on the ion-surface potentials $V_i(z)$ that are, in general, different for cations and anions. Assuming identical interaction ranges for cations and anions, $b^+ = b^- = b$, Equation 2.18 can be solved piecewise in regions I and II corresponding to the regions of finite or vanishing ion-surface interaction. The modified inverse Debye screening length κ' is defined as

$$\kappa'(z)^2 = \frac{1}{\epsilon k_BT}\sum_i q_i^2 c_{i0} a_i(z) = \begin{cases} \kappa_I^2; & z < b \\ \kappa_{II}^2; & z > b \end{cases} \tag{2.19}$$

and the parameter J is defined as

$$J(z) = \frac{1}{\epsilon}\sum q_i c_{i0} a_i(z) = \begin{cases} J_I; & z < b \\ J_{II}; & z > b. \end{cases} \tag{2.20}$$

Equation (2.18) can be integrated twice yielding

$$\frac{1}{\kappa'}\left(\ln(2(-J + \kappa'^2\Phi + \kappa'\sqrt{C_1 - 2J\Phi + \kappa'^2\Phi^2} + K_2))\right) = z \tag{2.21}$$

where C_1 and K_2 are the integration constants. The solution must satisfy the following boundary conditions (BC):

$$\text{(i)} \qquad \left.\frac{d\Phi_I(z)}{dz}\right|_{z=0} = \Sigma \tag{2.22}$$

$$\text{(ii)} \qquad \left.\frac{d\Phi_{II}(z)}{dz}\right|_{z=R} = 0 \tag{2.23}$$

$$\text{(iii)} \qquad \left.\frac{d\Phi_I(z)}{dz}\right|_{z=b} = \left.\frac{d\Phi_{II}(z)}{dz}\right|_{z=b} \tag{2.24}$$

$$\text{(iv)} \qquad \Phi_I(z)|_{z=b} = \Phi_{II}(z)|_{z=b} \tag{2.25}$$

with $\Sigma = -\sigma/\epsilon$ where σ is the surface charge density. The matching conditions (iii) and (iv) are used to provide a continuously differentiable potential at b. The electrostatic potential is thereby defined as

$$\Phi_I(z) = \frac{1}{4\kappa_I^2}\left(C_{2I}e^{-\kappa_I z} - 4e^{-\kappa_I z}\Sigma\kappa_I + 4J_I + C_{2I}e^{\kappa_I z}\right) \tag{2.26}$$

$$\Phi_{II} = \frac{(e^{\kappa_{II}(2R-z)}C_{2II} + 4J_{II} + C_{2II}e^{\kappa_{II}z})}{4\kappa_{II}^2} \tag{2.27}$$

Note that for large channels, the potential vanishes and Equation 2.27 reduces to $\Phi_{II}(z) = C_{II}^{DH}e^{-\kappa z}$. Applying the boundary conditions yields

$$C_{2I} = -\frac{-4\kappa_{II}^2 e^{-\kappa_I b}\Sigma\kappa_I + 4\kappa_{II}^2 J_I - \kappa_I^2 e^{-\kappa_{II}(-2R+b)}C_{2II} - 4\kappa_I^2 J_{II} - \kappa_I^2 C_{2II}e^{\kappa_{II}b}}{\kappa_{II}^2(e^{-\kappa_I b} + e^{\kappa_I b})} \tag{2.28}$$

$$C_{2II} = \frac{4(\kappa_{II}^2 e^{-\kappa_I b}J_I - e^{-\kappa_I b}\kappa_I^2 J_{II} + 2\kappa_{II}^2 e^{-\kappa_I b}\Sigma\kappa_I e^{\kappa_I b} - e^{\kappa_I b}\kappa_{II}^2 J_I + e^{\kappa_I b}\kappa_I^2 J_{II})}{\kappa_I((\kappa_I-\kappa_{II})e^{2\kappa_{II}R-\kappa_{II}b-\kappa_I b} - (\kappa_I\kappa_{II})e^{2\kappa_{II}R-\kappa_{II}b+\kappa_I b} + (\kappa_I+\kappa_{II})e^{-b(\kappa_I-\kappa_{II})} - (\kappa_I-\kappa_{II})e^{b(\kappa_{II}+\kappa_I)})} \tag{2.29}$$

The concentration profiles of the ith ionic species is calculated from

$$c_i(z) = c_{i0}a_i(z)\,(1 - q_i\Phi(z)/k_BT) \tag{2.30}$$

with the bulk ion concentration c_{i0}.

E. Parameterization of Specific Interactions of Hydronium and Hydroxide with a Channel Surface

Specific ion adsorption at a hydrophobic surface has been shown to accurately explain experimental data for long-ranged interactions between silica surfaces in different salt solutions [92, 93]. As such, we have used the abundant data for the interfacial tension at the air/water interface to parameterize the interfacial affinity of hydronium and hydroxide at water/silica interface, thereby capturing the ionic excess and the partitioning of the ions in the interfacial region. Within a mean field approximation, the interfacial tension can be written in terms of the electrostatic potential and the ionic concentration as

$$\begin{aligned}\Delta\gamma \quad (V_0^{\pm}, c_0) &= \int_0^{\infty}\left[\frac{1}{2}(c^+(z) - c^-(z))q\Phi(z)\right]dz \\ + \quad k_BT &\int_0^{\infty}\left[c^+(z)\ln\frac{c^+(z)}{c_0} + c^-(z)\ln\frac{c^-(z)}{c_0} + \Delta c(z)\right]dz \\ + \quad &\int_0^{\infty}\left[V^+(z)c^+(z) + V^-(z)c^-(z)\right]dz\end{aligned} \tag{2.31}$$

where the first integral is the electrostatic energy, the second integral represents the ideal mixing entropy of a dilute solution of anions and cations, and the last integral accounts for the ion-surface interaction [91, 94, 95]. However, the free energy expression (Equation 2.31) that is used here does not directly yield the relation between the electrostatic potential and the ionic densities via minimization, as the two fields depend implicitly on each other

via the Poisson-Boltzmann equation. Note that the expression used is more convenient for our analytical solution than the expression from Borukhov *et al.* [94, 95], and can be applied here as both the potential and the densities are known. Approximating $\ln \frac{c^+(z)}{c_0} \approx \ln a_\pm(z) - q\Phi/k_BT$ yields a closed form expression for the free energy per unit area. From this expression, the ion-surface interaction strength $V^\pm$ is chosen such that it reproduces the experimental air/electrolyte surface tension for a 100 mM solution (Figure 2.3) [96]. We have chosen the interfacial binding affinity of chloride as the reference ($V^{\mathrm{Cl}^-} = 0$). This choice is motivated by vanishing ion specific electrokinetic effects in NaCl solutions [77]. The corresponding binding affinity for the cation V^+ is then determined from relationships represented in Figure 2.3. The interaction range for anions and cations is chosen to be $b^+ = b^- = 1$ nm, based on the results from molecular dynamics simulations [91, 97]. In our model, H_3O^+ is slightly surface accumulated (with surface binding affinity $V^+ = -0.11\ k_BT$), while OH^- is weakly excluded ($V^- = +0.08\ k_BT$). While the partitioning of hydronium and hydroxide at the air/water interface has been actively debated in recent literature [98], our model is in agreement with the salt partitioning model for the air/water interface by Pegram and Record [99], classical and *ab initio* molecular dynamics simulations [100–102], non-linear spectroscopic studies [103, 104], and X-ray photoelectron spectroscopy measurements [105]. Conversely, the preferential adsorption of hydroxide to the air/water interface has been suggested by electrophoresis [106], titration [107], and mass spectrometry measurements [108]. Some theoretical studies have also indicated that the difference between the surface propensities of hydronium and hydroxide is small [109].

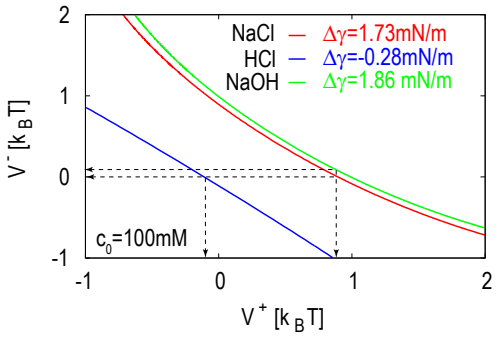

Figure 2.3: Optimal values for anion- and cation-surface interaction strength $V^\pm$. The lines correspond to the combination of V^+ and V^- that reproduces the experimental air/electrolyte surface tension for 100 mM bulk salt concentration (given as inset). The arrows indicate our choice of ion-surface interaction parameters with chloride as reference ($V^{\mathrm{Cl}^-} = 0$).

F. Electrokinetic Apparatus

The microjet electrokinetics apparatus used here has been described in previous publications [1, 2, 76]. Briefly, a high pressure liquid chromatography (HPLC) pump drives the liquid through PEEK tubing into a 30 μm inner diameter fused silica capillary. Electrokinetic currents were measured both upstream, through the stainless steel fitting which holds the capillary, and downstream, via a copper target electrode, using Keithley 428 and FEMTO DDPCA-300 current amplifiers. Water, with a resistivity of 18.2 MΩ·cm, used in the experiments was obtained from a Millipore purification system. Glassware was acid cleaned regularly with a Nochromix/sulfuric acid solution and rinsed with purified water.

G. Jet Coatings

The fused silica capillary tubing was functionalized using commercially available organosilanes. Trimethoxy(octadecyl)silane (ODS) [Technical Grade, 90%] and (3-Aminopropyl)triethoxysilane (APTES) [99%] were obtained from Sigma-Aldrich. N,N-didecyl-N-methyl-(3-trimethoxysilylpropyl)-ammonium chloride (DDMAC) [40-42% in methanol] and octadecyldimethyl(3-trimethoxysilylpropyl)-ammonium chloride (DMOAP) [60% in methanol] were obtained from Gelest. The capillary tubing was cut to $\sim$1.5 cm and soaked in solutions of $\sim$20 mM total organosilane concentration in toluene for 2–4 hours. To facilitate the reaction, a small amount of water was added to the mixtures. The capillaries were then removed from solution and baked for $\sim$6 hours at 140°C.

Results and Discussion

In this work, we investigate electrokinetic streaming currents generated from water flowing through micrometer-sized channels by combining a modified Poisson-Boltzmann description and continuum hydrodynamic equations with results from micro-fluidic experiments. Figure 2.4A summarizes our current understanding of the origin of a streaming current in a negatively charged channel. For the silica and PtIr channels used in the experiments, the negative surface charge arises from the dissociation of the silanol or metal oxide groups in water. In pure water, the streaming current originates from charge separation between hydronium and hydroxide. At the negatively charged walls, a pronounced double layer is formed, with a thickness of $\sim$1 μm. Hydronium is attracted to the interface while hydroxide is repelled (Figure 2.4B). The distribution of the ions is dominated by long-ranged electrostatic interactions with the charged channel walls, while non-electrostatic ion-surface interactions play only a minor role due to the low surface affinities of hydronium and hydroxide ($V^+ = -0.11$ $k_\mathrm{B}T$, $V^- = +0.08$ $k_\mathrm{B}T$). Consequently, the electrostatic potential is negative and decays exponentially with increasing distance from the channel walls (Figure 2.4C). The charge flux, resulting from the overlap between the net charge density and the laminar flow profile (Figure 2.4D), originates in the double layer region, in which the distribution of hydronium and hydroxide is unequal, and extends several microns into the channel due to the low screening

in pure water (Figure 2.4E). As a result of the extended double layer, hydronium is preferentially sheared away. At the target electrode, the unbalanced protons extract electrons to produce molecular hydrogen, as confirmed in our previous work [1]. The excess hydroxide in the reservoir discharges at the upstream nozzle connected to the reservoir and generates oxygen (Figure 2.4A).

Figure 2.4F, G show the dependence of the streaming current on the average flow velocity obtained from experiments under top hat and laminar flow conditions (data points) compared to the theoretical predictions using the surface charge density as the only adjustable parameter (lines). The resulting values for the surface charge density and electrostatic surface potential are summarized in Table 2.1. Our results are in good agreement with those measured for silica by Behrens *et al.* [110].

Table 2.1: Surface properties of the microchannels: Material, surface charge density σ, and surface potential Φ_0 based on our theoretical model. A reference to the experimental data used for the prediction is given in the last column.

material	flow condition	diameter [μm]	σ [e/nm^2]	Φ_0 [V]	reference
PtIr	top hat	5–19.1	-0.001 ± 0.0002	-0.22 ± 0.04	[1, 2]
Silica	laminar	30	$-0.00067 \pm 2.7 \cdot 10^{-5}$	-0.15 ± 0.006	current work
Silica	-	-	-0.00055 to -0.00083	-	[110]

Under top hat flow conditions, the streaming current scales as $v^{15/8}$ in the limit where $\kappa R >> 1$, while under laminar flow, the streaming current increases linearly with v. This provides a method for discriminating between different flow conditions. Overall, our theoretical model provides an excellent description of the experimental results under different flow conditions for small channels with low ionic strength ($\kappa R \approx 1$). Moreover, the model provides detailed insight into the ionic distribution and the electrostatic potential (Figure 2.4), and can be used to predict the surface charge density and the surface potential. Note, however, that the analytical description is limited to $q\Phi << k_\mathrm{B}T$. To accurately estimate the charge density of highly charged surfaces, numerical solutions of the full PB equation should be applied. In the following, we therefore restrict the discussion to low surface charge densities, wherein an analytical solution for the streaming current exists. This solution permits modeling of the influence of the surface and electrolyte properties over a wide range of parameters, which is essential to deriving the design principles necessary for maximizing power and hydrogen generation. In particular, we focus on the effect of the electrolyte concentration, the magnitude and sign of the surface charge density, the channel diameter, and the surface hydrophobicity under laminar flow conditions.

Figure 2.5A shows the streaming current's dependence on the ion concentration. At small ion concentrations, the streaming current has a plateau that scales as $I \propto R\sigma v$ in the limit of vanishing ion concentration. The current is maximized if the double layers from each side of the channel overlap and the full cross section of the channel contributes to charge separation. With increasing ion concentration, the double layer and therefore the region

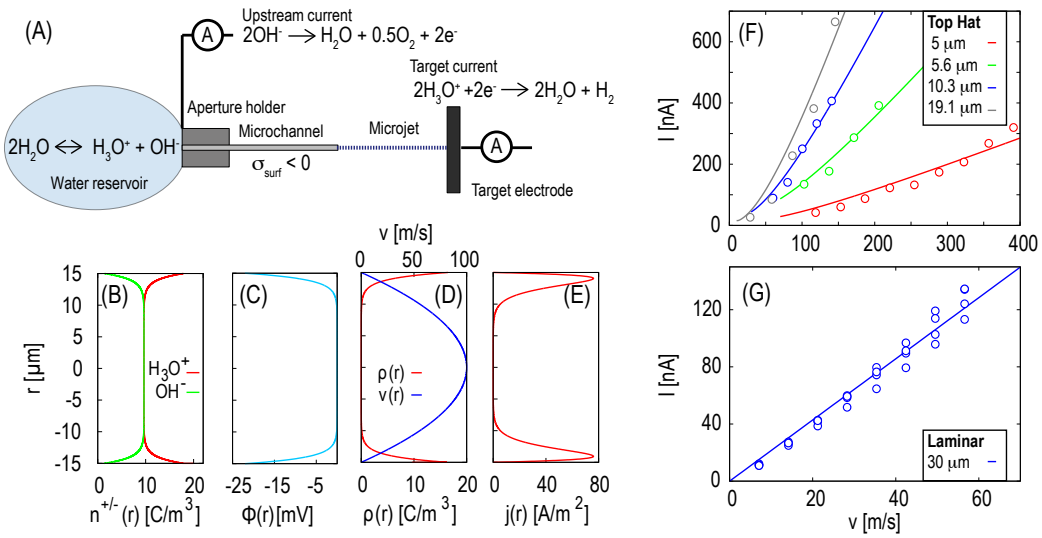

Figure 2.4: (A) Experimental design of the liquid microjet electrokinetics apparatus. (B) Density profiles of hydronium and hydroxide in pure water for a 30 μm channel with bare surface charge density $\sigma = -0.0001$ e/nm^2. (C) Electrostatic potential. (D) Charge density and flow velocity profile for laminar flow. (E) Charge flux $j(r) = \rho(r)v(r)$. (F) Streaming current as function of the average flow velocity for top hat flow and different PtIr channel diameters from electrokinetic measurements (open circles, adapted from [1, 2] discarding data points that are not in the regime of top hat flow) and theoretical predictions (lines). (G) Streaming current for laminar flow in a 30 μm silica channel from experiments (open circles) and theory (lines).

that contributes to the streaming current decreases due to increased screening. At large ion concentrations, where the screening length is on the order of the non-electrostatic ion-surface interaction range, specific ion adsorption at the channel walls becomes important. Here, excess adsorbed hydronium at the channel walls results in a surface charge reversal from negative to positive. As a result, hydroxide ions are attracted to the channel walls and form a second adsorption peak (data not shown). In this case, both hydronium and hydroxide ions are sheared away, leading to a slightly negative streaming current ($\sim$5 nA) due to the predominant flux of hydroxide ions. Moreover, at an uncharged surface in pure water under standard conditions (with bulk concentration $c_0 = 10^{-7}$ M of hydronium and hydroxide), the streaming current resulting from specific adsorption amounts to -1.8 pA (Figure 2.5B). This ion-specific anomalous streaming current is closely related to the electroosmotic flow at uncharged hydrophobic channels in sodium iodide solutions [77]. The contribution to the streaming current from specific adsorption of hydronium and hydroxide to an uncharged surface is minor. However, it can become important for strong ion-surface interactions at charged surfaces, as will be discussed further below. For a small negative surface charge ($\sigma = 1.2 \cdot 10^{-8}$ e/nm^2), the effect of preferential hydronium adsorption can be exactly

canceled (point of zero charge). Beyond this point, the streaming current is positive and increases linearly with increasing negative surface charge. The situation is reversed if the sign of the surface charge density is reversed. In this case, the streaming current is negative, since hydroxide is attracted to the positively charged channel walls and sheared away preferentially, leading to oxygen production at the target electrode.

Figure 2.5C shows the dependence of the current on the channel size. Similar to the results for top hat flow (Figure 2.4F), the streaming current increases with increasing channel size at a given flow velocity. The dashed line indicates a frequently used approximation in the limit $\kappa R >> 1$ [81].

In addition to electrical and hydrogen generation, our apparatus can be used to detect small changes in surface properties resulting from the selective interaction of different ions with surfaces in ultra-dilute solutions [76]. In Figure 2.5D, we show the effects of adding 0.1 nM anions and cations with surface affinity $V_S^{\pm}$ while maintaining a constant concentration of hydronium and hydroxide. The streaming current is affected only for ion-surface interactions much larger than the thermal energy $k_{\mathrm{B}}T$. Strong anion adsorption creates a higher effective surface charge and therefore generates greater charge separation and a larger streaming current. Strong cation adsorption, on the other hand, reduces the effective surface charge density and therefore decreases the streaming current. For instance, the addition of 0.1 nM KCl leads to a 10% reduction in the streaming current [76]. This corresponds to a cation affinity of about $V_S^{+} = 12\ k_{\mathrm{B}}T$, which is similar in magnitude to the non-electrostatic affinity of cations to carboxylate surface groups [111]. Consequently, ultra-dilute experiments allow us to estimate the affinity of cations to the surface silanol groups. The affinity of the ions for the undissociated silica surface groups is too weak ($<10\ k_{\mathrm{B}}T$) to affect the streaming current at such low salt concentrations [91].

In addition to surface charge and channel dimensions, the hydrophobicity of the channel walls play an important role for the energy conversion efficiency. While the former conditions mainly influence the ionic distribution, the surface hydrophobicity has a direct influence on the hydrodynamic flow profile. On small scales, the hydrodynamic boundary conditions deviate from the usual non-slip boundary condition. Assuming that the surface stress is linearly related to the surface velocity leads to the slip length shown schematically in the inset of Figure 2.6A [112]. Increasing the surface slip by increasing the hydrophobicity enhances the flow rate through small channels, offering the possibility of reducing dissipation due to fluid/surface friction (Equation 2.16). This increases the energy conversion efficiency ε, defined as the ratio between the output and the input power. For pressure driven flow, ε is given by

$$\varepsilon = \frac{I \nabla \psi}{Q \Delta p} \tag{2.32}$$

where $\nabla\psi$ is the voltage gradient. Figure 2.6A shows the streaming current as a function of the water contact angle or the slip length (Equation 2.14). The increase in the energy conversion efficiency for constant input pressure is shown in 2.6B. For the micron sized channels, the conversion efficiency can be increased by a factor of 1.4 using hydrophobic surface coatings as confirmed by our experiments (Figure 2.7). A further increase in the conversion

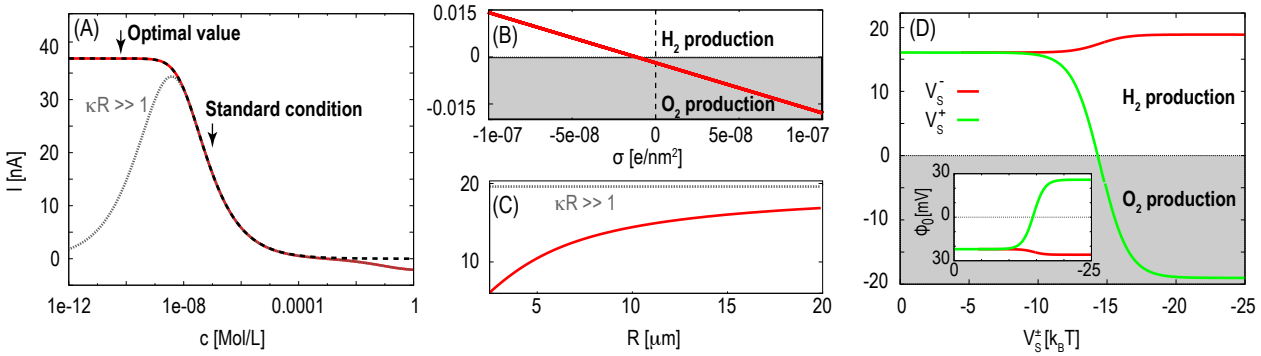

Figure 2.5: Streaming current (nA) as function of different parameters for a 30 μm channel with an average flow velocity $v = 50$ m/s. Unless otherwise stated, the channel has a surface charge density of $\sigma = -0.0001$ e/nm^2: (A) Streaming current dependence on the bulk ion concentration (red line). The dotted line indicates the limit in which the electric double layers do not overlap (large channels). The dashed line is the result for neglecting specific ion adsorption at the liquid/solid interface. (B) Streaming current dependence on the surface charge density. The value of the anomalous streaming current for uncharged channels is -1.8 pA. (C) Streaming current dependence on the channel radius. The dotted gray line indicates the frequently used approximation in the limit $\kappa R >> 1$ (Equation 2.12). (D) Streaming current dependence on the anion or cation ion-surface affinity $V_S^{\pm}$ for a 0.1 nM salt solution The electrostatic surface potential Φ_0 is shown in the inset. Gray areas indicate reversal of the sign of the streaming current leading to oxygen production at the target electrode.

efficiency could become possible by using nano-fluidic channels that are comparable in size to the slip length [87].

Guided by the theoretical predictions, we have employed surface coatings to vary the surface charge density and surface hydrophobicity of the channels. The results are shown in Figure 2.7 for a 30 μm channel. Reversal of the surface charge density and the sign of the streaming current is achieved by coating with APTES and DDMAC. Additionally, in agreement with the theoretical predictions, the streaming current increases with enhanced surface hydrophobicity. The ODS and DDMAC coatings are both terminated with long alkyl chains and thereby significantly reduce the hydrophilicity of the silica substrate. These two coatings significantly enhance the streaming current relative to that of their hydrophilic counterparts – uncoated silica (46.3%) and APTES (49.3%). Finally, a 0.6:0.4 mixture by mole ratio of DMOAP:ODS significantly reduces the surface charge density and therefore results in a much smaller streaming current.

Conclusions

In this work, we study electrokinetic streaming currents generated from water flowing through micron sized channels, focusing on modifications of surface properties with the goal

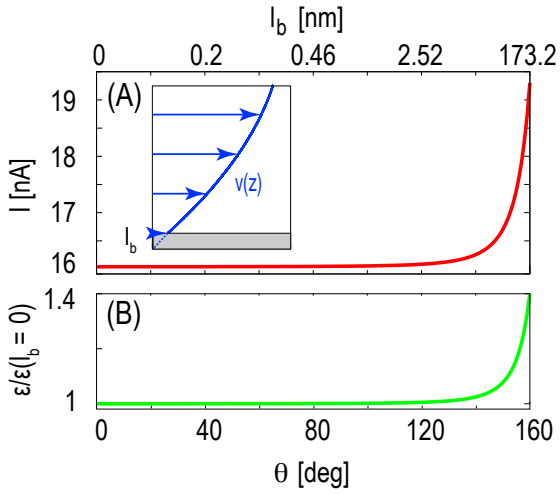

Figure 2.6: (A) Streaming current as function the surface hydrophobicity measured by the water contact angle Θ or the slip length l_b for constant input pressure. The inset shows a sketch of the slip velocity next to an interface. The slip length l_b corresponds to the distance wherein the linear extrapolation of the velocity profile reaches zero. (B) Efficiency increase by increasing the surface hydrophobicity at constant input pressure for a 30 μm channel with surface charge density of $\sigma = -0.0001$ e/nm^2.

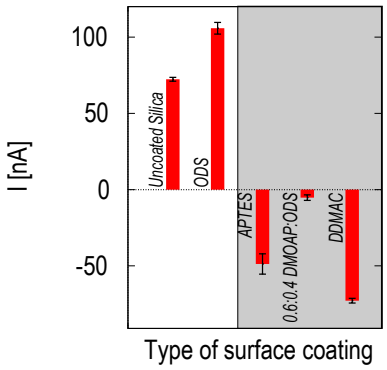

Figure 2.7: Streaming currents measured for surface coatings of varying surface charge density and surface hydrophobicity: Coating with ODS results in a negatively charged hydrophobic surface and increases the streaming current. The APTES and DDMAC coatings result in positively charged surfaces and reversal of the sign of the streaming current. The 0.6:0.4 DMOAP:ODS significantly reduces the surface charge and thereby results in a large reduction in the streaming current. The gray area indicates reversal of the sign of the streaming current.

of increasing the energy conversion efficiency. The combination of a Poisson-Boltzmann description, continuum hydrodynamics, and microjet electrokinetic experiments provides detailed insight into the contribution of electrostatic and non-electrostatic interactions to the streaming current. Specific adsorption of hydronium and hydroxide leads to anomalous ion-specific electrokinetic effects at *uncharged* surfaces, resulting in a streaming current of $\sim$1.8 pA. This non-electrostatic contribution is negligible when compared to the contribution of long-ranged electrostatic interactions at *charged* surfaces which result in streaming currents that are orders of magnitude larger (10–100 nA). In a negatively charged channel, the streaming current originates from the extended double layer formed by the preferential adsorption of hydronium to the solid/liquid interface. This more detailed model revises that suggested by Duffin *et al.*, which proposed that hydroxide was preferentially adsorbed to the channel walls [1, 2]. This previous model neglected to account for the channel's negative surface charge density. Specific ion adsorption becomes important for ions with high surface affinity ($V_S \gg k_B T$), and the interfacial affinity can be quantified using ultra-dilute salt solutions.

Tuning the surface properties of the channel, via silanization, provides a method for reversing the surface charge, thereby reversing the sign of the streaming current and switching between hydronium or hydroxide as the main charge carrier. Similarly, tuning the surface coating such that the surface charges are are minimized results in a significant reduction in the streaming current, an effect that can be exploited to minimize interference by the streaming potential in liquid microjet X-ray and UV photoemission spectroscopy experiments [21–23]. Moreover, increasing the surface hydrophobicity provides an avenue for increasing the energy conversion efficiency by reducing dissipation from fluid/surface friction. In particular, using carbon nano-tubes that are known to have an extremely large slip length could increase the current to a multiple of its current levels. However, generating a hydrostatic pressure differential at such small scales may prove challenging.

Chapter 3

Electrokinetic Detection of X-Ray Spectra of Weakly Interacting Liquids: n-Decane and n-Nonane

The material in this chapter was reproduced, with permission, from: Lam, R. K.; Shih, O.; Smith, J. W.; Sheardy, A. T.; Rizzuto, A. M.; Prendergast, D.; Saykally, R. J. Electrokinetic Detection for X-Ray Spectra of Weakly Interacting Liquids: N-Decane and N-Nonane. *J. Chem. Phys.* **2014**, *140* (23), 234202.

Introduction

The introduction of liquid microjets [24, 25] into soft X-ray absorption spectroscopy (XAS) by Wilson *et al.* enabled applications to liquids [27]. Prior to this, soft XAS was restricted to ultra-high vacuum surface physics and gas phase studies. This methodology has since enabled the measurement of Resonant Inelastic X-ray Scattering (RIXS) [113, 114] and Resonant Photoemission (RPE) [115, 116] spectra of liquids, which provide complementary data to XAS. The use of liquidmicrojets also facilitates the study of liquids without attendant radiation damage, which can be a serious limitation. However, a gas phase background, resulting from the vapor jacket surrounding the liquid jet, is always present. This background is usually small relative to the primary liquid signal, comprising less than 10% of the total signal detected for aqueous samples, such that a straightforward subtraction of the gaseous signal is typically sufficient. However, weakly interacting liquids (e.g., hydrocarbons) have faster evaporation rates under high vacuum conditions that generate more extensive vapor jackets around the microjets, precluding meaningful characterization of the liquids. Total Electron Yield (TEY) [28, 116–121], Total Ion Yield (TIY) [122, 123], and Total Fluorescence Yield (TFY) [124–127], which comprise the most common detection schemes for XAS of liquid microjets, are all sensitive to the vapor background. New experimental modalities or new detection methods are therefore necessary to enable the study of weakly interacting liquids, which are important solvents in many chemical and biochemical contexts [128–131].

This vapor background issue can potentially be addressed through the use of liquid flow cells, which have recently been used in XAS studies of a wide variety of systems [132–134]. These flow cells separate the liquid from the high vacuum environment through the use of silicon nitride windows. However, in the soft X-ray region, the windows attenuate the incoming X-ray beam, resulting in a significant reduction in signal, and they severely limit the study of nitrogen-containing compounds. Moreover, fluorescence detection must be used to detect the already-reduced signal and for low Z atoms, such as carbon, nitrogen, and oxygen, X-ray fluorescence is not the dominant de-excitation pathway [135, 136]. Instead, the Auger process, which results in the ejection of electrons, is heavily favored as the core-level de-excitation process. Therefore, it is usually preferable to detect via electron yield – especially when probing low Z atoms.

The use of liquid microjets in XAS provides important advantages over other existing methods for the study of liquids. This approach allows for windowless coupling to the X-ray synchrotron source, which ensures that the photon flux is not attenuated prior to interaction with the liquid. The microjet also provides a dynamic, rapidly renewed (microsecond residence times) sample which effectively eliminates sample damage. The signal generated by the impinging X-ray beam can then be detected via TEY, TIY, or TFY. To reduce or eliminate the vapor background attending the use of liquid microjets, new detection techniques, motivated by optogalvanic [137, 138] and electrokinetic [1, 2, 76] detection methods have been explored by our group. A schematic diagram of a typical microjet electrokinetics experiment is presented in Figure 3.1A. A more detailed description of the microjet electrokinetics experiment has been published previously [1, 2, 76]. Briefly, the current generated via charge separation at the microjet orifice can be detected both upstream, via back-conduction through the liquid, and downstream, on a target electrode. Analogously, we demonstrate in the present study that the X-ray absorption signal can be detected upstream of the impinging X-ray beam by measuring the magnitude of the charge present in the liquid jet following the removal of the ionized electrons by a positively biased electrode. Detecting downstream, while possible, proved to be impractical upon testing. The charge present in the liquid is proportional to the number of observed absorption events; hence, the method constitutes a novel type of *action spectroscopy* for core-level spectroscopy.

Materials and Methods

A. Sample Preparation

Water of 18.2 MΩ·cm resistivity was obtained from a Millipore purification system. n-Nonane and n-decane with stated purity of at least 99% were obtained commercially from Alfa Aesar. Samples were used without further purification.

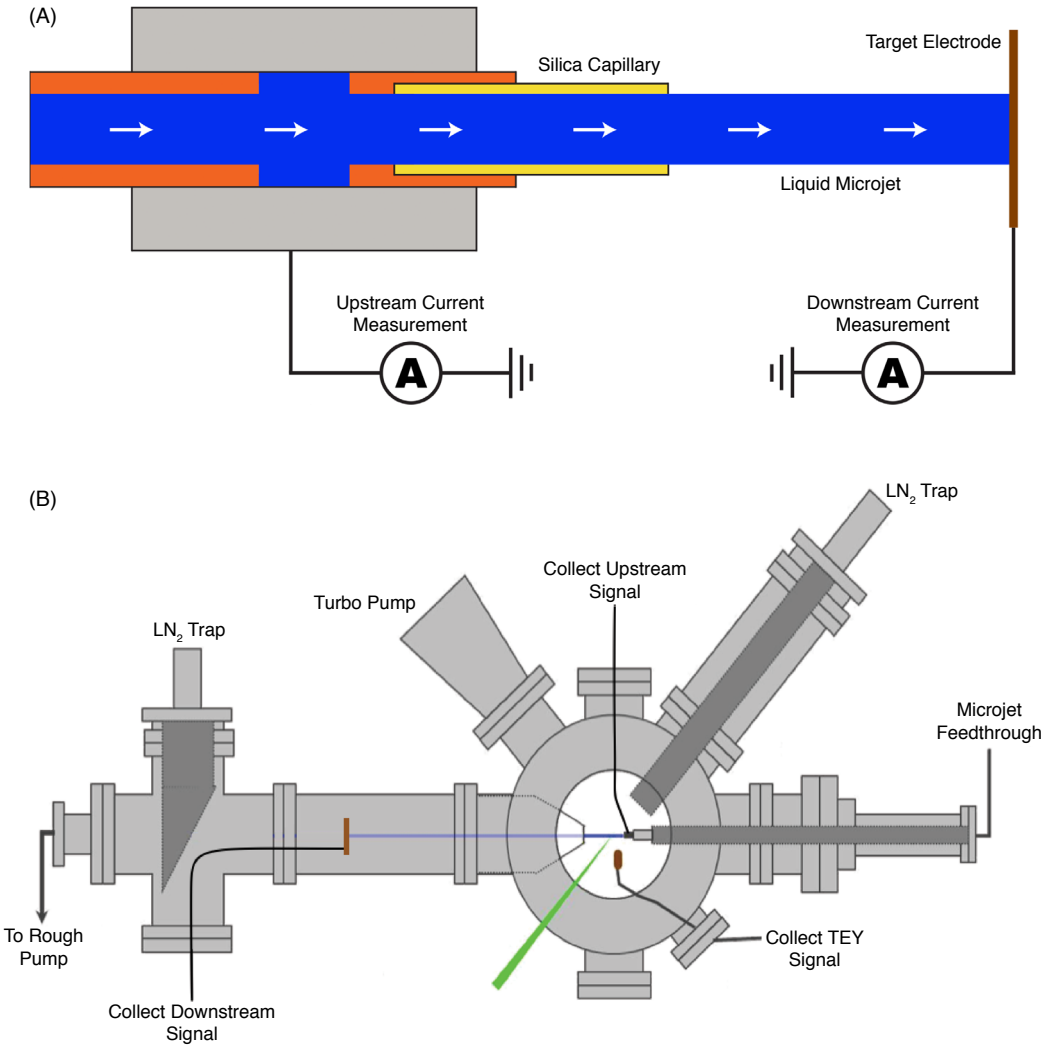

Figure 3.1: Experimental schematics. (A) Schematic of microjet electrokinetics experiment. Streaming current can be simultaneously collected at the target electrode and upstream of the point of charge separation via back conduction. (B) *Downstream detection*: A heated metal plate was placed between the skimmer and liquid nitrogen trap. The downstream signal is collected concurrently with the TEY signal. *Upstream detection*: The standard silica capillary is replaced with a 50 μm stainless steel TaperTip. The upstream signal is detected via the metal capillary concurrently with the TEY signal. Upstream and downstream detection schemes were not used concurrently. previously.

B. Experimental Design

Oxygen and carbon K-edge TEY, downstream, and upstream spectra were collected at Beamline 8.0.1 at the Advanced Light Source (ALS) at Lawrence Berkeley National Laboratory. A detailed description of the X-ray experiment has been published previously [117]. Minor changes were made to accommodate the new downstream and upstream detection methods. Briefly, an intense ($>10^{11}$ photons/s), high resolution ($E/\Delta E = 7000$), and tunable soft X-ray beam is generated from an undulator at the ALS. The beam is then focused (100×35 μm spot size) onto a liquid jet. A syringe pump (Teledyne-ISCO 260D) drives the liquid through fused capillary tubing with a 30–50 μm inner diameter, creating a liquid jet with linear flow velocities in the range 1–200 m/s that is intersected with the X-ray beam in a high vacuum ($\sim 2 \cdot 10^{-4}$ Torr) chamber. The liquid beam then passes through a skimmer and freezes onto a cryogenic trap. A TEY signal is collected with a positively biased (2.1 kV) copper electrode located $\sim$1 cm above the liquid sample as a function of photon energy. Vapor phase TEY spectra were collected by positioning the liquid microjet above or below the incident X-ray beam. The recorded spectra were normalized to the current (I_0) collected from a gold mesh located further up the beamline to account for X-ray intensity variations.

To facilitate the new detection modalities, a straightforward modification was applied to our experimental endstation [117]. A schematic representation of the modified experimental design is shown in Figure 3.1B. To enable the indirect detection of core-level absorption spectra downstream of the incident X-ray beam, a stainless steel target electrode, with an attached DC Peltier heater to prevent freezing, was placed between the skimmer aperture and the cryogenic trap. Current from the target was collected simultaneously with the TEY signal. To collect spectra upstream of the incident X-rays, the usual fused silica capillary is replaced with a 50 μm stainless steel TaperTip (New Objective). A wire is connected from the metal nozzle to a current amplifier (FEMTO DDPCA-300) to collect the upstream signal. The upstream spectrum is acquired simultaneously with the TEY spectrum. Simultaneous detection with TEY is essential to both the upstream and the downstream detection schemes. The removal of the ionized electrons by the positively biased electrode results in a positively charged liquid jet. The magnitude of the positive current can then be measured both upstream or downstream of the incident X-ray beam. The exact mechanism of conduction through the resistive liquid for the upstream detection is presently undetermined although induction is likely. Upstream and downstream signals were not collected concurrently.

C. Simulations and Calculations

Gromacs 4.6.4 [139–143] was used to perform classical NVT MD simulations of both gas phase and liquid n-decane. The gas phase system contained a single decane molecule in a cubic box of edge 30.000 Å and the liquid system contained 30 molecules of decane in a periodic cubic box of edge 21.280 Å. The simulations employed a modified OPLS-AA [144–146] forcefield developed by Siu *et al.* [147]. Following an initial minimization, the liquid system was heated to 298 K and then equilibrated for 500 ps under constant pressure to a

final density of 0.736 g/ml. An NVT simulation was then run for 2 ns. For the gas phase system, an NVT simulation was run immediately following heating to 298 K. The molecular configuration of each system was collected every 20 ps for use in the spectral simulation.

To calculate the X-ray absorption spectrum, atomic coordinates were taken from the final snapshot of the NVT simulation of liquid decane and from 10 uncorrelated snapshots of the single molecule NVT simulation for gas phase decane. The core-level excitation linestrengths were calculated with the eXcited electron and Core Hole (XCH) density functional theory approach [148]. The electronic structure was calculated using the plane wave self consistent field (PWSCF) code from the Quantum ESPRESSO package [149]. The exchange correlation energy was estimated with the Perdew-Burke-Ernzerhof (PBE) exchange correlation functional within the generalized gradient approximation [150]. A plane wave basis set with periodic boundary conditions and a kinetic energy cut-off of 25 Ry was used to model the localized and delocalized states. In the XCH approach, the lowest core-hole excited state is explicitly treated. The resulting self-consistent field was used to generate higher excited states non-self consistently. Transition amplitudes were then calculated within the single-particle and dipole approximations. The calculated transitions are broadened by Gaussian convolution of 0.1 eV full width half maximum. The energy axis was aligned relative to the experimentally collected vapor phase spectra of decane and a similarly calculated spectrum for a single decane molecule. Isosurfaces were calculated with Quantum ESPRESSO and rendered in VESTA [151].

Results and Discussion

Detecting the signal downstream of the incident X-rays, while possible, proved to be problematic. The addition of the DC heater to mitigate freezing in the high vacuum environment resulted in the crystallization of solutes onto the target. This led to a rapid degradation in the target electrode conductivity and the ability to detect changes in the charge carried by the liquid jet. Additionally, the natural breakup of the liquid jet due to Rayleigh instabilities [152, 153] and evaporation in the vacuum chamber often prevented the charged liquid from reaching the target electrode. Due to these issues, downstream detection of the X-ray signal as a method of reducing the vapor background was deemed impractical.

Detecting the X-ray absorption signal upstream of the impinging X-rays proved to be a more viable approach. By using a metal capillary as the detection electrode, the issues that arose from the downstream detection, freezing on the target electrode, crystallization of dissolved solutes, and vaporization of the liquid jet prior to detection, were entirely eliminated. The upstream detection scheme was first tested on the well-studied liquid water system [27, 154] and then on liquid nonane and liquid decane. These weakly interacting, long-chain liquid hydrocarbons are not typically considered to be highly volatile liquids, but since they exhibit high evaporation rates under high vacuum conditions, they essentially behave as such. As a result, in previous attempts to measure X-ray absorption spectra of liquid long-chain alkanes using microjets, only vapor phase spectra were collected. Figure 3.2 compares the oxygen K-edge core-level spectra of liquid water collected via both TEY

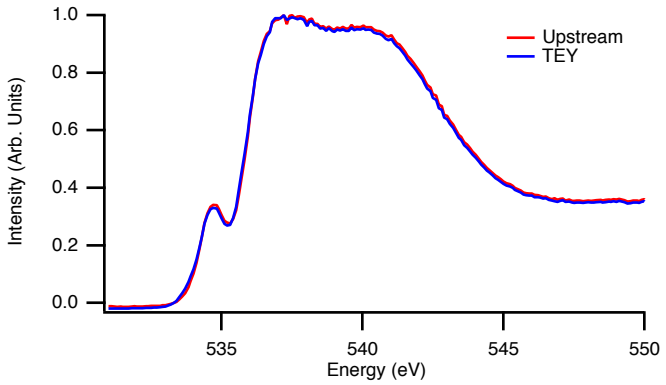

Figure 3.2: Oxygen K-edge absorption spectra for 25°C liquid water measured simultaneously with TEY and upstream detection. Spectra have been normalized to the peak maxima for direct comparison.

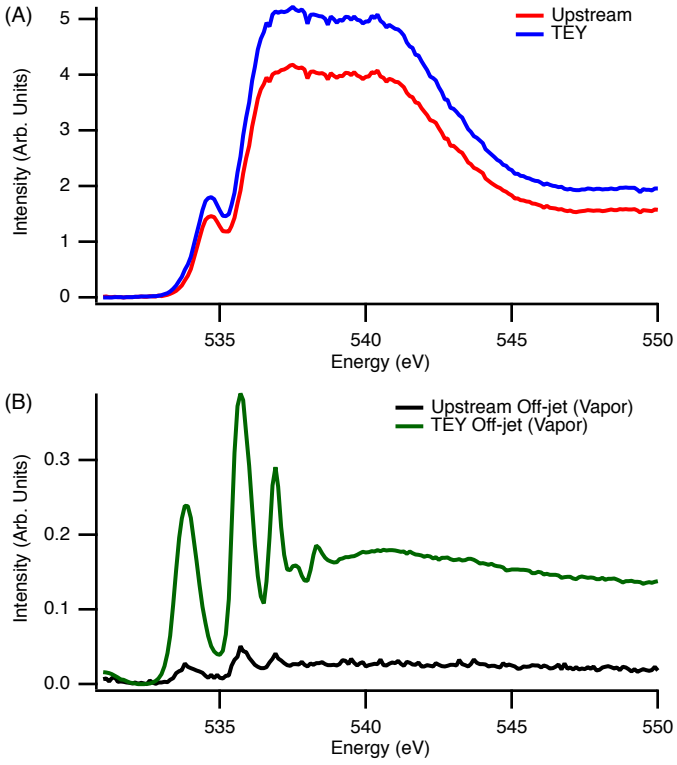

Figure 3.3: Unnormalized oxygen K-edge absorption spectra for 25°C water measured simultaneously with TEY and upstream detection. (A) On-jet (liquid) spectra; (B) off-jet (vapor) spectra. The off-jet signal originates from the liquid microjet vapor jacket.

and upstream detection. The spectra are normalized to the intensity of the strongest peak to facilitate direct comparison. As expected, due to the thin vapor jacket surrounding the water jet, the on-jet spectrum of liquid water is identical for the two detection methods. However, comparison of the unnormalized liquid (on-jet) and vapor (off-jet) spectra, shown in Figure 3.3, reveals a significant difference in the two detection schemes. While the upstream detection exhibits only a slightly reduced sensitivity to the signal originating in the liquid, it exhibits a significantly reduced sensitivity to the signal from the microjet vapor jacket.Overall, there is a five-fold increase in the liquid/vapor signal contrast in the upstream spectrum and similar signal-to-noise ratios when compared to TEY detection. The ∼20% decrease in the signal intensity in the upstream spectrum is likely a result of the inefficiencies in the mechanism of charge transfer back through the liquid.

In prior attempts to measure X-ray absorption spectra of liquid hydrocarbons using liquid microjets with TEY, shown in Figure 3.4A, the area normalized on-jet and off-jet spectra appeared essentially identical, whereas for strongly interacting liquids, like water and methanol, the liquid-phase spectrum is distinctly different from that of the gas and solid phases [27, 155, 156]. The anticipated broadening and spectral changes normally associated with the transition from the gas phase to the liquid phase spectrum were not observed in the hydrocarbon TEY spectra shown above. There are two possible explanations for this invariance between the liquid and vapor spectra observed previously. The first is that there genuinely is no difference between the gas phase and condensed phase spectra. Liquid hydrocarbons interact primarily through dispersion and weak electrostatic forces [147, 157–159]. It is possible that these interactions are simply not strong enough to exert an observable influence on the energy levels of the unoccupied orbital states of the molecule that are probed in the X-ray experiment. However, the increased density in the liquid phase should result in inhomogeneous, collisional broadening that should be clearly evident in the liquid spectrum at the high resolution of the present X-ray experiments. A more likely explanation for the similarities between the previously measured absorption spectra is simply that the signal arising from the vapor surrounding the microjet overwhelms the on-jet TEY spectrum. Liquid nonane exhibits an evaporation rate in a high vacuum environment that is significantly greater than those of the typical systems studied using liquid microjets (primarily aqueous solutions and alcohols) [25, 160]. The faster evaporation rate thus leads to a higher local vapor pressure surrounding the microjet and thus a larger vapor signal component in the on-jet spectrum.

Because the upstream detection method is much less sensitive to the signal originating from the vapor jacket, it can more effectively sample the genuine liquid phase spectra of samples with high local vapor pressures. Newly detected carbon K-edge X-ray absorption spectra of liquid nonane and decane are shown in Figures 3.4B and 3.4C. The spectra shown have been area normalized to allow for the comparison of peak intensity changes and shifts between the liquid and vapor phase. In these newly obtained spectra, clear differences are apparent between the on-jet (upstream and TEY) and the off-jet (TEY) vapor signal. In the on-jet (liquid) spectra, the feature centered near 292 eV is significantly broadened (FWHM: 2.13 eV for vapor; 4.25 eV for TEY; 5.45 eV upstream for decane) and slightly blueshifted

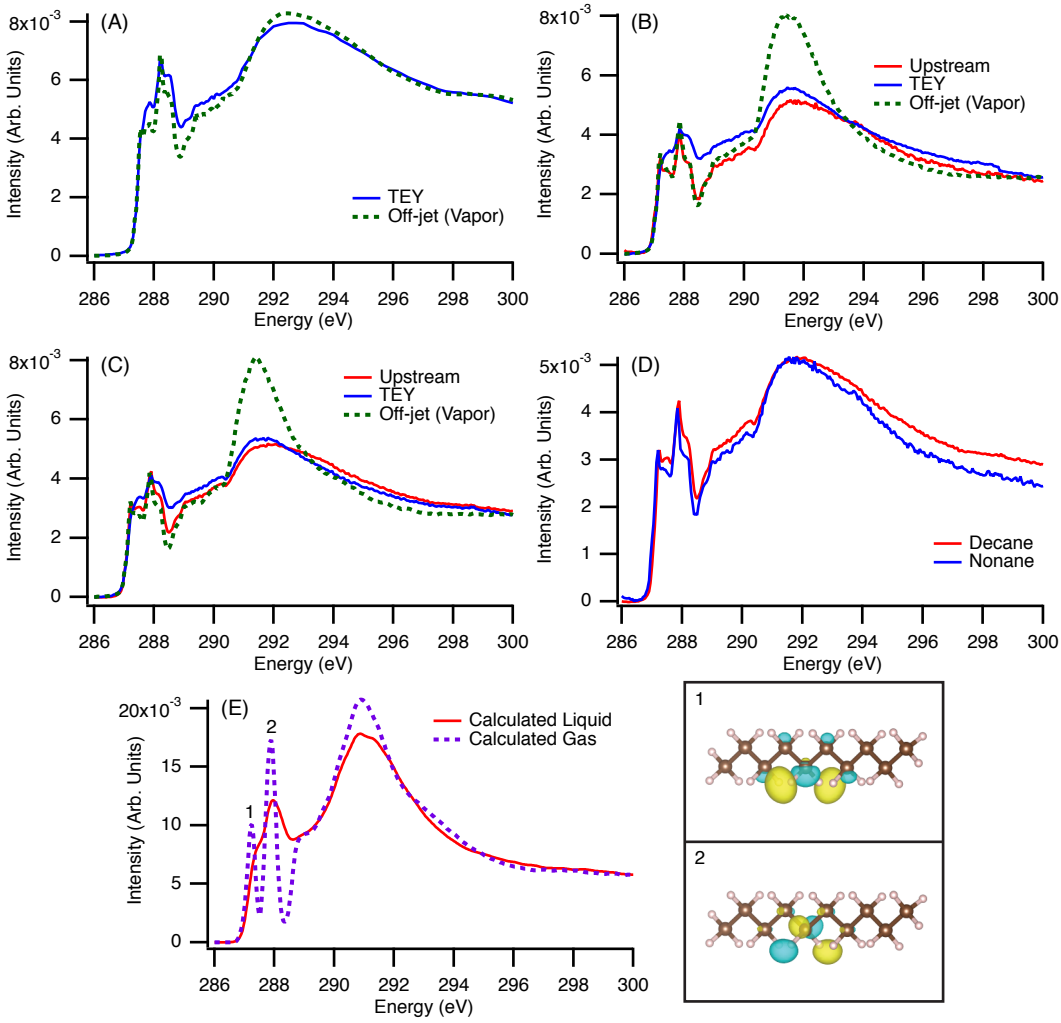

Figure 3.4: Carbon K-edge X-ray absorption spectra for n-nonane and n-decane. All experimental spectra have been area normalized. (A) Previously measured carbon K-edge absorption (TEY) spectra of n-nonane. Off-jet signal, shown in green, is the vapor signal originating from the microjet vapor jacket. (B) Carbon K-edge absorption spectra of n-nonane measured simultaneously with TEY and upstream detection. Off-jet signal, shown in green, is the vapor signal originating from the microjet vapor jacket. FWHM: off-jet: 2.70 eV; TEY: 3.24 eV; upstream: 4.26 eV. Blue-shift relative to off-jet: TEY: 0.11 eV; upstream: 0.30 eV. (C) Carbon K-edge absorption spectra of n-decane measured simultaneously with TEY and upstream detection. Off-jet signal, shown in green, is the vapor signal originating from the microjet vapor jacket. FWHM: off-jet: 2.13 eV; TEY: 4.25 eV; upstream: 5.45 eV. Blue-shift relative to off-jet: TEY: 0.42 eV; upstream: 0.80 eV. (D) Comparison of carbon K-edge liquid phase spectra of nonane and decane measured with upstream detection. (E) Comparison of the calculated carbon K-edge spectra for gas phase decane and liquid decane. Peak 1 (C *1s* $\rightarrow$ σ^*(C–H), 287.2 eV) and peak 2 (C *1s* $\rightarrow$ σ^*(C–H), 287.8 eV).

(TEY: 0.42 eV; upstream: 0.80 eV for decane) relative to the off-jet spectra. A significant reduction (∼40%) in intensity of the feature near 292 eV is observed in the liquid phase spectra. More importantly, the upstream spectra are more blueshifted and broadened, and exhibit a greater reduction in peak intensity than the do TEY on-jet spectra, indicating that the upstream signal exhibits a significantly reduced sensitivity to the vapor, and therefore a far more genuine liquid-phase signal.

To interpret the experimental X-ray absorption spectra, calculations were performed using the XCH density functional theory approach [148] described above for both gas phase and liquid phase decane. As the measured spectra for nonane and decane exhibit nearly identical spectral features, shown in Figure 3.4D, the analogous XCH calculations were not performed for nonane. Due to the inherent similarities between the liquid and vapor spectra, the first two peaks, centered at 287.2 eV and 287.7 eV were assigned by comparing to the calculated spectrum for a single decane molecule, as shown in Figure 3.4E. The two peaks correspond to orthogonal C *1s* $\rightarrow$ σ^*(C–H) transitions. Unlike the broad feature centered near 292 eV, these two peaks are not significantly blueshifted in the liquid. This indicates that the LUMO and LUMO+1 states are not appreciably perturbed by intermolecular interactions in the liquid phase. In contrast, the broad feature centered at 292 eV arises from many highly mixed and delocalized states. The calculated spectrum of liquid decane exhibits the same broadening, shift, and reduction in intensity as the experimental spectrum. The broadening observed in the liquid phase spectra of nonane and decane is primarily a result of inhomogeneous broadening, since the liquid linewidths considerably exceed the gas phase linewidths, which are dominated by the core-hole lifetimes.

Conclusions

Using the new upstream detection approach, unperturbed spectra of two weakly interacting liquids, n-nonane and n-decane, were obtained and exhibit very good agreement with spectra calculated from first principles theory. With this windowless approach, we are able to retain all of the advantages gained from the use of liquid microjets while effectively suppressing the gas phase background. With less volatile liquids, such as water, an essentially complete elimination of the gas phase background is observed. This opens the way for general study of this new class of liquids and solutions.

Chapter 4

Hydrogen Bonding Interactions in Water-Alcohol Mixtures from X-Ray Absorption Spectroscopy

The material in this chapter was reproduced, with permission, from: Lam, R. K.; Smith, J. W.; Saykally, R. J. Communication: Hydrogen Bonding Interactions in Water-Alcohol Mixtures from X-Ray Absorption Spectroscopy. *J. Chem. Phys.* **2016**, *144* (19), 191103.

Introduction

It is well established that non-ideal liquid-liquid binary mixtures can exhibit negative excess entropies of mixing, i.e., the measured entropy of mixing is less than that predicted for the mixing of two ideal liquids. For an ideal mixture of two liquids, A and B, the entropy of mixing is given by

$$S_{id} = -kN[X_A \ln x_A + X_B \ln x_B] \tag{4.1}$$

where k is Boltzmann's constant, N is the number of molecules, and x_i is the mole fraction of each component. The excess entropy of mixing is thereby defined as

$$S^E = S_{mix} - S_{id} \tag{4.2}$$

where S_{mix} is the measured entropy of mixing. Negative excess entropy of mixing would therefore indicate the formation of a non-ideal mixture that exhibits enhanced order or structuring. Many alcohol-water mixtures (i.e., methanol-water, ethanol-water, etc.) exhibit negative excess entropies of mixing, an effect first experimentally characterized by Butler *et al.* in 1933 who deduced the free energy of alcohols in aqueous solution through partial vapor pressure measurements.[36] Methanol-, ethanol-, and isopropanol-water solutions were further examined by Lama and Lu [161] who showed that the excess entropy of mixing in these alcohol water mixtures remained negative for all concentrations of alcohol. Additionally, while the excess enthalpies of mixing for methanol- and ethanol-water mixtures were always

negative, indicating the formation of stronger interactions in the mixtures relative to those in the pure liquids, the excess enthalpy of mixing for isopropanol-water mixture is positive for concentrations above $x_{iPrOH} \approx 0.45$. This positive excess enthalpy of mixing observed in isopropanol-water mixtures was attributed to steric hindrance, resulting from the bulky isopropyl group, impeding ideal hydrogen bond (HB) formation.

Despite significant experimental and theoretical effort [162–172], a converged model for the liquid structure of these mixtures has yet to be established. To explain the anomalous behavior of the alcohol-water mixtures, many have invoked Frank and Evans' proposed iceberg model for the solvation of hydrophobic species in water, wherein water forms clathrate-like structures around the solvated hydrophobic groups [37]. Molecular dynamics (MD) simulations have provided evidence both for and against this model [38–40]. More recently, microscopic clustering and aggregation have been proposed as an alternative explanation for the observed negative excess entropy [173–178]. Experimental studies, employing a wide range of experimental techniques, have thus far been inconclusive [160, 179, 180]. Neutron and X-ray diffraction studies of methanol- and ethanol-water mixtures have concluded that incomplete mixing alone can explain the negative excess entropy of mixing [181–186]. This has been supported by X-ray emission and X-ray absorption studies [155, 156, 187]. Dielectric relaxation and nuclear magnetic resonance spectroscopies support the clustering explanation while also revealing reduced liquid mobility [188–193]. Using Raman spectroscopy, Ben-Amotz *et al.* have concluded that the observed clustering in alcohol-water mixtures is a result of random, rather than hydrophobic, interactions [194, 195]. In contrast, some femtosecond midinfrared spectroscopy experiments have shown that water surrounding the aliphatic groups of the alcohols displays significantly slowed dynamics relative to the bulk, lending support to the model in which the measured negative excess entropy is attributed to water forming clathrate-like structure around the hydrophobic groups of the alcohols [196].

Here, we present a study of methanol-, ethanol-, and isopropanol-water mixtures via liquid microjet X-ray absorption spectroscopy (XAS). XAS is an atom-specific probe of a system's unoccupied electronic states sensitive to both the intermolecular and intramolecular environments. It is therefore ideal for probing liquid structure. Since introducing the use of liquid microjet technology in XAS of liquids in 2001 [27], we have employed this methodology to study a wide variety of phenomena in liquid systems, including ion solvation and pairing in water [28, 29], the solvation of lithium in propylene carbonate [30], the hydrolysis of carbon dioxide [34], and the structure of hydrated carbonic acid [33].

Experimental Methods

Oxygen K-edge total electron yield (TEY) spectra were collected at Beamline 8.0.1 at the Advanced Light Source (ALS) at the Lawrence Berkeley National Laboratory. A detailed description of the experiment has been published previously [117]. Briefly, an intense ($>10^{11}$ photons/s), high resolution ($E/\Delta E = 7000$), and tunable soft X-ray beam is generated by an undulator magnet at the ALS. A dual syringe pump system (Teledyne-ISCO 260D) drives two liquid samples – water (18.2 MΩ·cm from a Millipore purification system) and methanol,

ethanol, or isopropanol – through a mixing tee and an extended length of polyether ether ketone (PEEK) tubing to ensure complete mixing of the liquids (interaction time >1 min), and finally into a 30 μm inner diameter fused silica capillary to create a liquid jet with a linear flow velocity of ∼20 m/s. The liquid beam is intersected with the focused (100 × 35 μm spot size) X-ray beam in a high vacuum ($\sim 2 \cdot 10^{-4}$ Torr) chamber, yielding an on-jet spectrum. The liquid jet then passes through a skimmer and freezes onto a cryogenic trap. The TEY signal is collected as a function of photon energy with a positively biased (2.1 kV) copper electrode placed ∼1 cm above the liquid sample. Vapor phase (off-jet) TEY spectra were collected by translating the liquid microjet above or below the incident X-ray beam. The collected spectra were normalized to the current I_0 collected from a gold mesh located further upstream on the beamline to account for X-ray intensity variations. The vapor phase contribution to the on-jet spectrum was removed via a straightforward subtraction of the measured off-jet spectrum, yielding a liquid phase spectrum.

Results and Discussion

Measured oxygen K-edge spectra for liquid- and vapor-phase water, methanol, ethanol, and isopropanol are presented in Figure 4.1. The liquid phase XA spectrum of water is significantly altered from that of the vapor characterized by both a ∼1 eV blue shift and a large degree of inhomogeneous broadening. The XA spectra of the liquid alcohols exhibit many similarities with that of water. In liquid water, the pre-edge feature, centered at ∼535 eV, is associated with broken hydrogen bonds (HBs) [148]. A similar pre-edge feature is also observed in all of the alcohols, wherein this pre-edge feature is red-shifted (∼1 eV), relative to water, and is lowered in intensity, manifesting only as a shoulder in methanol and ethanol, rather than a distinct peak as seen in water and isopropanol. Note that this is not in agreement with previous finding by Nagasaka *et al.* who observed the absorption onset of methanol and water at the same energy [187].

Significant changes are observed in the pre-edge region of the alcohol spectra (533–535 eV) upon the addition of water (Figure 4.2). In the methanol- and ethanol-water mixtures, a significant reduction in intensity of the alcohol pre-edge feature is observed following the addition of a relatively small amount of water. For the methanol-water mixtures, the methanol pre-edge feature is only present in pure MeOH and 9:1 MeOH:H_2O mixtures. In the 7:3 MeOH:H_2O mixture, only the pre-edge feature of water is present. The water pre-edge peak continues to grow upon further addition of water. In the ethanol-water mixtures, the ethanol pre-edge peak is only present in the pure ethanol spectrum. In mixtures containing both ethanol and water, the ethanol pre-edge feature is entirely absent while the water pre-edge peak appears to increase monotonically with water concentration. This behavior is not observed in the isopropanol-water mixtures where an initial increase in intensity in the isopropanol pre-edge peak is observed for the 9:1 and 7:3 iPrOH:H_2O mixtures. A decrease in the intensity of the peak is observed in the 5:5 iPrOH:H_2O mixture and those with higher fractions of water. The pre-edge feature of liquid water and the analogous feature in the alcohols originate from disorder in the hydrogen bonding network (i.e., broken hydrogen

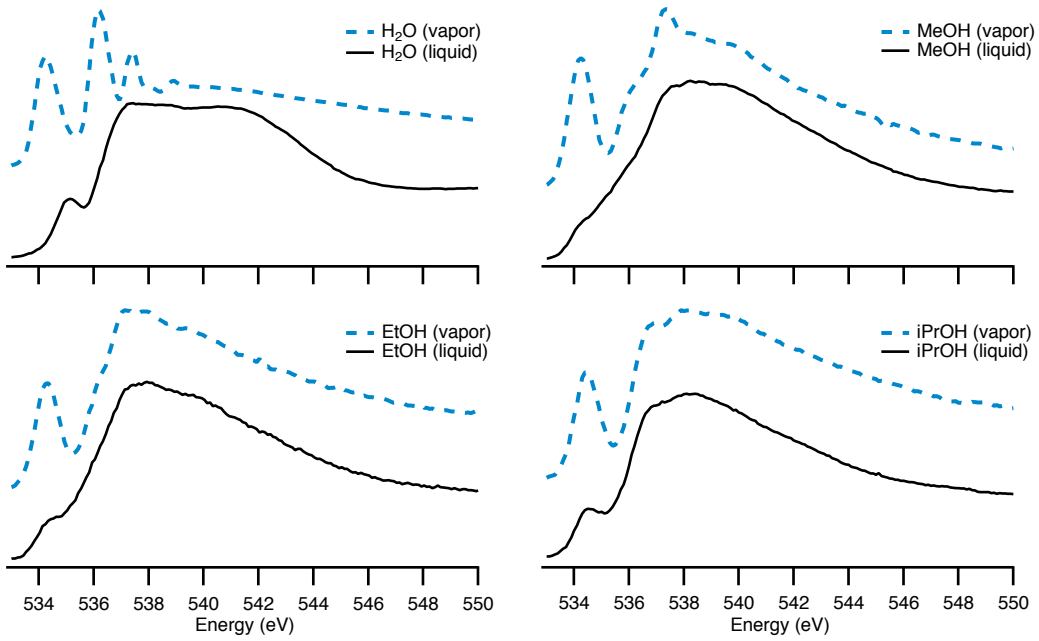

Figure 4.1: Oxygen K-edge XA spectra for vapor (dashed blue) and liquid (solid black) water, methanol, ethanol, and isopropanol. Vapor spectra were collected by translating the liquid jet above or below the incident X-ray beam. The measured spectra have been calibrated via a single-point energy alignment relative to the spectrum of liquid water.

bonds) [148, 160]. The rapid depletion of the alcohol pre-edge features in the spectra of the methanol- and ethanol-water mixtures strongly suggests that the addition of even a small amount of water to methanol and ethanol significantly reduces the number of dangling OH bonds originating from the alcohol molecules. The corresponding formation of additional hydrogen bonding interactions, which suggests enhanced structuring in the mixtures, would be manifested thermodynamically as a reduction in entropy. The even more rapid disappearance of the ethanol pre-edge feature, relative to that of methanol, is consistent with previous measurements of excess entropy of mixing in which ethanol-water mixtures exhibit a more negative excess entropy of mixing than do methanol-water mixtures [161]. Additionally, more recent *ab initio* calculations on methanol- and ethanol-water clusters indicate that the ethanol-water hydrogen bonding interaction is slightly stronger than the methanol-water interaction [197]. In the liquid system, this would likely be manifested as a greater number of alcohol-water hydrogen bonding interactions in ethanol-water relative to methanol-water.

In the isopropanol-water mixtures, an increase in the intensity of the alcohol pre-edge peak is observed for mixtures containing up to 0.5 water mole fraction. This suggests that the addition of water to isopropanol induces more disorder in that portion of the hydrogen bonding network involving the isopropanol as the hydrogen bond donor, consistent with previous measurements of the excess enthalpy of mixing of such mixtures [161]. While the excess enthalpy of mixing of methanol- and ethanol-water mixtures is always negative,

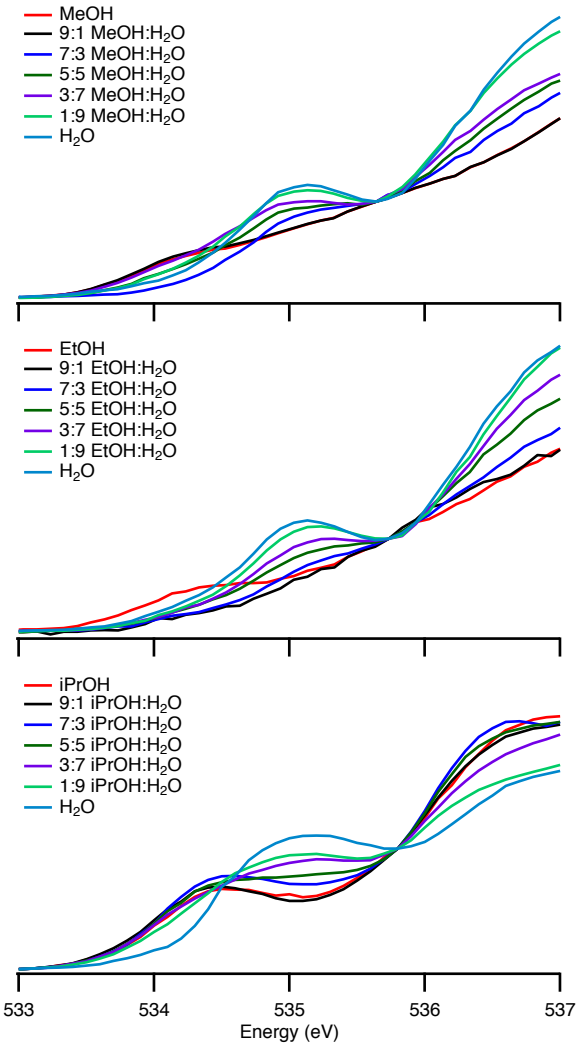

Figure 4.2: Oxygen K-edge XA spectra in the pre-edge region for the alcohol-water mixtures. Top: methanol-water. Middle: ethanol-water. Bottom: isopropanol-water. Ratios indicate molar ratios of the mixtures. Spectra have been normalized to the first minimum above the water pre-edge ($\sim$535.7 eV). The small differences in the pure water spectra collected for the different alcohol-water mixtures are attributable to artifacts from the vapor subtraction. In particular, the on-jet water spectrum collected with the isopropanol mixtures exhibited a greater vapor contribution.

isopropanol-water mixtures exhibit a positive excess enthalpy of mixing in mixtures with isopropanol mole fraction concentrations greater than 0.5. A positive excess enthalpy of mixing is indicative of weaker liquid-liquid interactions present in the mixture relative to those in the pure liquids. A reduction in the population of isopropanol-water hydrogen bonds or an increase in the disorder in the hydrogen bonding network can account for this measured thermodynamic property of the liquid. It cannot, however, account for the negative excess entropy of the isopropanol-water as a reduction in hydrogen bonding should result in an increase in the entropy. Therefore, the measured negative excess entropy of the isopropanol-water system likely originates from incomplete mixing between the two liquids.

Conclusions

We have presented oxygen K-edge X-ray absorption spectra of methanol-, ethanol-, and isopropanol-water mixtures. The spectra exhibit reproducible changes in the oxygen pre-edge region (533–537 eV), corresponding to changes in the hydrogen bonding environment. In the methanol- and ethanol-water mixtures, we find that the addition of water results in a significant reduction in dangling alcohol OH bonds, evidenced by the rapid depletion of the alcohol pre-edge peak. While this observation does not preclude micro-immiscibility as a contributing factor to the measured negative excess entropy of mixing, the formation of additional liquid-liquid interactions would also contribute to the anomalous thermodynamic properties of the methanol- and ethanol-water mixtures. In contrast, in isopropanol-water mixtures, the addition of water initially results in an increase in the isopropanol pre-edge the intensity, which indicates a significant increase in dangling alcohol OH bonds upon the addition of water. In isolation, the disruption of the hydrogen bonding network in the isopropanol-water mixtures would result in an increase in the entropy of mixing. The measured negative excess entropy of the isopropanol system is likely a consequence of inhomogeneous mixing.

Chapter 5

X-Ray Spectroscopy of Aqueous Carbonates

5.1 The Hydration Structure of Aqueous Carbonic Acid from X-Ray Absorption Spectroscopy

The material in this section was reproduced, with permission, from: Lam, R. K.; England, A. H.; Sheardy, A. T.; Shih, O.; Smith, J. W.; Rizzuto, A. M.; Prendergast, D.; Saykally, R. J. The Hydration Structure of Aqueous Carbonic Acid from X-Ray Absorption Spectroscopy. *Chem. Phys. Lett.* **2014**, *614*, 282–286.

Introduction

Aqueous carbonic acid (H_2CO_3) is the centerpiece of both the global carbon cycle [44–46] and physiological buffer and respiration systems [47–49], yet it remains incompletely characterized despite enormous effort. As described in a very recent review [198], carbonic acid has been well studied in both the gas phase [199–201] and in cryogenic matrixes [202–206], but there have been very few successful spectroscopic studies of the aqueous acid, and none of its electronic structure [42, 50, 51]. Carbonic acid is intrinsically unstable upon contact with even a single water molecule, reacting via a proton chain mechanism to rapidly form aqueous bicarbonate, carbonate, and hydrated protons [207–209], which comprises the reversible mechanism for dissolution of CO_2 gas. Here we report the first measurement of X-ray absorption spectra for aqueous carbonic acid, enabled by the use of fast-flow liquid microjet technology [24, 27, 41], wherein protonation of a bicarbonate solution continuously generates the acid as a function of pH under ambient conditions. We combine molecular dynamics (MD) simulations with a first principles density functional theory (DFT) method [148] to model and interpret the small (0.2 eV) measured blueshift of the carbonic acid π^* orbital in the C K-edge spectrum relative to that of bicarbonate [41], thereby gaining new and detailed insights into the nature of aqueous carbonic acid. We find that the two

most stable isomers donate two strong hydrogen (H–) bonds to water oxygens and accept a stronger H-bond at the carbonyl and weaker H-bonds at the acidic oxygens, exhibiting an average hydration number of 3.17 as torsional motions rearrange the solvation structures. Because both gas phase and solid phase carbonic acid have been well studied, this work will facilitate the development of detailed models for the reversible gas-liquid chemistry of carbon dioxide.

Near edge X-ray absorption fine structure spectroscopy (NEXAFS), is an atom-specific probe of both the electronic structure of a molecule and its local chemical environment, making it a method of choice for detailed characterization of hydration interactions. Until very recently, NEXAFS studies of the carbonate system were restricted to gaseous CO_2 [210], and to carbonates adsorbed to a surface [211] or in various solid mineral forms [212] by the difficulties then inherent in addressing liquid samples by this high vacuum technology. In 2011, we reported the first NEXAFS study of aqueous carbonate and bicarbonate ions [41], which was followed by an X-ray emission study in 2014 [213]. In the present experiment, we follow an approach similar to that employed by Eberle *et al.* [50] in observing Raman spectra of aqueous H_2CO_3, enabled by the slow dehydration of carbonic acid ($k = 26.3$ s^{-1}, $t_{1/2} \approx 26$ ms) relative to the very rapid protonation rate of the bicarbonate anion ($k_{on} = 4.7 \cdot 10^{10}$ M^{-1}s^{-1}, $t_{1/2} \approx 21.3$ ps; $[H^+] = [HCO_3^-] = 1$ M) [42, 43], which facilitates accumulation of carbonic acid. We combine a 0.5 M solution of $NaHCO_3$ with 1 M HCl in a high velocity liquid microjet mixing system to generate the acid at 25°C.

Materials and Methods

A. Sample Preparation

Samples (0.5 M $NaHCO_3$ and 1 M HCl) were prepared using 18.2 MΩ·cm resistivity water obtained from a Millipore purification system. Concentrated HCl (12.1 M) was obtained from J.T. Baker. $NaHCO_3$ with stated purity of at least 99.7% was commercially obtained from Sigma-Aldrich. Samples were used without further purification.

B. Experimental Design

Carbon K-edge total electron yield (TEY) spectra were collected at Beamline 8.0.1. A detailed description of the experimental setup has been published previously [117]. Briefly, an intense (>10^{11} photons/s), high resolution (E/ΔE = 7000), tunable soft X-ray beam is generated from an undulator at the ALS. The beam is focused (100 × 35 μm spot size) onto the liquid microjet. A dual syringe pump system (Teledyne-ISCO 260D) drives the solution through 30-50 μm inner diameter fused silica tubing to generate the liquid microjet with high linear flow velocities (1–200 m/s) that is intersected with the X-ray beam in the high vacuum ($\sim 2 \cdot 10^{-4}$ Torr) chamber.

Solutions are typically mixed shortly after the pump. The mixed solution then travels through several meters of PEEK tubing (∼7.5 min mixing time) before reaching the silica

capillary. The long mixing time associated with this 'standard' experimental setup precluded studies of short-lived intermediate species such as carbonic acid. To transcend this limitation, a new fast-flow microjet mixing system was designed to mix the two solutions immediately prior to the generation of the fast-flowing liquid jet. A Hastelloy Microvolume Y-Connector was mounted inside the vacuum chamber and used to generate the liquid jet. To introduce the sample, two of the openings in the connector were attached directly to the syringe pumps with PEEK tubing. The third was used to hold the silica capillary and generate the liquid jet. The mixing time in this scheme was shortened to ∼0.5 ms, thereby facilitating the observation of short-lived species in solution. This time is shorter than the previously measured half-life of carbonic acid (∼26 ms) [50] but significantly longer than the measured rate for the proton transfer to bicarbonate ($k_{on} = 4.7 \cdot 10^{10}$ M^{-1} s^{-1}) [42, 43]. The liquid jet then passes through a skimmer and freezes onto a cryogenic (liquid nitrogen) trap. A TEY signal is then collected as a function of photon energy (0.2 eV step size), with a positively biased (2.1 kV) copper electrode. Vapor phase TEY spectra were measured by positioning the microjet a few microns above or below the incident X-ray beam.

C. Simulations and Calculations

The associated molecular dynamics (MD) simulations and calculated spectra were published previously [41]. Briefly, Amber 9 [214] was used to generate 10 ns classical NVT-MD trajectories for gaseous and dissolved CO_2 and Quantum mechanics/molecular mechanics (QM/MM) trajectories for aqueous carbonate and carbonic acid. The simulation box for the aqueous species contained ∼90 TIP3P water molecules. From the generated trajectories, molecular configurations were taken from 100 uncorrelated snapshots and used in the first principles spectral calculation.

X-ray absorption spectra were calculated using the eXcited electron and Core Hole (XCH) density field theory (DFT) method [148]. In this approach, the lowest energy core-hole excited state is treated explicitly. Higher excited states are generated from the resulting self-consistent field. The electronic structure was calculated using PWSCF from the Quantum ESPRESSO package [149] and the exchange correlation energy was calculated with the PBE exchange correlation functional under the generalized gradient approximation [150]. A plane wave basis set with a 25 Ry kinetic energy cutoff and periodic boundary conditions was used to model the localized and delocalized states. The calculated spectra were then aligned relative to the C *1s* → π^* peak in the experimental gaseous carbon dioxide spectrum. Isosurfaces were calculated with Quantum ESPRESSO and rendered in VESTA [151].

Results

Using the fast-flow microjet mixing system, X-ray absorption spectra of bicarbonate, 1:2, 1:1, and 2:1 mole fraction acid:bicarbonate mixtures were measured. The spectrum of 1:1 acid:bicarbonate was also measured without the fast-flow mixing system, wherein the increased mixing time ensured that only gaseous carbon dioxide was present at the time of

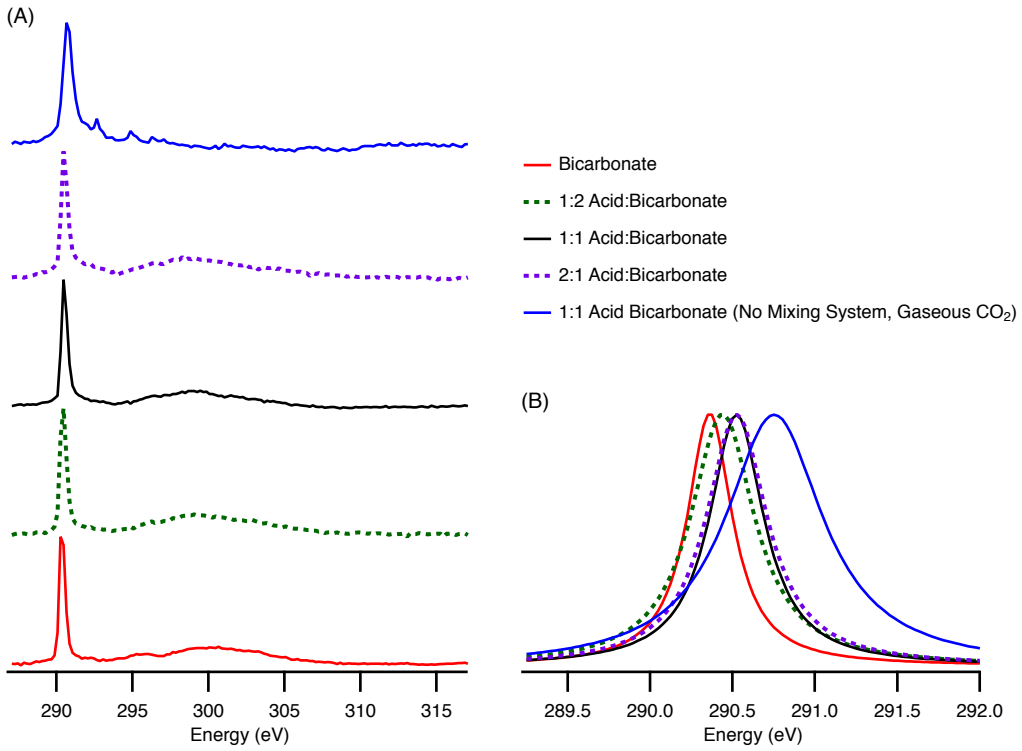

Figure 5.1: Peak-normalized experimental carbon K-edge X-ray absorption spectra. (A) Overview of measured spectra for bicarbonate (red), and the mixtures 1:2 HCl:$NaHCO_3$ (green), 1:1 HCl:$NaHCO_3$ (black), 2:1 HCl:$NaHCO_3$ (purple), and 1:1 HCl:$NaHCO_3$ without the mixing system (blue). (B) Lorentzian-fit experimental X-ray absorption spectra of the C *1s* $\rightarrow$ π^* transition in bicarbonate (red), 1:2 HCl:$NaHCO_3$ (green), 1:1 HCl:$NaHCO_3$ (black), 2:1 HCl:$NaHCO_3$ (purple), and 1:1 HCl:$NaHCO_3$ without the mixing system (blue). The maximum absorptions are at 290.35, 290.45, 290.53, 290.53, and 290.75 eV, respectively. All other spectra were measured using a sample introduced by the fast-flow microjet mixing system.

measurement. Good agreement between experimentally acquired spectra with the previously calculated [41] first principles eXcited electron Core Hole (XCH) spectra [148] establish the predictive nature of the XCH method and indicate that aqueous carbonic acid is indeed the short-lived intermediate in the hydrolysis of carbon dioxide to form carbonate. Details of the hydration structure of the acid are revealed in the molecular dynamics simulations underlying the calculated XCH spectra [41].

The NEXAFS data are shown in Figure 5.1A. Spectra have been peak-normalized and offset for clarity. All of these experimental spectra, with the exception of that for gaseous carbon dioxide, exhibit a broad resonance between 293 and 305 eV. Through comparison with the calculated isosurfaces of excited electronic states in this energy range, this resonance is assigned to a C *1s* $\rightarrow$ π^* transition for either bicarbonate or carbonic acid, depending on pH.

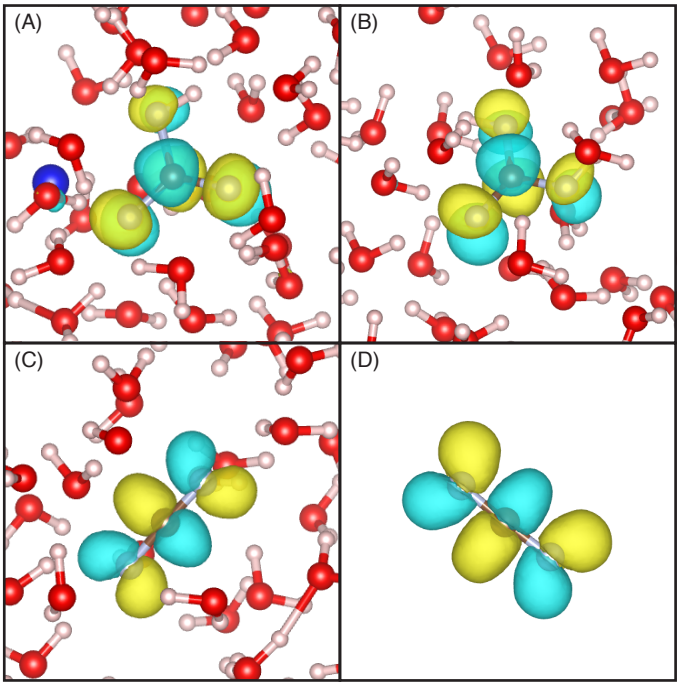

Figure 5.2: Isosurfaces of the core-excited electron density for the π^* resoncances. Oxygen atoms on the carbonate species are shaded. (A) $NaHCO_3$, (B) H_2CO_3, (C) aqueous CO_2, (D) gaseous CO_2.

The sharp peaks centered at ∼290 eV (Figure 5.1B) are assigned to the respective C *1s* $\rightarrow$ π^* transitions for the different carbonate species. Isosurfaces for the π^*(C=O) state are shown in Figure 5.2 for bicarbonate (Figure 5.2A), carbonic acid (Figure 5.2B), dissolved carbon dioxide (Figure 5.2C), and gaseous carbon dioxide (Figure 5.2D). These images were chosen from molecular configurations whose spectra closely matched the simulated average spectra of the thermodynamic ensembles. The experimental C *1s* $\rightarrow$ π^* peaks have been fit to a Lorentzian distribution (Figure 5.3) to facilitate the comparison with the calculated spectra. In the C *1s* $\rightarrow$ π^* transition, a reproducible blueshift (∼0.2 eV) from the bicarbonate spectrum to the 1:1 acid:bicarbonate mixture is observed. Furthermore, the gaseous carbon dioxide (1:1 mixture without the mixing system) spectrum exhibits an additional blueshift (∼0.2 eV) relative to the 1:1 mixture acquired using the fast-flow microjet mixing system. For the 1:2 acid:bicarbonate mixture, a broader C *1s* $\rightarrow$ π^* peak is observed. This feature spans the width of the peaks observed in bicarbonate and in the 1:1 mixture, indicating that both bicarbonate and the species present in the 1:1 mixture were also present in the 1:2 mixture. The 2:1 acid:bicarbonate mixture produced the same shift as the 1:1 mixture.

To assign the measured spectral features to specific species, the experimentally measured spectra were compared to our [22] previously calculated spectra (Figure 5.4). The theoretical spectra were energy-aligned relative to the C *1s* $\rightarrow$ π^* transition for gaseous carbon dioxide. Comparison of the σ^* features confirmed that the species absorbing in the 1:1 and

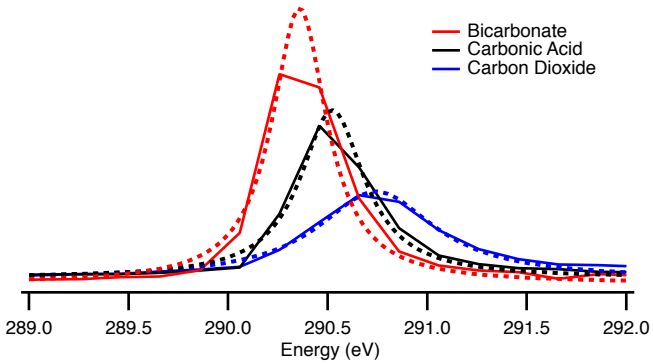

Figure 5.3: Unnormalized experimental spectra of the C *1s* $\rightarrow$ π^* transition (solid lines) for $NaHCO_3$ (red), H_2CO_3 (black), and CO_2 (blue). The Lorentzian fits are shown in the dashed lines. FWHM: 0.025 eV ($NaHCO_3$), 0.038 eV (H_2CO_3), 0.11 eV ($CO_{2(g)}$).

2:1 acid:bicarbonate mixtures was not carbon dioxide, viz. the broad σ^* resonance between 293–305 eV is present in both the experimental and theoretical spectra of bicarbonate and carbonic acid, but is not observed for carbon dioxide. Gaseous carbon dioxide does, however, exhibit a weak characteristic vibronic peak ~2 eV higher in energy than the C *1s* $\rightarrow$ π^* peak [41], which was observed in the 1:1 mixture acquired without the fast-flow mixing system. The C *1s* $\rightarrow$ π^* transition observed for the 1:1 and 2:1 mixtures exhibits excellent agreement between the experiment and calculated carbonic acid spectra, viz. the reduction in peak intensity, along with the observed shifts of the π^* feature is observed in both the calculated and experimental spectra. The shifts observed between different carbonate species originate from the energy differences between the ground state and core-excited states of the respective species interacting with the surrounding solvent molecules. The decrease in peak intensity of the carbonic acid feature can be attributed to the coexistence of multiple rotamers (cis-cis (CC), cis-trans (CT), trans-trans (TT)) and their respective hydration environments. In the calculated spectra for the different rotamers of carbonic acid, the C *1s* $\rightarrow$ π^* features exhibit small shifts (CC: 0.024 eV blueshift, CT: 0.024 red shift relative to TT), which would effect the observed broadening and reduction in intensity. The isosurface for the cis-trans rotamer is shown in Figure 5.2B. The species observed in the 1:1 and 2:1 acid:bicarbonate mixtures was therefore assigned to aqueous carbonic acid. The broad C *1s* $\rightarrow$ π^* peak observed for the 1:2 acid:bicarbonate mixture was attributed to the presence of both bicarbonate and carbonic acid. The agreement between the previously calculated spectrum of aqueous carbonic acid and present experimental spectra demonstrates the predictive power of our XCH spectral calculation.

The recent *ab initio* MD study by Kumar *et al.* [215] addresses the hydration of the respective carbonate species, predicting that the solvation strength correlates with the net charge on the solute,and that neutral CO_2 acts like a typical hydrophobic solute, inducing stronger hydrogen bonds among the adjacent waters. Considerable steric impedance to optimal solvation is observed, and hindered librational motions of the hydrogen-bonded

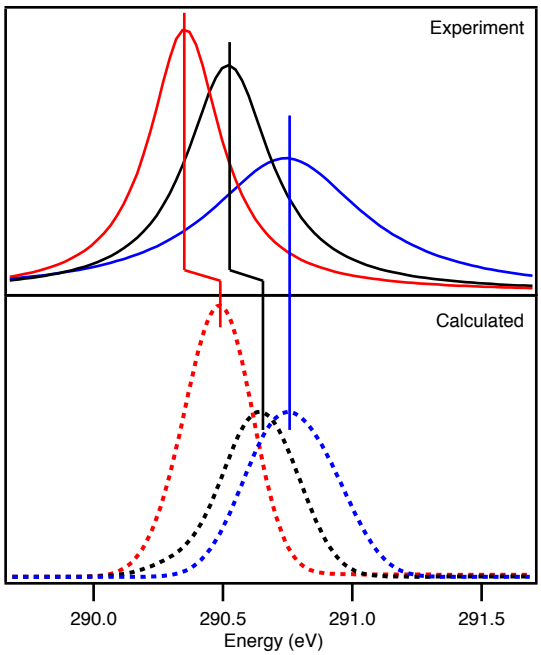

Figure 5.4: Lorentzian-fit experimental and calculated spectra of the C *1s* $\rightarrow$ π^* transition of carbonate species. Bicarbonate (red), carbonic acid (black), and gaseous carbon dioxide (blue). Theoretical spectra were energy-aligned to the experimental spectra for gaseous CO_2. Experimental spectra are area normalized to facilitate comparison with the calculated spectra.

network rearrange the solvation structures. Hydrogen bonds donated by carbonic acid to first-shell oxygen atoms are predicted to be stronger than those donated by water to either the hydroxyl or carbonyl oxygens of the acid. These predictions are partially supported by the experimental results presented here. The radial distribution functions (RDFs) for the carbonyl oxygen to water hydrogens for the different carbonate species in the snapshots used in the XCH calculations are shown in Figure 5.5 [216]. The shift of the first peak in the RDF to shorter distances with increasing negative charge of the carbonate species, indicative of increasing hydrogen bond strength, agrees with previous predictions [215, 217, 218]. In general, the increasing H-bond strength is proportional to the hydration number (measured for distances up to 2.5 Å): Na_2CO_3 (5.55), HCO_3 (4.26), H_2CO_3 (3.17), CO_2 (0.56). These are lower than previously reported values (9.09–5.55 for carbonate and 5.41–4.26 for bicarbonate) due to the inclusion of the sodium counterion in our simulations [41]. While the RDF for the hydroxyl oxygen to water hydrogen shown in Figure 5.6 also shows good agreement with the predictions made by Kumar *et al.*, indicating that the hydroxyl oxygen of carbonic acid is a poor hydrogen bond acceptor, our simulations indicate that the H-bonds accepted by the carbonyl oxygen are slightly stronger and more structured that those donated by the hydroxyl hydrogens. This is supported by the slightly shorter $=O–H_w$ distances and the narrower first peak in the $=O–H_w$ RDF relative to that of the $H_O–O_w$

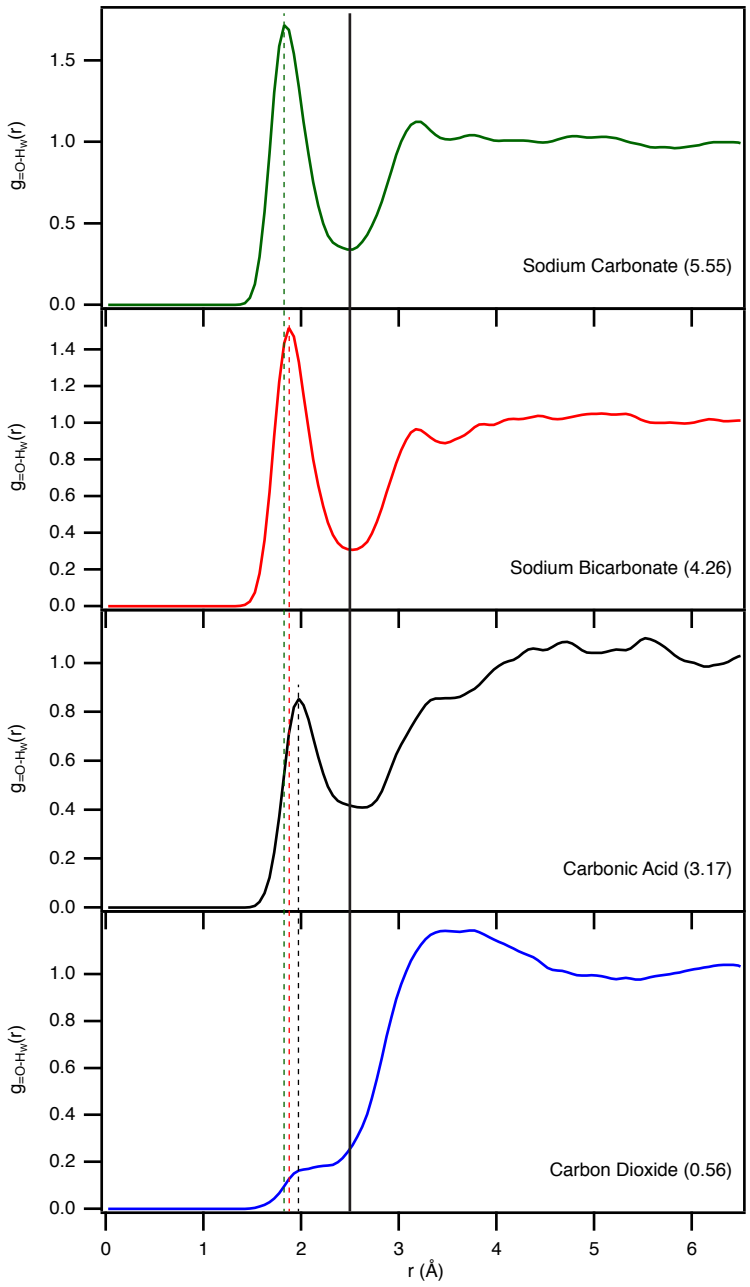

Figure 5.5: Calculated radial distribution functions for the carbonyl oxygen to water hydrogens of the different carbonate species. The carbonate and bicarbonate simulations include sodium counterions. Number in parentheses corresponds to the coordination number to distances of 2.5 Å.

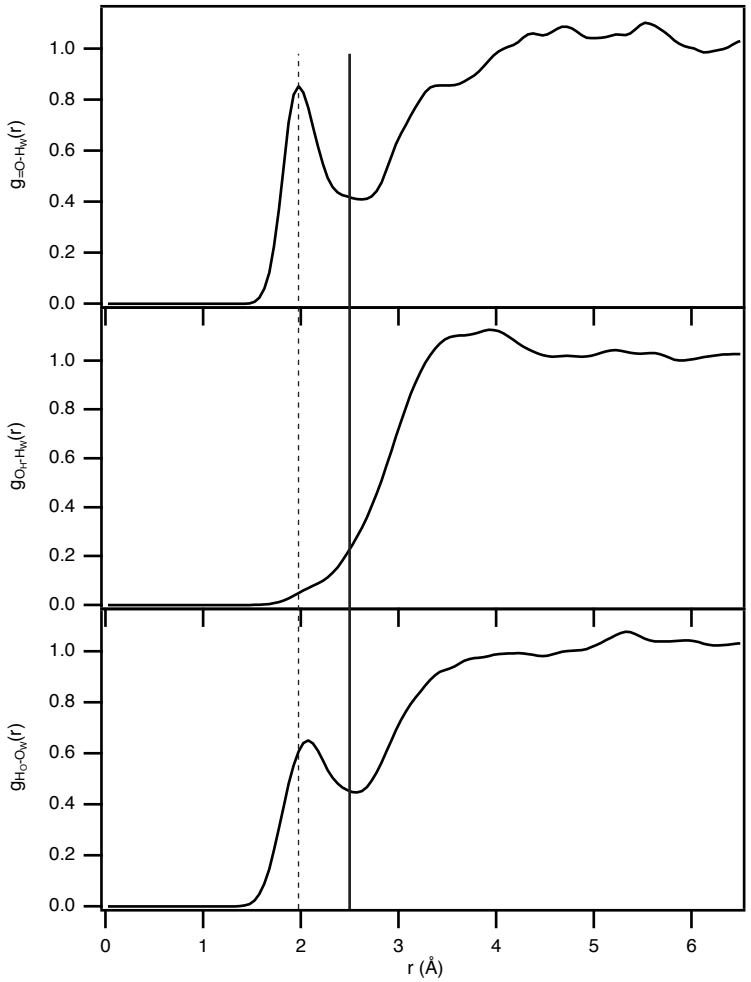

Figure 5.6: Calculated radial distribution functions for carbonic acid. The labels =O, O_H, and HO refer to the carbonyl, hydroxyl oxygen, and hydroxyl hydrogen respectively. O_w and H_w refer to the oxygens and hydrogens of the water molecules.

RDF. The structural variability observed in the H-bonds donated by the acidic protons of carbonic acid likely results from the interconversion of the carbonic acid between its different rotamers and their respective hydration environments.

Conclusions

In summary, this first characterization of carbonic acid under ambient aqueous conditions by the atom selective technique of X-ray absorption spectroscopy and first principles XCH calculations establishes the detailed hydration properties of this short-lived species. Calculated spectral energy shifts and intensities for the species observed (bicarbonate, carbonic acid, gaseous carbon dioxide) correspond well with the experimentally measured spectra,

demonstrating the predictive power of the XCH technique for calculating reliable core-level spectra. We expect that these results will thereby facilitate future studies of the carbon dioxide chemistry in geological and biological systems.

5.2 The Hydration Structure of Dissolved Carbon Dioxide from X-Ray Absorption Spectroscopy

The material in this section was reproduced, with permission, from: Lam, R. K.; England, A. H.; Smith, J. W.; Rizzuto, A. M.; Shih, O.; Prendergast, D.; Saykally, R. J. The Hydration Structure of Dissolved Carbon Dioxide from X-Ray Absorption Spectroscopy. *Chem. Phys. Lett.* **2015**, *633*, 214–217.

Introduction

The dissolution of carbon dioxide in water and its subsequent hydrolysis reactions comprise one of the most central processes in all of science [44–46, 219–228], yet it remains incompletely understood despite enormous effort [198]. The solubility of gaseous CO_2 is governed by Henry's Law under equilibrium conditions ($k_{H,cp} = 3.38 \cdot 10^{-2}$ mol $L^{-1}atm^{-1}$), with normal average CO_2 pressures in the atmosphere ($3.9 \cdot 10^{-4}$ atm) yielding total dissolved CO_2 concentrations of $1.33 \cdot 10^{-5}$ M in pure water [198]. Most of this is present as the weakly hydrated CO_2 molecule, but a small fraction ($\sim$1%) hydrolyzes to form the short-lived carbonic acid (H_2CO_3) molecule, which subsequently forms bicarbonate, and carbonate ions via proton transfer reactions [215, 229, 230].

The chemical reaction of CO_2 with water to form carbonic acid is clearly the central feature of these carbonate equilibria, and has been addressed by many experiments [42, 50, 51, 220, 230–236] and calculations [51, 208, 209, 215, 218, 237–242] with conflicting results. Details of the neutral CO_2 solvation by bulk water prepare the reaction pathway, and are thus a determining factor in this chemistry.

We previously characterized the hydration structures of aqueous carbonate and bicarbonate using X-ray absorption spectroscopy [41]. More recently, we described the use of a fast-flowing liquid microjet mixing system to protonate a bicarbonate solution to generate the short-lived ($k = 26.3\ s^{-1}$, $t_{1/2} \approx 26$ ms) carbonic acid molecule [42, 43], which was subsequently probed by soft X-ray absorption spectroscopy. Interpretation of the measured spectra via first principles theory provided a detailed picture of the hydration of the acid as donating two strong hydrogen bonds to solvating waters while acting as a weak acceptor of one such bond [33]. Here we apply this same approach to study the hydration of dissolved carbon dioxide, providing the first experimental characterization of the solvated neutral molecule.

Materials and Methods

A. Sample Preparation

Samples (1 M $NaHCO_3$ and 1 M HCl) were prepared using 18.2 MΩ·cm resistivity water obtained from a Millipore purification system. Concentrated HCl (12.1 M) was obtained

from J.T. Baker. $NaHCO_3$ (>99.7% purity) was obtained from Macron Fine Chemicals. Samples were used without further purification.

B. Experimental Design

Carbon K-edge total electron yield (TEY) spectra were collected at Beamline 8.0.1. A detailed description of the experimental setup has been published previously [117]. A high flux ($>10^{11}$ photons/s), high resolution ($E/\Delta E = 7000$), tunable soft X-ray beam is generated from an undulator at the Advanced Light Source (ALS), Lawrence Berkeley National Lab (LBNL). A dual syringe pump system (Teledyne-ISCO 260D) drives the two solutions through the fast-flow liquid mixing system and into a 50 μm ID capillary to generate the liquid microjet. The X-ray beam is focused (100 $\times$ 35 μm spot size) onto the jet in a high vacuum chamber ($\sim 2 \cdot 10^{-4}$ Torr). The liquid jet then passes through a skimmer and freezes onto a cryogenic (liquid nitrogen) trap. The TEY signal is collected as a function of photon energy (0.05 eV step size) using a biased copper electrode (2.1 kV) positioned $\sim$1 cm above the jet. Vapor phase TEY spectra were measured by positioning the microjet a few mm above or below the liquid stream. Measured TEY spectra were processed using the finite impulse response (FIR) Fourier filtering algorithm in Igor Pro (Wavemetrics) to remove the high frequency background introduced by the liquid microjet mixing system.

C. Simulations and Calculations

The molecular dynamics (MD) simulations and calculated X-ray absorption spectra were published previously [33, 41]. Briefly, Amber 9 [214] was used to generate 10 ns classical NVT-MD trajectories for gaseous and dissolved CO_2 and Quantum mechanics/molecular mechanics (QM/MM) trajectories for carbonic acid. The simulation box for the aqueous species contained $\sim$90 TIP3P water molecules. 100 uncorrelated snapshots were taken from each trajectory for use in the spectral calculation.

X-ray absorption spectra were calculated using the eXcited electron and Core Hole (XCH) density function theory (DFT) method [148]. Under the XCH approximation, the lowest energy core-hole excited state is treated explicitly while the higher excited states are generated from the resulting self-consistent field. The electronic structure was calculated using PWSCF from the Quantum ESPRESSO package [149] and the PBE exchange correlation functional under the generalized gradient approximation was used to calculate the exchange correlation energy [150]. A plane wave basis set, employing the Vanderbilt Ultra-Soft Pseudopotential [243], with a 25 Ry kinetic energy cutoff and periodic boundary conditions was used to model the localized and delocalized states. The resulting calculated spectra were aligned relative to one another using the atomic alignment scheme developed previously wherein the calculated excitation energy is aligned with respect to that of an isolated carbon atom [41]. The calculated spectrum for CO_2 was then aligned to the corresponding C *1s* $\rightarrow$ π^* peak of gas phase CO_2. All other calculated spectra were aligned relative to that.

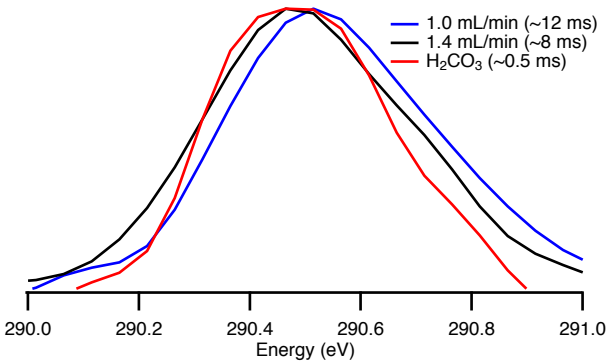

Figure 5.7: Peak-normalized experimental carbon K-edge X-ray aborption spectra of the C(1) $\rightarrow$ π^* transition of 1:1 HCl:$NaHCO_3$ mixtures at different interaction times. The absorption maxima are at 290.5 eV (H_2CO_3, 0.5 ms), 290.5 eV (1 mL/min, $\sim$8 ms), and 290.66 eV (1.4 mL/min, $\sim$12 ms). All spectra were measured using a step size of 0.05 eV with samples introduced by the fast-flow microjet mixing system.

Calculated Radial Distribution Functions (RDFs) were generated using VMD Molecular Graphics Viewer [244].

Results and Discussion

Using the fast-flow liquid microjet mixing system, the X-ray absorption spectra of a 1:1 acid:bicarbonate mixture was measured following three different interaction times, controlled by altering both the length of the silica capillary used to form the microjet and the volumetric flow rate. The X-ray absorption spectra of the C *1s* $\rightarrow$ π^* transition measured at the different mixing times are shown in Figure 5.7. As the interaction time between the acid and bicarbonate increases, a small, but measurable, blue shift ($\sim$0.05–0.1 eV) is observed. The spectrum shown in black corresponds to the shortest interaction time ($\sim$0.5 ms) and was assigned to aqueous carbonic acid (k = 26.3 s^{-1}). At this shorter time, only a small amount ($\sim$1.3%) of the carbonic acid generated via the prontonation of bicarbonate (k_{on} = $4.7 \cdot 10^{10}$ $M^{-1}s^{-1}$) has decomposed into dissolved carbon dioxide and water (k = 26.3 s^{-1}) [42, 43]. To lengthen the time before measuring the X-ray absorption spectrum, a 10 cm long, 50 μm ID silica capillary was used at two different flow rates (1.4 mL/min and 1.0 mL/min) which corresponds to an interaction time of $\sim$8 and $\sim$12 ms respectively. With the increased interaction time, significantly larger amounts, $\sim$19% and 27% of the initial 0.5 M aqueous carbonic acid concentration, of carbon dioxide should be present.

While gaseous carbon dioxide exhibits a weak vibronic peak at $\sim$292.8 eV, dissolved carbon dioxide does not. As shown in Figure 5.8, the vibronic peak is not present in the spectra measured following the longer interaction times, indicating that the observed blueshift is a result of the presence of dissolved, rather than gaseous, carbon dioxide. The observed blueshift is also consistent with predictions from theory. The calculated C *1s* $\rightarrow$ π^* transi-

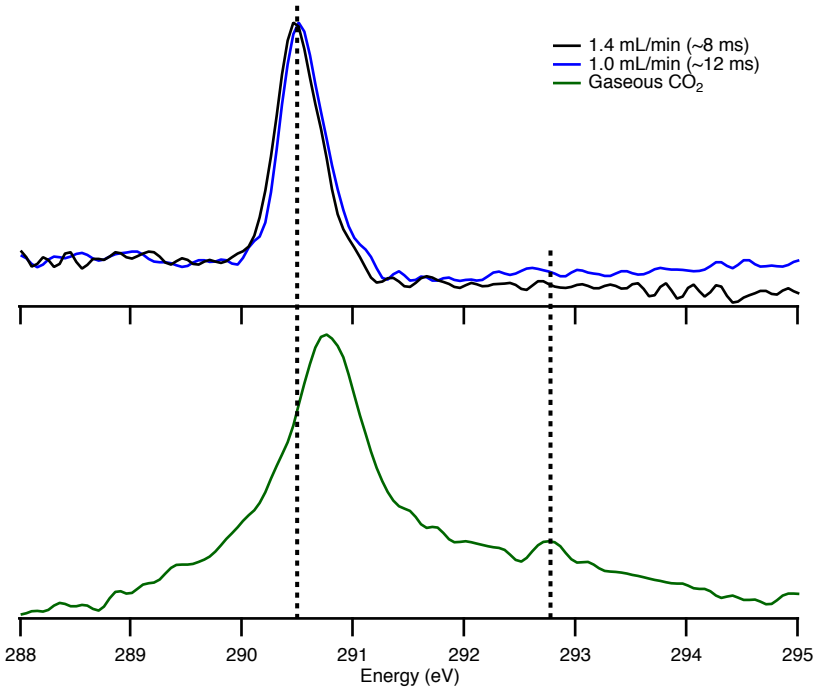

Figure 5.8: Comparison between XA spectra of 1:1 HCl:$NaHCO_3$ mixtures at ∼8 and ∼12 ms interaction times with those of gaseous CO_2. Gaseous CO_2 exhibits a characteristic vibronic peak at 292.75 eV that is not present for dissolved CO_2.

tion (Figure 5.9) of dissolved carbon dioxide exhibits a small (∼0.4 eV) blueshift from that of carbonic acid and is slightly redshifted (∼0.7 eV) from that of gaseous carbon dioxide.

The solvation structure of dissolved CO_2 has been addressed by molecular dynamics simulations. From snapshots generated from the MD simulations, we find the average hydrogen bond number of CO_2, measured to a distance of 2.5 Å, to be 0.56 vs. 3.17 for H_2CO_3, indicating that dissolved CO_2 is poor hydrogen bond acceptor and is extremely weakly hydrated. The radial distribution functions (RDFs) for the carbonyl oxygen (=O) to water hydrogen (H_w) distances for dissolved CO_2 and H_2CO_3 are shown in Figure 5.10. A shift of the first peak in the RDF to a longer distance in CO_2 indicates a weaker interaction between the CO_2 carbonyl oxygens and the water hydrogens relative to that of H_2CO_3. The C–O_w RDFs for CO_2 and H_2CO_3 (Figure 5.10) both show a broad peak around 3–5 Å. The onset of this broad feature is shifted to shorter distances for hydrated CO_2 relative to that of H_2CO_3 indicating a stronger interaction between the CO_2 carbon and the water oxygens. This C–O_w interaction is a prerequisite for the hydrolysis of dissolved CO_2 to form carbonic acid, bicarbonate, and carbonate [34]. While the RDFs between the water oxygens (O_w) of aqueous CO_2 and H_2CO_3, shown in Figure 5.11, are not significantly different from that of pure water, the RDFs of both CO_2 and H_2CO_3 of exhibit a higher first maximum and a lower first minimum, indicating a more ordered liquid structure surrounding the solute. This result is

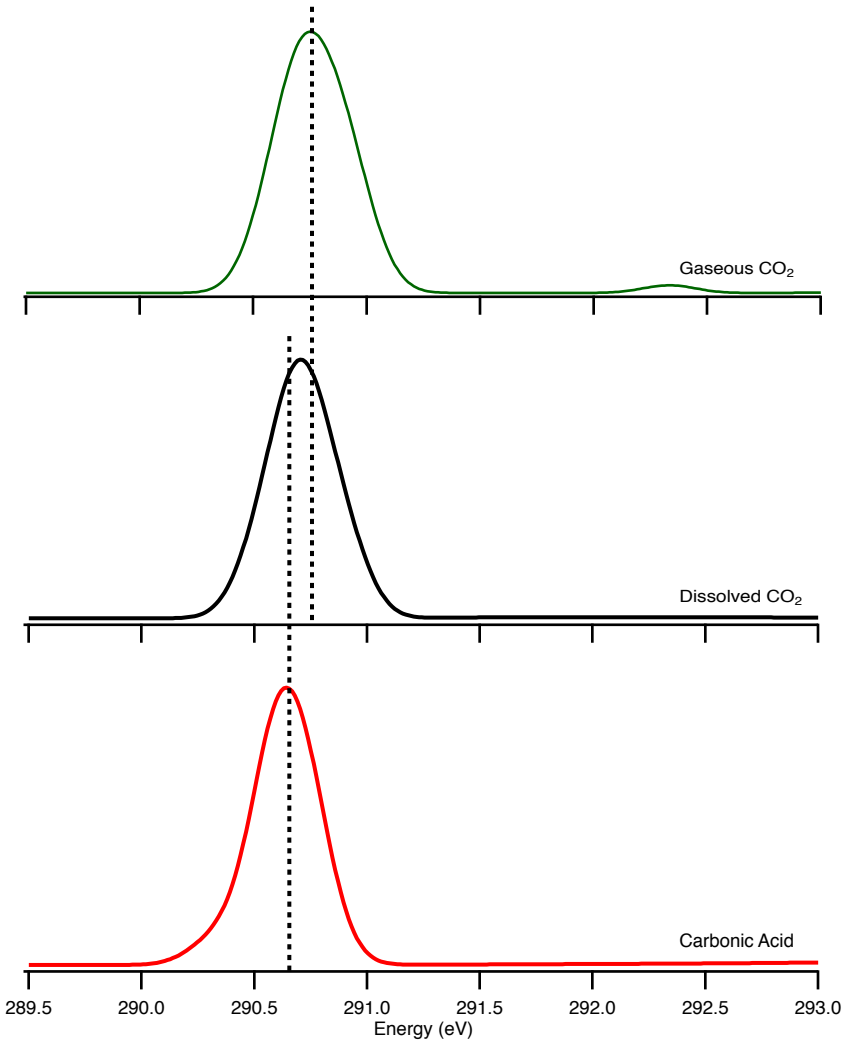

Figure 5.9: Calculated XAS spectra for aqueous carbonic acid (red), dissolved CO_2 (black), and gaseous CO_2 (green). A measurable blue shift is observed between the transition from carbonic acid to gaseous CO_2. Predicted peak maxima are at 290.64 eV (carbonic acid), 290.71 eV (dissolved CO_2), and 290.75 eV (gaseous CO_2).

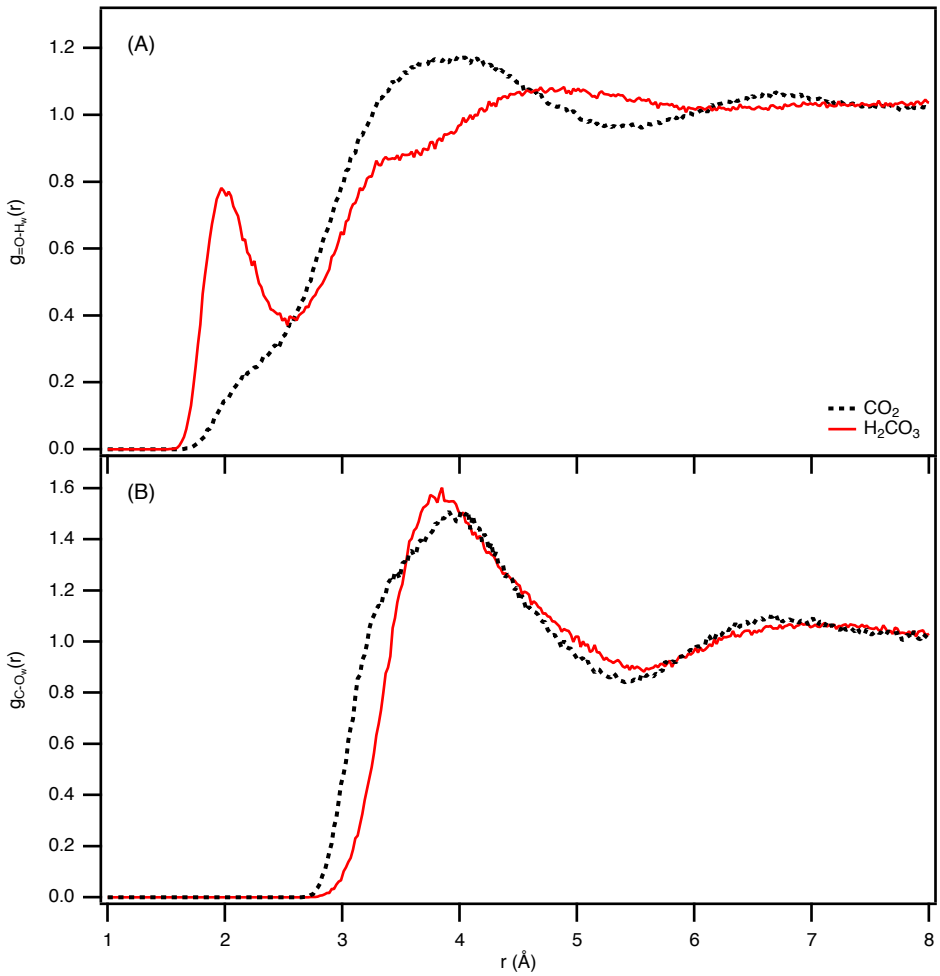

Figure 5.10: Calculated radial distribution functions for aqueous carbonic acid (red) and dissolved carbon dioxide (dashed black). The labels O and C refer to the carbonyl oxygen and carbon respectively. O_w and H_w refer to the oxygens and hydrogens of the water molecules. Bin sizes are 0.02 Å in all cases.

in general agreement with predictions made by Kumar *et al.* wherein CO_2 was predicted to behave as a typical hydrophobic, solute carving out a cylindrical void which enhances the tetrahedral hydrogen bond network of the surrounding solvent [215].

Conclusions

This first characterization of dissolved carbon dioxide under ambient conditions by X-ray absorption spectroscopy and first principles XCH calculations establishes the detailed hydration properties of dissolved carbon dioxide. Calculated spectral energy shifts and intensities between aqueous carbonic acid, dissolved carbon dioxide, and gaseous carbon

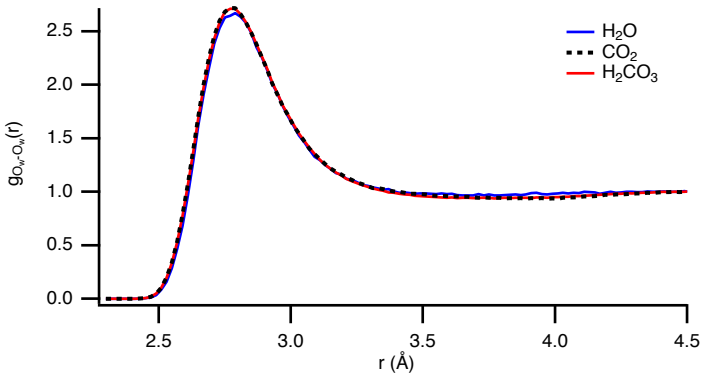

Figure 5.11: Calculated oxygen–oxygen radial distribution functions for pure TIP3P water and for water containing dissolved CO_2 or aqueous H_2CO_3. Both the RDFs of CO_2 and H_2CO_3 exhibit slightly higher first maxima and lower first minima indicating a more ordered liquid structure surrounding the solute. Bin sizes are 0.02 Å in all cases.

dioxide correspond well with experimentally measured spectra. In future studies, we will focus on resolving some limitations of our current experimental design (i.e., finer control over the liquid interaction times) and the limitations of the molecular dynamics modeling through the implementation of higher level *ab initio* theories.

5.3 Reversed Interfacial Fractionation of Carbonate and Bicarbonate evidenced by X-Ray Photoemission Spectroscopy

The material in this section was reproduced, with permission, from: Lam, R. K.; Smith, J. W.; Rizzuto, A. M.; Karslıoğlu, O.; Bluhm, H.; Saykally, R. J. Reversed Interfacial Fractionation of Carbonate and Bicarbonate Evidenced by X-Ray Photoemission Spectroscopy. *J. Chem. Phys.* **2017**, *146* (9), 94703.

Introduction

The aqueous carbonate system is of central importance in nature and has been studied extensively. The species involved – carbon dioxide, carbonic acid, bicarbonate, and carbonate – are involved in both the global carbon cycle and in physiological buffer and respiration systems. Oceanic carbonate chemistry governs CO_2 uptake by surface waters, and the subsequent saturation of carbonate has a significant role in biomineralization in marine organisms and in ecosystems [46, 225]. In mammalian systems, the carbonate buffer system regulates blood pH and is responsible for CO_2 transport across membranes [221]. Clearly, understanding aqueous carbonate chemistry is also central to efforts involved in mitigating the effects of climate change (e.g., carbon capture, sequestration, etc.) [222, 226, 245]. Consequently, much effort has addressed the aqueous carbonate system, dating back over a century [246] with past experimental studies characterizing the kinetic, thermodynamic, and structural properties of these species in aqueous solution and in ice matrixes [42, 44, 45, 50, 198, 201, 202, 212, 223, 237, 247, 248]. Recent theoretical studies, employing molecular dynamics and *ab initio* quantum calculations, have sought to characterize the thermodynamic and mechanistic details of their hydration and chemical reactions [209, 217, 218, 238, 240, 241, 249, 250].

The nature of the ions and their effects on the water structure at the air/water interface critically influence the uptake of atmospheric gases such as carbon dioxide, which is subsequently hydrolyzed to bicarbonate and carbonate. The aqueous bicarbonate and carbonate ions present at the air/water interface have previously been examined by vibrational sum frequency generation (VSFG), finding that the carbonate ion has a significant effect on the orientation and structuring of interfacial water [56–58]. These VSFG studies probe the interfacial water structure, focusing on the –OH stretching region of the vibrational spectrum, and are thereby an indirect probe of the ion. In contrast, X-ray photoemission spectroscopy (XPS) is an atom-specific probe of a system's occupied states, which enables both system composition and depth profiling. Depth profiling is achieved through the exploitation of the effective attenuation length (EAL) of the emitted photoelectrons, viz., photoelectrons with energies near 200 eV selectively probe the interface to depths of ∼20 Å, whereas those with higher kinetic energies typically have longer EALs and thereby probe deeper below the surface (e.g., ∼60 Å at 800 eV) [251]. Additionally, the measured binding energies characterize

the oxidation state of the probed atoms. The development of ambient pressure photoemission spectroscopy by Siegbahn *et al.* opened the field to the study of liquid interfaces[252] either in the presence of the equilibrium vapor pressure [253] or under vacuum conditions, as in the liquid microjet photoemission spectroscopy experiments first performed by Faubel *et al.* [25], and has since been applied to the study of a wide range of liquid systems [120, 254–257]. The spatial distribution of K^+ and CO_3^{2-} in an aqueous solutionwas previously investigated using XPS by Brown *et al.*, who concluded that the cation resides slightly closer to the interface than the anion [258].

Here, we present a study of sodium carbonate (Na_2CO_3), sodium bicarbonate ($NaHCO_3$), and carbonic acid (H_2CO_3) via liquid microjet XPS. We have previously explored the aqueous carbonate system using liquid microjet X-ray absorption spectroscopy (XAS), a complementary technique which probes the unoccupied states of a system; this enabled the detailed characterization of the hydration structure of Na_2CO_3, $NaHCO_3$, H_2CO_3, and dissolved CO_2 [33, 34, 41]. Building on those results, the measurement of XPS spectra at different incident photon energies, ranging from 490 eV to 1090 eV, has permitted the characterization of the surface fractionation of the individual ions. Investigating 50:50 mixtures of Na_2CO_3:$NaHCO_3$ and H_2CO_3:$NaHCO_3$ reveals that both Na_2CO_3 and H_2CO_3 are present in greater concentrations than that of $NaHCO_3$ in the probed interfacial region.

Materials and Methods

A. Sample Preparation

Solutions were prepared using 18.2 MΩ·cm resistivity water obtained from a Millipore purification system. Concentrated HCl (12.1 M) was obtained from Baker. Na_2CO_3 (>99.5% purity) was obtained from Fisher Chemical. $NaHCO_3$ (>99.7% purity) was obtained from Macron Fine Chemicals.

The solutions probed by XPS are detailed in Table 5.1.

Table 5.1: Aqueous carbonate solutions probed by XPS.

I	0.5 M Na_2CO_3
II	0.5 M $NaHCO_3$
III	0.5 M H_2CO_3 (1 M $NaHCO_3$ + 1 M HCl)
IV	50:50 Na_2CO_3:$NaHCO_3$ (1 M Na_2CO_3 + 1 M $NaHCO_3$)
V	50:50 H_2CO_3:$NaHCO_3$ (1 M $NaHCO_3$ + 0.5 M HCl)

The 0.5 M H_2CO_3 solution (**III**) was generated *in situ* using our fast-flow liquid microjet mixing system by mixing solutions of 1 M HCl and 1 M $NaHCO_3$. This mixing system was previously employed in XAS measurements of aqueous H_2CO_3 and dissolved CO_2 [33, 34]. Briefly, a dual syringe pump system (Teledyne-ISCO 260D) drives two solutions through a Microvolume Y-connector. The mixed solution then travels through a 50 μm inner diameter

fused silica capillary to generate the liquid microjet. In this scheme, the interaction time between the two solutions is ∼0.5 ms, facilitating the observation of short-lived species in solution.

The 50:50 mixtures of Na_2CO_3:$NaHCO_3$ (**IV**) were generated by mixing 1 M Na_2CO_3 with 1 M $NaHCO_3$, yielding a 0.5 M concentration of both carbonate and bicarbonate. 50:50 H_2CO_3:$NaHCO_3$ (**V**) was generated by mixing 1 M $NaHCO_3$ with 0.5 M HCl yielding 0.25 M concentrations of both species. To generate mixtures of 50:50 H_2CO_3:$NaHCO_3$ with the same concentration Na_2CO_3:$NaHCO_3$ as the Na_2CO_3:$NaHCO_3$ solution (0.5 M of each ion), a 2 M solution of $NaHCO_3$ would have been required. This exceeds the solubility limit of $NaHCO_3$ in water (96 g/L, 1.14 M). All mixing was done *in situ* within the fast-flow liquid microjet mixing system.

B. Experimental Design

Carbon *1s* and the corresponding valence band X-ray photoemission spectra were measured at Beamline 11.0.2 [259] at the Advanced Light Source (ALS), Lawrence Berkeley National Laboratory (LBNL) using the Ambient Pressure Photoemmision Spectrometer (APPES-II) endstation, which is based on a NAP Phoibos 150 hemispherical analyzer (Specs Surface Nano Analysis GmbH, Berlin). The sample was introduced via a liquid microjet, into the vacuum chamber, operating at a pressure of ∼10 mTorr. The liquid jet is orientated normal to both the electron optical axis of the input lens of the electron spectrometer and the incident X-ray beam. The C *1s* photoemission spectra of aqueous Na_2CO_3 (**I**), $NaHCO_3$ (**II**), and H_2CO_3 (**III**) and 50:50 mixtures of Na_2CO_3:$NaHCO_3$ (**IV**) and H_2CO_3:$NaHCO_3$ (**V**) were measured using incident photon energies of 490 eV, 690 eV, 890 eV, and 1090 eV, resulting in photoelectrons with ∼200, 400, 600, and 800 eV kinetic energy, respectively. To account for shifts induced by charging of the liquid jet and the detector work function, measured binding energies were aligned to the liquid water $1b_1$ binding energy at 6.5 eV [260].

Results and Discussion

The C *1s* and their respective valence band photoemission spectra, measured with an incident photon energy of 490 eV, are shown in Figure1 for 0.5 M solutions of sodium carbonate, sodium bicarbonate, and carbonic acid (**I**–**III**). A large systematic shift to higher binding energies is observed between the various carbonate species, from carbonate to carbonic acid. Measured binding energies are Na_2CO_3 (289.1 eV), $NaHCO_3$ (290.1 eV), and H_2CO_3 (291.0 eV) with corresponding FWHMs of 1.1 eV, 1.1 eV, and 1.3 eV, respectively. The spectra shown in Figure 5.12 are background-corrected using a linear baseline subtraction but are otherwise unnormalized. As the photoemission cross sections are not expected to differ significantly between the various carbonate species, the drastic difference observed in the intensity between species is striking. The spectra of both sodium carbonate and carbonic acid exhibit higher intensity than that of the sodium bicarbonate. To account for

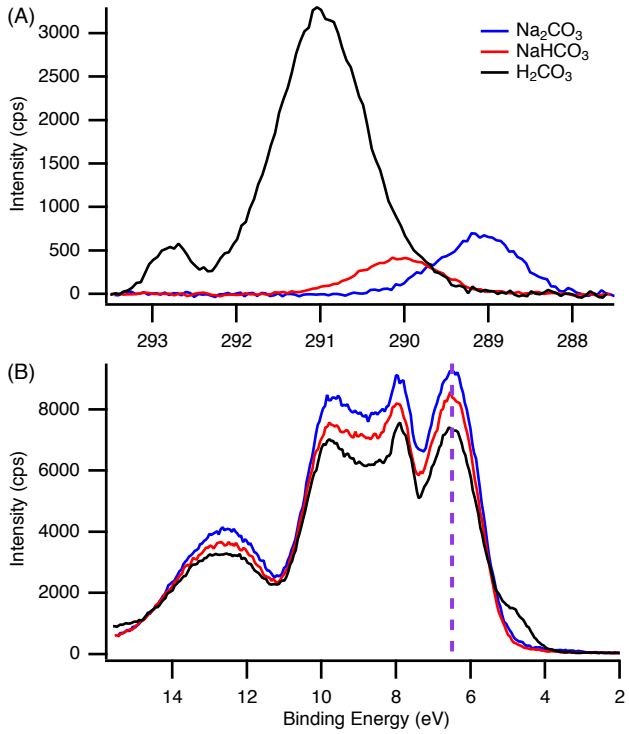

Figure 5.12: X-ray photoemission spectra with an incident photon energy of 490 eV. (A) Measured C *1s* binding energies for 0.5 M solutions of Na_2CO_3 (solution **I**, blue), $NaHCO_3$ (solution **II**, red), and H_2CO_3 (solution **III**, black). The low intensity peak centered at 292.8 eV corresponds to gas phase CO_2. (B) Measured valence band photoemission spectra for the respective solutions. The energy axes, for all measurements, were aligned relative to water $1b_1$ feature, located at 6.5 eV (dashed purple line).

differences in alignment between the liquid jet, the incident X-ray beam, and the detector, the spectra were scaled, relative to the valence band intensity of sodium carbonate. The measured signal intensity in the valence band spectra primarily corresponds to that of the water valence band photoemission, which is largely unchanged upon the addition of 0.5 M solute. The scaled spectra, which also exhibit this anomalous difference in intensity, are shown in Figure 5.13. Relative to that of sodium bicarbonate, the signals originating from carbonate and carbonic acid solutions are ∼1.5 and ∼10.2 times larger, respectively.

The measured carbonate and bicarbonate spectra were fit to single Gaussians while the carbonic acid spectrum was fit to two Gaussian peaks due to the presence of a small peak at ∼292.8 eV corresponding to a gas phase CO_2 background present in the chamber resulting from the decomposition of H_2CO_3 to form CO_2 and H_2O. The fitted peaks, shown in Figure 5.14, reproduce the measured spectra well and were used to deconvolute the spectra of Na_2CO_3:$NaHCO_3$ (**IV**) and H_2CO_3:$NaHCO_3$ (**V**) mixtures.

Figures 5.15 and 5.16 show the measured photoemission spectra (black and green mark-

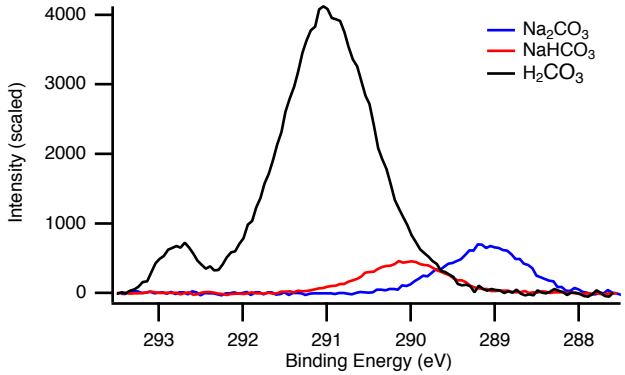

Figure 5.13: Scaled C *1s* X-ray photoemission spectra for 0.5 M solutions of Na_2CO_3 (solution **I**, blue), $NaHCO_3$ (solution **II**, red), and H_2CO_3 (solution **III**, black). Spectra were scaled relative to the valence band intensity of Na_2CO_3 to account for intensity differences originating from the liquid jet alignment. Applied scaling factors are Na_2CO_3 (1.0), $NaHCO_3$ (1.1), and H_2CO_3 (1.25).

ers) for 50:50 mixtures of Na_2CO_3:$NaHCO_3$ (**IV**) and H_2CO_3:$NaHCO_3$ (**V**) at incident photon energies of 490 eV, 690 eV, 890 eV, and 1090 eV. The differences in intensity that were observed in the single component solutions are clearly maintained in these mixtures, although at slightly different ratios. The measured photoemission spectra of the mixtures were fit by fixing the width and center obtained from the Gaussian fits of the single component solutions shown in Figure 5.14 and varying only the amplitudes of the Gaussians. For the spectra measured at energies higher than 490 eV, the relative centers of the Gaussians between species were maintained. The fitted spectra are shown in the solid black and solid green lines in Figures 5.15 and 5.16, respectively, exhibit excellent agreement with the measured spectra. The individual components of the fit are shown in blue (Na_2CO_3), red ($NaHCO_3$), black (H_2CO_3), and purple (CO_2 gas).

The peak area ratios for 50:50 mixtures of Na_2CO_3:$NaHCO_3$ (**IV**) and H_2CO_3:$NaHCO_3$ (**V**) are plotted as a function of electron kinetic energy (eKE) in Figure 5.17. As the electron kinetic energy increases, the peak area ratio between the probed species approaches a limit of unity, as would be expected for an equimolar mixture. However, our results indicate that concentrations of both Na_2CO_3 and H_2CO_3 are significantly enhanced relative to that of $NaHCO_3$ throughout the probed region. While the enhancement of a neutral acid (H_2CO_3) over a charged ion (HCO_3^-) is not surprising, and has previously been observed for protonated acetic acid [52], the significant enhancement of CO_3^{2-} over HCO_3^- appears to conflict with recent models for interfacial ion adsorption. Historically, it had been assumed that all ions were repelled from the air/water interface. This repulsion was originally explained by classical electrostatic theory [261] and supported by surface tension measurements which showed that the surface tension increased as a function of salt concentration [262, 263]. More recently, molecular dynamics simulations [264, 265], surface specific second-order nonlinear optical experiments [103, 266, 267], and XPS measurements [253, 257] have predicted and ob-

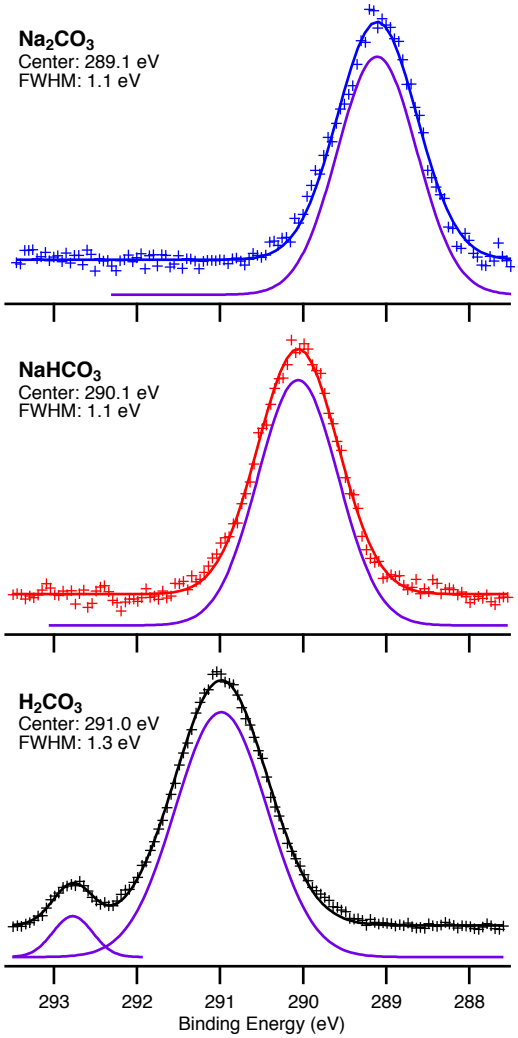

Figure 5.14: Gaussian fits for the measured C *1s* X-ray photoemission spectra for Na_2CO_3 (solution **I**, top), $NaHCO_3$ (solution **II**, middle), and H_2CO_3 (solution **III**, bottom) with an incident photon energy of 490 eV. The experimental measurement is represented by the markers (+), and the solid blue, red, and black lines correspond to the respective fit curves for Na_2CO_3, $NaHCO_3$, and H_2CO_3. The individual Gaussian peaks are represented by the offset solid purple lines. Measured binding energies are Na_2CO_3 (289.1 eV), $NaHCO_3$ (290.1 eV), and H_2CO_3 (291.0 eV) with corresponding FWHMs of 1.1 eV, 1.1 eV, and 1.3 eV, respectively.

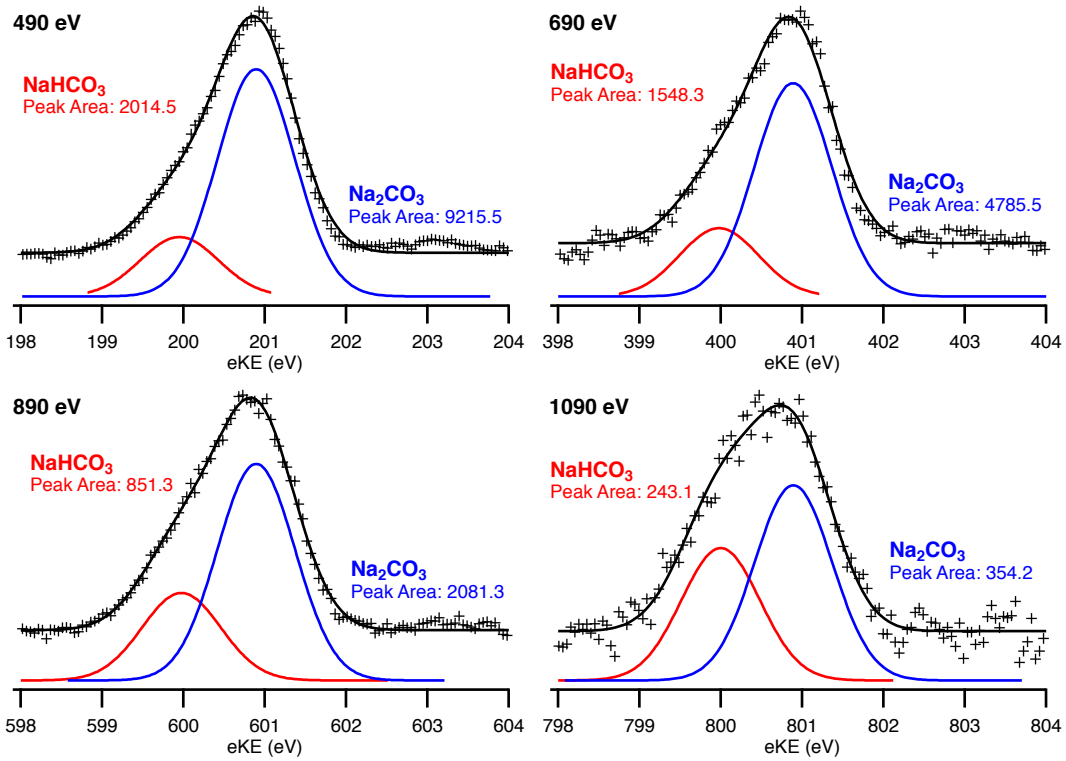

Figure 5.15: Measured X-ray photoemission spectra of 50:50 Na_2CO_3:$NaHCO_3$ mixtures (solution **IV**) at 490 eV, 690 eV, 890 eV, and 1090 eV incident photon energies, corresponding to electron kinetic energies (eKE) of 200 eV, 400 eV, 600 eV, and 800 eV, respectively. The measured spectra were fit with two Gaussian peaks with the same parameters (width, center) as those measured for the pure components (Figure 5.14). Peak areas represent the absolute area in the measured spectrum. The decrease in absolute signal as the photon energy is increased is a result of the reduction in photoemission cross section.

served the enhancement of certain simple ions at the air/water interface. These models have shown that weakly hydrated, charge-diffuse ions are generally enhanced at the air/water interface [53–55]. Our current experiments suggest that carbonate, a strongly hydrated doubly charged anion, is present in higher concentrations than is the singly charged, less strongly hydrated, bicarbonate anion in the probed region. This can be rationalized if carbonate adsorbs to the air/water interface as an ion pair with sodium (Na^+:CO_3^{2-}). Adsorption to the air/water interface as a contact ion pair has previously been observed, in both experiment and theory, for aqueous solutions of strong acids [109, 268, 269]. In previous VSFG measurements, carbonate was shown to exert a much larger effect on the interfacial water than does bicarbonate [56, 57]. More recently, Allen *et al.* employed phase sensitive VSFG measurements, finding that bicarbonate is accommodated by the interfacial region while carbonate is excluded [58]. In these experiments, the presence of aqueous carbonate was found

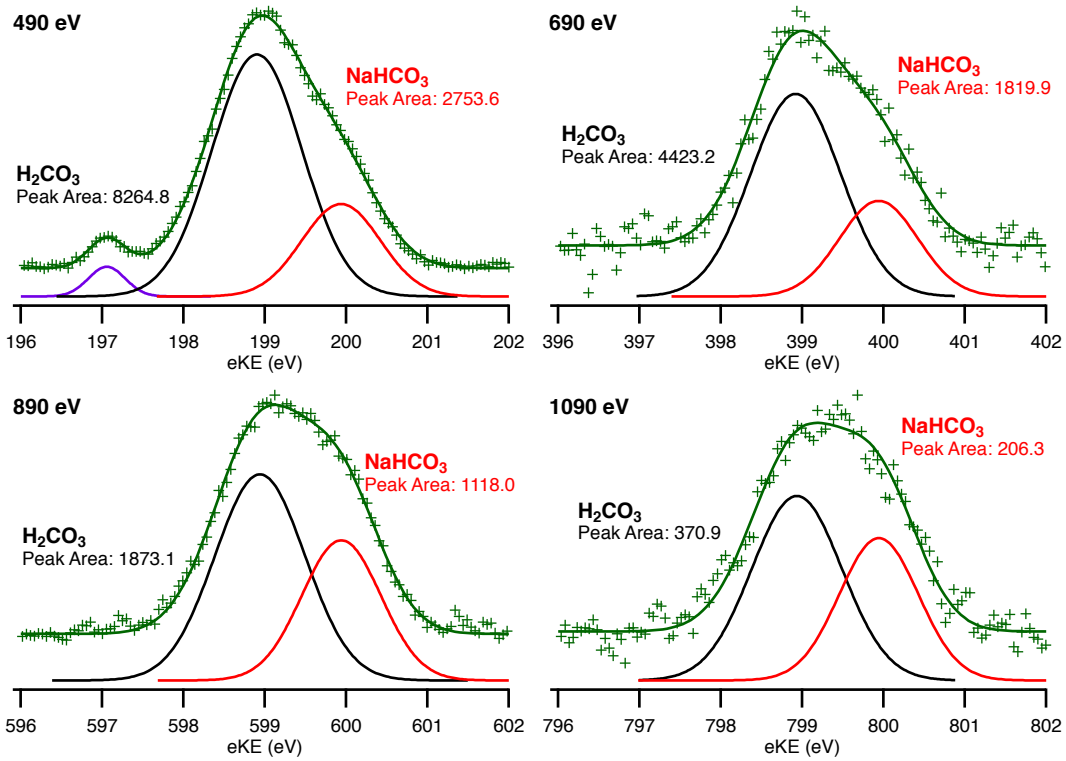

Figure 5.16: Measured X-ray photoemission spectra of 50:50 H_2CO_3:$NaHCO_3$ mixtures (solution **V**) at 490 eV, 690 eV, 890 eV, and 1090 eV incident photon energies, corresponding to electron kinetic energies (eKE) of 200 eV, 400 eV, 600 eV, and 800 eV, respectively. The measured spectra were fit with two Gaussian peaks with the same parameters (width, center) as those measured for the pure components (Figure 5.14). Peak areas represent the absolute area in the measured spectrum. The decrease in absolute signal as the photon energy is increased is a result of the reduction in photoemission cross section.

to reorient the surface waters so that the water hydrogens point downward into the bulk.

While these VSFG results appear to conflict with the present XPS measurements, they are not necessarily irreconcilable. Second order nonlinear experiments probing the air/water interface are sensitive only to regions of broken inversion symmetry. While the exact thickness of the probed interfacial region is not quantified, the penetration depth of the probe is approximately half the input wavelength. In aqueous systems containing simple ions, the probe depth is likely less than 1 nm. However, in systems with a more complex depth profile a greater depth may be accessible [270]. Theoretical models typically define the interface in terms of the Gibbs dividing surface, wherein the solvent density reaches half of the bulk density. In either case, these measurements are certainly more surface specific than our low-energy XPS measurements, wherein the effective attenuation length of an electron in water is at a minimum ($\sim$2 nm) when the electron has a kinetic energy of $\sim$200 eV. As such, even

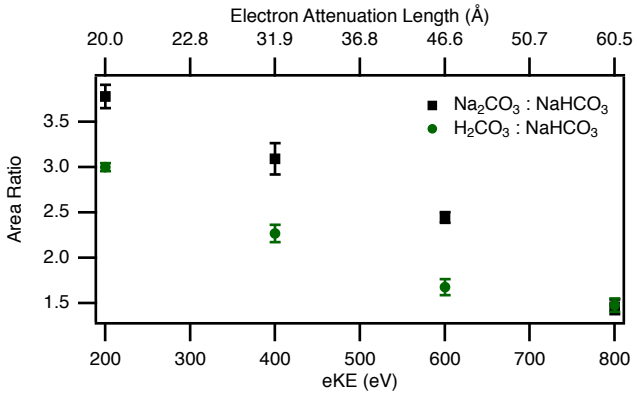

Figure 5.17: Peak area ratios vs. eKE for 50:50 Na_2CO_3:$NaHCO_3$ mixtures (solution **IV**) and 50:50 H_2CO_3:$NaHCO_3$ mixtures (solution **V**). Corresponding approximate electron attenuation length values adapted from Ottosson *et al.* [251].

with 200 eV photoelectrons, a significant proportion of the signal arises from photoelectrons generated 2–5 nm below the surface. At 800 eV, the EAL is ∼6 nm. Although the EAL is expected to vary slightly with system composition, we do not expect these variations to affect our interpretation as the EAL should always increase as a function of eKE from 200 eV to 800 eV. Our results would therefore indicate that there exists a significant accumulation of CO_3^{2-} below the depletion region outside of the region probed by the SFG measurements.

Conclusions

We have presented the X-ray photoemission spectra of aqueous solutions of Na_2CO_3, $NaHCO_3$, and H_2CO_3 which exhibit a systematic shift to higher measured C *1s* binding energies from carbonate to carbonic acid. The measured spectra of 50:50 mixtures indicate that both carbonate and carbonic acid are present at higher concentrations in the probed region than bicarbonate. Further theoretical modeling is required to address the apparent conflict with current models describing ion adsorption to aqueous interfaces, which would suggest that the singly charged anion, bicarbonate, should be present in higher concentrations relative to the doubly charged carbonate anion. This new result could reflect interesting and important differences in the hydration and counterion interactions (i.e., ion pairing) of the carbonate species.

Chapter 6

Soft X-Ray Nonlinear Spectroscopy

6.1 Soft X-ray Second Harmonic Generation as an Interfacial Probe

Nonlinear optics has recently been extended from visible and near UV wavelengths to new regimes with the development of X-ray free electron lasers (XFELs) capable of delivering X-ray pulses with high brightness, ultrashort pulse duration, and high coherence [62–64, 271–274]. One fundamental nonlinear probe is second harmonic generation (SHG), a second-order process which combines two photons of the same energy to generate a single photon with twice the energy [275]. At infrared, visible, and ultraviolet wavelengths, second-order nonlinear spectroscopies have become important tools in surface science, as symmetry considerations, within the dipole approximation, constrain signal generation to regions lacking centrosymmetry, such as surfaces and interfaces [267, 276–278]. In contrast, at hard X-ray wavelengths, second harmonic and sum frequency generation (SFG) have been observed in centrosymmetric materials with a non-uniform electron density and are essentially bulk probes [62, 63]. As soft X-ray wavelengths fall in between the hard X-ray and UV regimes, there has been uncertainty regarding the interface specificity of soft X-ray SHG. Here, by utilizing a recently constructed, highly coherent, soft X-ray free electron laser [279, 280], we report the first observation of soft X-ray second harmonic generation near the carbon K-edge ($\sim$284 eV). Our experimental results and accompanying theoretical analysis indicate that soft X-ray SHG is an interface specific probe with symmetry constraints similar to optical SHG/SFG, and is highly sensitive to resonance effects. This enables a powerful new approach for surface and interface analysis with broad applicability to many scientific fields, as it combines the elemental and chemical specificity of X-ray absorption spectroscopy with the rigorous interfacial specificity of second-order nonlinear spectroscopies, while maintaining a fully coherent signal. With several new coherent free electron lasers under development (SwissFEL, SXFEL, LCLS-II, FLASH2020) [281, 282], this new technique offers exciting applications to a wide range of problems.

At optical wavelengths, second-order nonlinear spectroscopies have become indispensable

techniques for surface analysis, being among the few techniques with genuine interface specificity. As such second harmonic generation (SHG) and sum frequency generation (SFG) have been employed to study of a wide range of scientifically important systems (e.g., liquid/vapor interfaces, catalytic interfaces, etc.) [277]. These techniques exploit the enhancement of the second-order nonlinear response to a high intensity, coherent photon beam when either the intermediate or final state is resonant with a real state within the target material. The nonlinear response to a coherent input beam of frequency ω can be derived from an expansion of the polarization of the target medium

$$\vec{P} = \vec{X}^{(1)}E + \vec{X}^{(2)}EE + \vec{X}^{(3)}EEE + ... \tag{6.1}$$

where $\vec{X}^{(n)}$ is the nth order susceptibility tensor. Within the dipole approximation, even orders of $\vec{X}^{(n)}$ necessarily vanish in centrosymmetric media. This causes SHG, SFG, difference frequency generation (DFG), and higher even-order nonlinear signals to be inherently surface specific in centrosymmetric media, as this symmetry is broken only at interfaces. Assuming a broken-symmetry region with thickness much less than the wavelength, the intensity of the SHG signal from a given interface is given by

$$I_{2\omega} \propto |X^{(2)}_{eff}|^2 I^2_{\omega} \tag{6.2}$$

where $X^{(2)}_{eff}$ is the effective susceptibility of the interfacial region and I_ω is the intensity of the fundamental beam. Note the quadratic dependence of the second harmonic (SH) intensity $I_{2\omega}$ on the input intensity I_ω.

Until recently, the lack of light sources with sufficient intensity and coherence has limited the development of nonlinear X-ray spectroscopies. Prior to the development of free electron lasers (FELs), only parametric down-conversion had been observed [283]. While the advent of XFELs has recently enabled second- and third-order nonlinear spectroscopies at hard X-ray energies, including SHG [62], SFG [63], two-photon absorption [64], and inelastic Compton scattering [65], current hard X-ray FELs lack the longitudinal and temporal coherence necessary for efficiently satisfying the phase-matching conditions required for nonlinear spectroscopies, thus making the exploitation of some of these techniques difficult [66, 67]. Furthermore, the shorter hard X-ray wavelengths ($\lambda < 0.2$ nm) induce second harmonic and sum frequency generation even within centrosymmetric media, as the observed response depends on material inhomogeneity on the length scale of the X-ray wavelength, similar to how SHG is seen in a plasma, and effectively making this method a bulk probe [68].

Here we report the observation of soft X-ray SHG generated by high intensity, coherent FEL pulses at FERMI, a highly coherent soft X-ray FEL based on high-gain harmonic-generation (HGHG) of a longer wavelength seed laser [279, 280]. The experiments were conducted at the EIS-TIMEX endstation [284, 285]. An experimental schematic is shown in Figure 6.1 A: a soft X-ray FEL pulse (estimated pulse duration ∼25 fs, pulse energy ∼1–5 μJ, spot size ∼350 μm^2) is passed through a 2 mm iris to attenuate the off-axis second harmonic contamination from the FEL source, and focused onto a graphite sample at normal incidence. The transmitted beam and the collinear SH signal are passed through

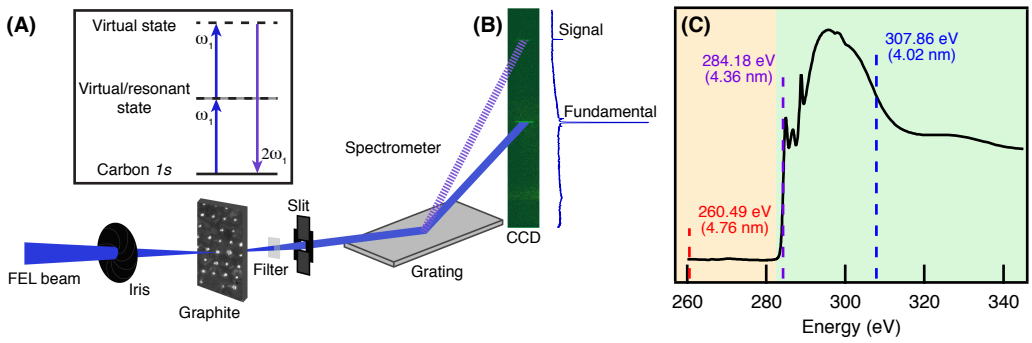

Figure 6.1: Experimental design. (A) X-ray pulses are passed through a 2 mm iris, then focused by an ellipsoidal mirror (not shown) onto the graphite sample (spot size $\sim$350 μm^2) at normal incidence. The transmitted beam and the collinear second harmonic signal (double the fundamental photon energy) are passed through a 600 nm aluminum filter and into a spectrometer, spatially separating the second harmonic signal from the fundamental. A schematic energy level diagram of the SHG process is shown in the inset. (B) The CCD image and projection of the transmitted FEL beam and the SHG signal for a single FEL pulse. (C) Linear, total electron yield (TEY) X-ray absorption spectrum of a 500 nm graphite sample. X-ray SHG measurements were made at the three discrete photon energies (ω_1) shown in the dashed lines. The non-resonant and resonant regions are shaded in orange and green, respectively.

a 600 nm aluminum filter to attenuate the fundamental FEL pulse, into a spectrograph [286] to separate the SH signal from the fundamental, and onto a CCD detector (Figure 6.1B). The sample was raster scanned so that pristine graphite was probed with each laser pulse. Measurements were made using three discrete wavelengths chosen to have incoming photon energies lying below (λ = 4.76 nm; $\hbar\omega$ = 260.5 eV), on (λ = 4.36 nm; $\hbar\omega$ = 284.18 eV), and above (λ = 4.02 nm; $\hbar\omega$ = 307.86 eV) the carbon K-edge absorption edge of graphite (see Figure 6.1C) to demonstrate the effects of resonant enhancement. In this case, the FEL energy is resonant with the intermediate state and generates a non-resonant signal, enabling transmission experiments. SHG spectra can also be measured at half the photon energy used here, where the final state is resonant although this would hinder transmission studies. Measurements were made both with and without the sample present to permit subtraction of any remaining second harmonic contamination from the FEL beam.

The measured dependence of the second harmonic signal on the pulse energy for multiple thicknesses of graphite (100–720 nm) corresponding to 260.49 eV, 284.18 eV, and 307.86 eV is shown in Figures 6.2A, 6.2B, and 6.2C, respectively. The pulse energy was calculated from the absolute number of X-ray photons incident on the sample, which was directly measured by the spectrometer with the sample removed. A quadratic fit to the SH response with respect to input intensity at a given photon energy is represented by a dashed line. At each photon energy, the power dependence of the SH signal is largely invariant with sample thickness, an observation that is consistent with surface sensitivity in a centrosymmetric sample. Notably,

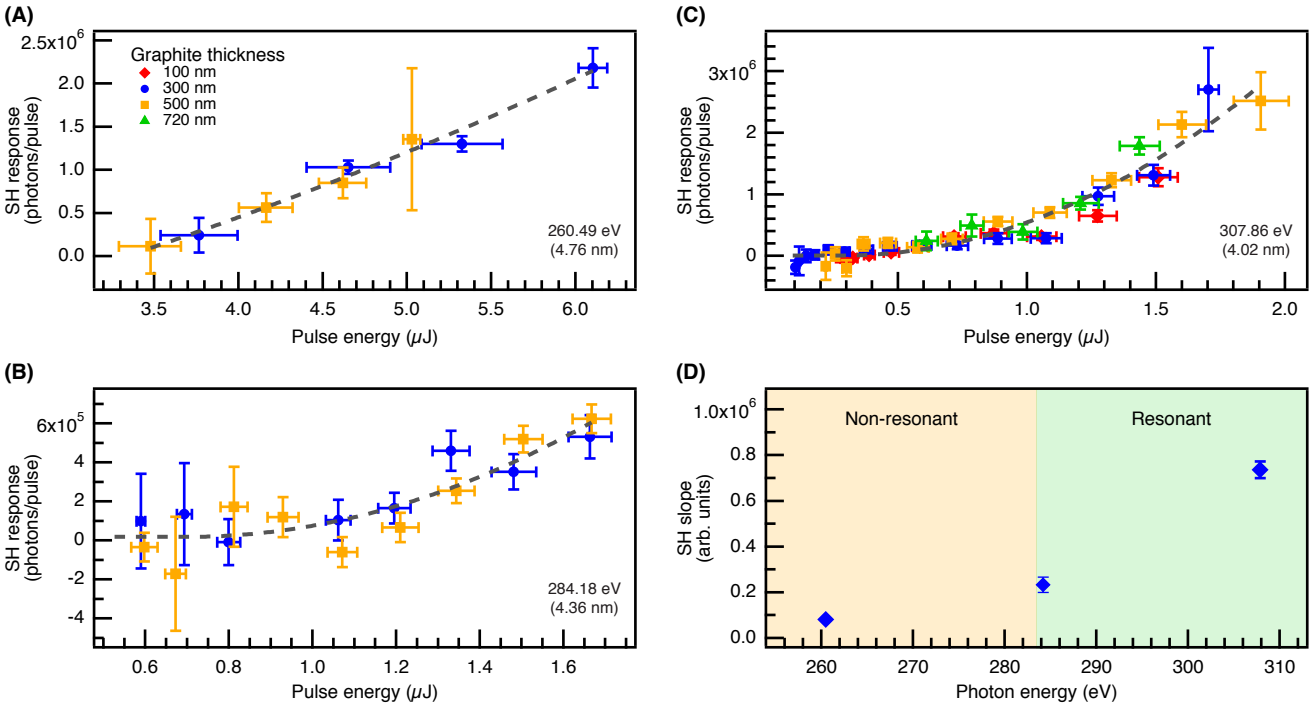

Figure 6.2: Pulse energy dependence of soft X-ray SHG. The second harmonic response at 260.49 eV (A), 284.18 eV (B), and 307.86 eV (C), of graphite thin films (100 nm, red diamond; 300 nm, blue circle; 500 nm, orange square; 720 nm, green triangle). The dashed lines represent quadratic fits to all the points at a given photon energy, constrained to show no detectable second harmonic signal generated below a threshold pulse energy. The vertical and horizontal error bars represent the standard error of the SH response and the standard deviation of the pulse energies in each bin, respectively. (D) The slope of the linearized pulse energy dependence curve for each photon energy. The relative $X^{(2)}_{eff}$ response is proportional to the slope of the linearized pulse energy dependence curve (SH response vs. [input power]^2). Error bars represent the standard deviation from the linear regression analysis. The non-resonant and resonant regions are shaded in orange and green, respectively.

even for thin samples with a large transmission (>70%), a thickness-dependent increase in the SH signal is not observed, implying that the signal is not bulk-volume dependent. This invariance with sample thickness is also observed at resonant photon energies. The bulk second harmonic signal in graphite, due to electric quadrupole contributions, is weak.

At the resonant photon energies, a significant enhancement of the SH signal was observed, permitting its detection with significantly lower pulse energies. The tunable nature of FELs facilitate resonance, and double resonance exploitation. The measured relative $X^{(2)}_{eff}$ response of graphite at different X-ray wavelengths is proportional to the slope of the linearized power dependence curve (SH response vs. [input power]^2), shown in Figure 6.2D. A significant enhancement in the $X^{(2)}_{eff}$ response is observed when exciting with X-ray energies at or above the graphite absorption onset (>284 eV). In this case, the intermediate state is resonant with real transitions (Fig 6.1C), and the data are consistent with the expected resonant enhancement of the SH signal when either the intermediate or final state is real. When off-resonance at 260.49 eV, a threshold pulse energy of over 1 μJ per pulse is required for a sufficient SH signal-to-noise ratio as determined based on the minimum of the quadratic fits shown in Figure 6.2. On resonance, the pulse energy necessary is significantly lower, viz. 0.7 μJ and 0.3 μJ at 284.18 eV and 307.86 eV, respectively. This resonance enhancement means that the technique can be used to generate a surface specific soft X-ray spectrum with sensitivity to chemical composition. The pump intensities used here correspond to peak fields of 10^{12} W/cm^2, which is 4 orders of magnitude less than what was required for hard X-ray SHG (10^{16} W/cm^2) [62]. While the exact damage threshold will vary based on the sample, we expect that it will be possible to perform soft X-ray SFG below the damage threshold for a broad variety of materials, by leveraging the lower X-ray fields required by combining the soft X-ray pulse with an optical laser pulse. When hard X-ray SFG was performed by using an optical laser pulse combined with an X-ray laser, the pump intensities were ca. 10^{10} W/cm^2 for the optical laser and 10^{11} W/cm^2 for the X-ray laser [63]. Additionally, as soft X-ray SHG requires significantly smaller fields than does hard X-ray SHG, such damage-free SHG measurements may be achievable by exploiting higher repetition rate FELs (LCLS-II, FLASH2020) and more efficient detection (better spectrometer, spatial separation, etc.).

In order to verify our experimental observation of a significant SHG response in the soft X-ray regime of graphite, we calculated the linear and second-order response from first principles using perturbation theory within density functional theory [287, 288]. This approach is broadly applicable for calculating electronic SHG and SFG spectra, from the optical regime through the X-ray energies, and is detailed below. Figures 6.3A and 6.3B present the linear and SH response, respectively, of an 8-layer slab of AB stacked hexagonal graphite. A better comparison to experiments can be obtained by sampling a finite temperature molecular dynamics trajectory, as has been demonstrated for linear absorption [289]. Nevertheless, the linear absorption spectrum calculated here within the independent particle approximation captures salient resonant features, such as π^* and σ^* features at 284.9 and 291.65 eV, compared to the respective experimental values of 284.9 and 288.8 eV. Due to symmetry considerations, only the X_{zzz} component of the $X^{(2)}$ susceptibility tensor is non-vanishing.

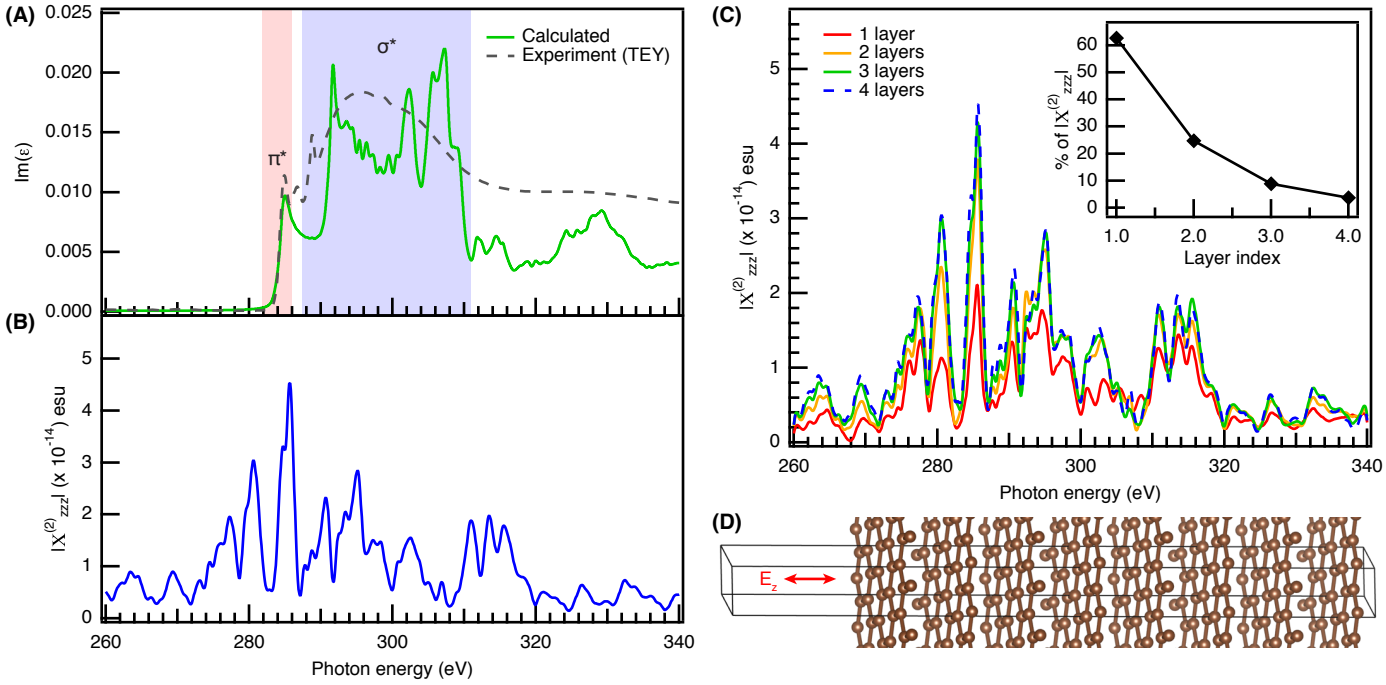

Figure 6.3: Second harmonic susceptibility from first principles theory. (A) Imaginary part (black, solid) of the linear dielectric function corresponding to the calculated linear spectrum at the C K-edge NEXAFS region calculated with a density functional theory based supercell approach for an 8-layer slab of graphite compared with the experimental linear spectrum (dashed grey, dashed). The π^* and σ^* transitions are labeled in red and blue, respectively. The experimental peak between the marked π^* and σ^* regions corresponds to oxidized graphite. Note that a more realistic comparison between theory and experiment can be obtained by sampling a finite temperature molecular dynamics simulation as inhomogeneity in thermalized samples is a significant contributor to spectral broadening. (B) Calculated C *1s* core-level contribution to the magnitude $|X^{(2)}_{zzz}|$ of the zzz component of the second-order nonlinear susceptibility tensor $X^{(2)}(2\omega, \omega, \omega)$ relevant to SHG near the C K-edge of a graphite surface. C *1s* core-levels from the top four surface layers of an 8-layer slab of graphite (shown in D) are considered in the simulation. The z axis is perpendicular to the surface of the slab. (C) Convergence of the calculated $|X^{(2)}_{zzz}|$ as a function of the number of surface layers whose C *1s* core-states are included in the simulation. The inset shows the percentage contribution to $|X^{(2)}_{zzz}|$ from each of the top four individual layers, obtained by integrating $|X^{(2)}_{zzz}|$ over a 260–340 eV energy window, plotted as a function of layer index. Contribution to the overall response is seen to decay exponentially moving into the bulk of the slab with the top layer accounting for ∼63% of the signal. (D) Periodic supercell of the 8-layer graphite slab employed in the simulations.

Small changes in the energy calibration and temperature effects in the theory and the imperfect materials used in the experiments can engender large differences in signal intensity, particularly near the absorption edge, likely accounting for the observed differences between experiment and theory. The main features in the SH spectrum correspond to excitations from a convolution of the ground state and π^* and σ^* intermediate states in the conduction band. As such, a direct comparison between the SH spectrum and the linear spectrum is infeasible.

The signal originating from each layer of the graphite slab was isolated, in order to determine the exact degree of surface specificity. As shown in the inset of Figure 6.3C, the contribution to the overall response decays exponentially as a function of layer index and is essentially limited to the first three monolayers, or ∼0.5 nm, with ∼63% of the signal originating from the topmost layer, ∼25% from the second, and ∼9% from the third. This result is consistent with expectations from optical sum frequency generation, wherein 90% of the signal originates from the first 2 molecular layers [290].

In conclusion, soft X-ray second harmonic generation is demonstrated to be a powerful elemental and chemical specific spectroscopy that is highly symmetry sensitive. This new technique will permit a new class of interface analysis experiments with significantly higher interfacial specificity than existing soft X-ray methods, effectively allowing for X-ray absorption spectroscopy of the first few molecular layers of an exposed bulk sample or either side of a buried interface. For example, buried interfaces in layered samples, wherein an individual layer contains an element not present in the others, could be probed directly without concomitant contamination from the exposed interfaces. Additionally, as the pulses remains fully coherent, it should be possible to combine this technique with lensless coherent imaging techniques with a resolution not limited by aberration [69]. Such a technique would require either an energy-sensitive nondispersive detector or the generation of a signal that is spatially separated from the input pulses, as has been achieved previously with non-collinear input laser pulses, such as in optical SFG [267, 276–278]. If radiation damage concerns can be mitigated, the spectral sensitivity demonstrated here would enable experiments which can both spectroscopically and spatially resolve nanoparticles. Such measurements, when combined with the first-principles electronic structure framework developed here, will have broad applicability to a variety of systems of current interest.

Samples

Unsupported nanocrystalline graphite thin films (thickness: 100, 300, 500, 720 nm), mounted onto L1.0 rings (10 mm diameter), were purchased from Lebow Company (Goleta, CA).

Experimental Design

The soft X-ray SHG experiment was performed at EIS-TIMEX end-station of the Elastic and Inelastic Scattering (EIS) beamline [284, 285] at the FERMI FEL-2 free electron laser

[279, 280]. FEL-2 is based on a double high gain harmonic generation (HGHG) conversion scheme. The HGHG scheme consists in preparing the electron beam phase space in a first undulator (modulator), where the interaction with an external laser (seed) induces a controlled and periodic modulation in the beam longitudinal energy distribution. The beam propagates through a dispersive section converting the energy modulation into a density modulation. The density modulated beam is then injected in a long undulator (amplifier) where the FEL amplification process is enhanced by the presence of the modulation. This sequence is repeated twice in FERMI FEL-2 in order to achieve high harmonic multiplication factors [280]. The input seed used in this experiment corresponds to the third harmonic of a Ti:Sa oscillator followed by a regenerative amplifier. A further pulse temporal compression stage was set up in the UV to reduce the duration of the seed to 67 fs.

Table 6.1: FERMI FEL pulse characteristics: wavelength (nm), harmonic number, pulse duration (fs), Fourier limited spectral width (σ, nm), measured spectral width (σ, nm), coherence length (μm) and number of shots for various data sets.

Wavelength (nm)	$n \times m$	Estimated duration (FWHM, fs)	Fourier limited spectral width (σ, nm)	Measured (most probable) spectral width (σ, nm)	Coherence length (FWHM, μm)	Shots
4.02	65	22.7	$4.5 \cdot 10^{-4}$	$1.1 \cdot 10^{-3}$	2.7	3398
4.36	60	23.3	$5.1 \cdot 10^{-4}$	$2.0 \cdot 10^{-3}$	1.8	794
4.76	55	24	$5.9 \cdot 10^{-4}$	$2.2 \cdot 10^{-3}$	1.9	479

When the FEL is optimized for maximizing the peak power, in the HGHG process the frequency upshift to harmonic n typically shortens the output pulse by a factor $\sim 7/(6n^{1/3})$ [291]. The three wavelengths used in the experiment correspond to the conversion of the seed to harmonic orders $n = 11$th, 12th, and 13th in the first stage, and harmonic $m = 5$ in the second. We may therefore estimate the pulse shortening corresponding to the double stage conversion of FEL-2 as $(7/6)^2/(nm)^{1/3}$. We have listed the duration estimate for the three wavelengths in Table 6.1, together with the measured spectral width, the expected width for Gaussian Fourier transform limited pulses, and the corresponding coherence length. The spectral width was measured as the most probable value resulting from the statistical analysis of >450 shots at a given wavelength. An example is shown in Figure 6.4, where a typical histogram of the spectral width (σ, nm) is shown at $n = 13$, $m = 5$.

The graphite films were attached to a 5-axis manipulator stage. The sample was rastered ($\sim$50–60 μm) so that pristine graphite was probed with each laser shot, mitigating the effects of sample damage. Between laser shots, the positioning of the sample stage, monitored by a telemicroscope, was moved along the beam axis to ensure that the sample was always at the focal point of the ellipsoidal mirror.

Photons from the FEL source are transported to the endstation along the Photon Analysis, Delivery, and Reduction System (PADReS) [292], which also provided shot-to-shot

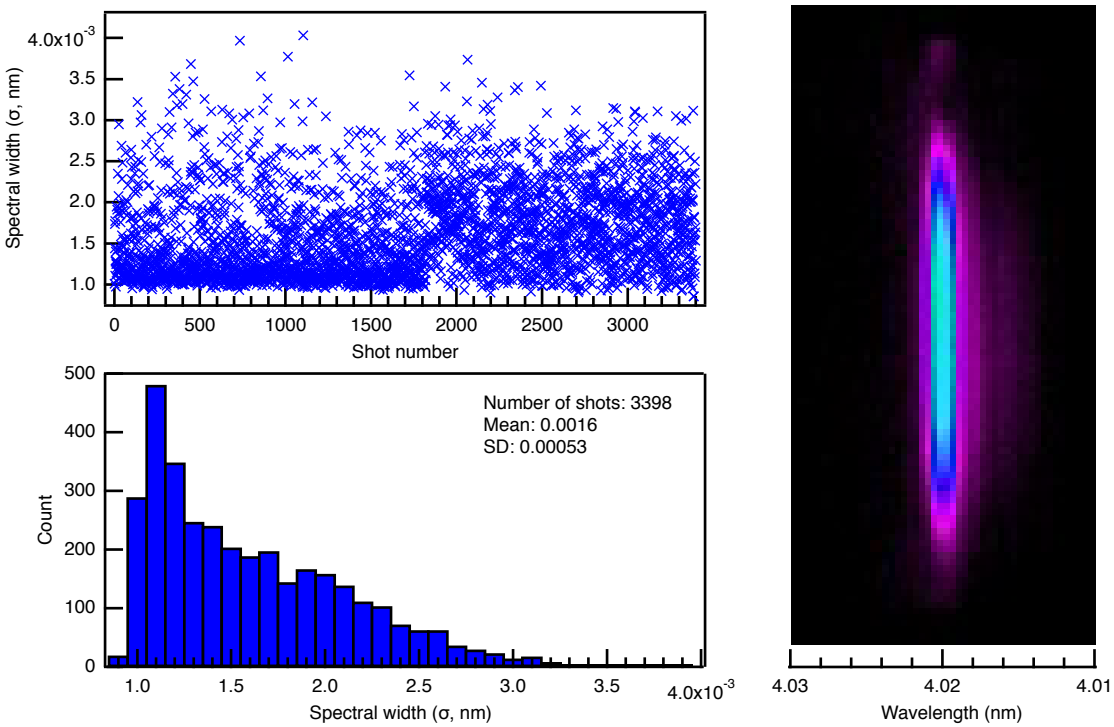

Figure 6.4: Spectral width. Top left: Spectral width (σ, nm) vs. shot number for the 3398 shots in the histogram. Bottom left: Histogram of the FEL spectral width (σ, nm) at 4.02 nm. The most probable value is $1.1 \cdot 10^{-4}$ nm. Right: Single shot of the FEL at 4.02 nm with spectral spread along the horizontal axis (nm).

photon diagnostics (I_0 monitor, PRESTO (Pulse-Resolved Energy Spectrometer (Transparent and Online))) and a gas attenuator (6 m, N_2, 1.7 mbar) to remove the first stage FERMI radiation. The FEL beam was passed through an iris (2 mm) to attenuate both the off-axis second harmonic emission from the FEL light source and the emission of the first undulator chain of FERMI characterized by a larger divergence, and focused by an ellipsoidal mirror ($f = 1.4$ m) onto the graphite sample at normal incidence. The transmitted beam and the collinear second harmonic signal were then passed through a 600 nm Al filter to attenuate the fundamental beam, and into an EUV spectrometer [286]. In the spectrometer, the beam was reflected from a grating (Hitachi cod. 001-0450, 2400 gr/mm central groove density) in first order – to separate the second harmonic signal from the fundamental – and onto a CCD (Princeton Instruments PIXIS-XO 400 B). A single CCD image was recorded for each laser pulse.

To explicitly separate the relative contributions to the measured second harmonic signal from the FEL source and the sample, measurements were also made without the sample present. In general, an approximately equal number of laser shots were recorded with and without the graphite sample present. These off-sample measurements also allowed for the direct characterization of the FEL beam (intensity, mode hopping, etc.).

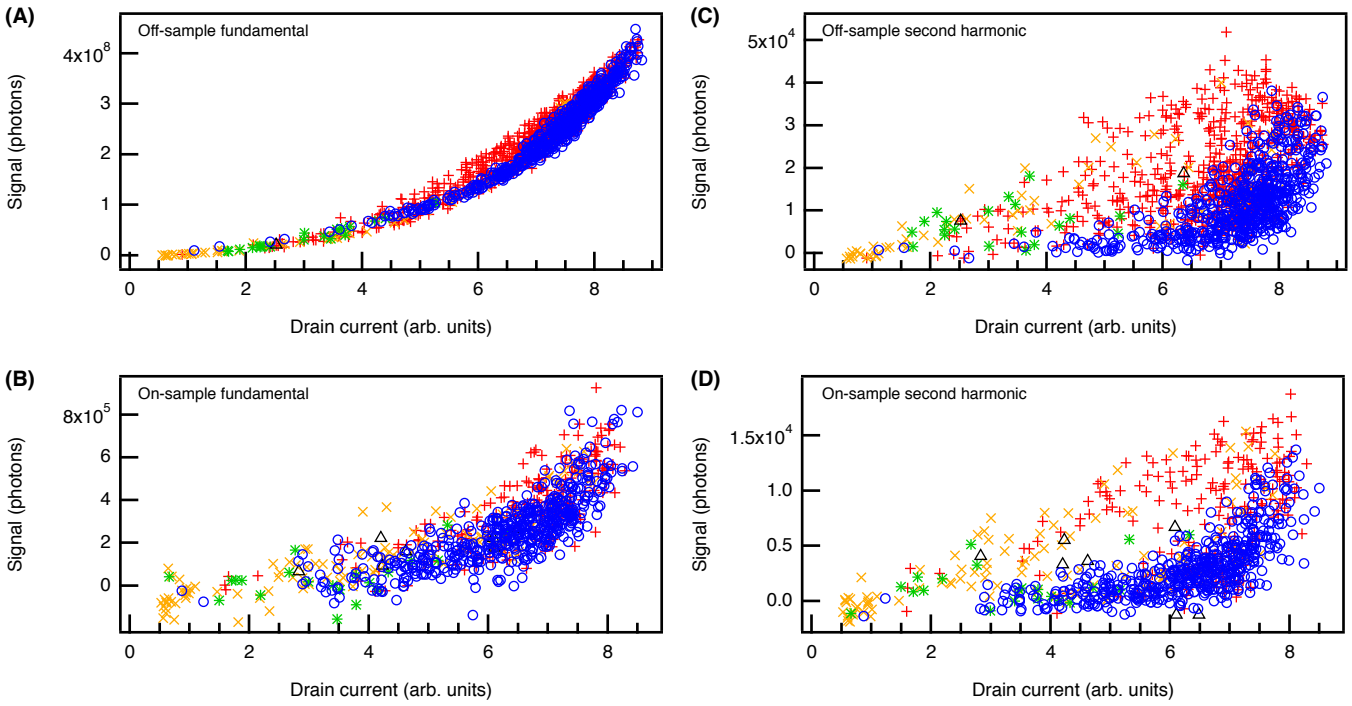

Figure 6.5: Pulse energy calibration and filtering. The correlation between the drain current (arb. units) and spectrometer signal for the off-sample fundamental (a) were used to calibrate the FEL pulse energy. Signals measured on the CCD were filtered using a series of four steps: 1. low energy cutoff (not shown), 2. horizontal (orange X; σ, nm) and vertical (red +; σ, mm) beam profiles, 3. FWHM (green $*$), 4. distance, remaining outliers (black $\triangle$). The points remaining after filtering are shown as blue circles. The uncalibrated dataset presented is from the 500 nm graphite sample at 307.86 eV (4.02 nm). (A) Off-sample fundamental (B) On-sample fundamental (C) Off-sample second harmonic (D) On-sample second harmonic.

Data Analysis

Each dataset for every graphite sample at each photon energy (260.49 eV, 284.18 eV, and 307.86 eV) contained >250 FEL pulses. The signal recorded on the CCD at the fundamental and second harmonic wavelengths is shown in Figure 6.5 for a single data set. Figure 6.5 shows data from the 500 nm graphite sample at 307.86 eV (4.02 nm). Each plotted point represents a single laser shot and its corresponding signal on the CCD, scaling only for the spectrometer efficiency and the transmission through the 600 nm Al filter before the spectrometer, with respect to the uncalibrated drain current measured off the ellipsoidal mirror immediately upstream of the sample. The correlation between the drain current and the CCD signal were used to calibrate the FEL pulse energies. In these data, it is readily apparent that mode stability of the FERMI light source was of particular concern and is especially evident in the signal at the second harmonic wavelengths. This instability may be

caused by two main factors, which may also play a concurrent role. The central wavelength depends on the slope of the beam longitudinal energy distribution. A change in this slope, dependent on the temporal jitter between seed and the electron bunch at the first modulator, may lead to a periodic shift and broadening of the spectrum. A second aspect is related to the FEL tuning condition. Seeking the maximum pulse energy may bring one of the FEL amplifiers to a pre-saturation condition where the pulse duration scaling no longer holds. Under this condition, the pulse may develop side-bands and split into two satellites. The energy extracted increases, but this increase is generally not accompanied by a growth of the peak power.

Filtering and removing contributions from the undesired modes was necessary. This filtering was accomplished in a series of automated steps utilizing the photon diagnostic data from PADReS and the image from the CCD in the spectrometer acquired for each laser pulse. Initially, a low pulse energy cutoff was applied, removing data points originating from FEL pulses for which the measured drain current on the ellipsoidal mirror was less than 0.5 arb. units (not shown in figure). The data were then filtered utilizing the horizontal (energy distribution) and vertical (spatial spread) beam profiles measured by the PADReS spectrometer and the full width half maximum (FWHM) of the peak corresponding to the fundamental beam in the projection of the CCD image along the energy axis. Points were removed from the dataset if the standard deviation (σ) was greater than 0.006 nm or less than 0.58 mm for the horizontal and vertical profiles, respectively. Note that when the FEL enters a regime wherein spectral splitting occurs, a spatial narrowing of the pulse is also observed. For the FWHM filtering, points were removed if they were determined to be outliers with respect to the remaining dataset following the removal of points by the horizontal and vertical profile filtering. Finally, the remaining outliers, determined by a distance filter, were removed. The distance filter was implemented by renormalizing the pulse energy and signal axes (min: 0, max: 1) and calculating the distance between the points and (0.2, 0.75). The distribution of distances was then used in the determination of the outliers. Outliers were determined using a simple box plot model wherein an outlier was defined as those points lying beyond the whiskers – 1.5xIQR (interquartile range) below or above the first and third quartile, respectively. Examples of pulses removed by and remaining after filtering are shown in Figure 6.6.

Following the filtering, the remaining points were binned. As the sampling of pulse energies were not uniform, the bin positions were determined by the centroid of the dataset. The appropriate scaling factors were then applied to account for attenuation through the graphite sample and for the portion of the signal blocked by the entrance slits to the spectrometer. The proportion of the signal blocked by the spectrometer entrance slits was determined using the spatial profile of the fundamental beam on the spectrometer, along with the size of the horizontal and vertical entrance slits. From this, utilizing the shadow cast on the CCD from the slits, the percentage of the flux transmitted through the slits can be calculated, providing a direct measurement of the fundamental beam intensity. The difference between the on- and off-sample curves then yields the power dependence curves shown in Figure 6.2.

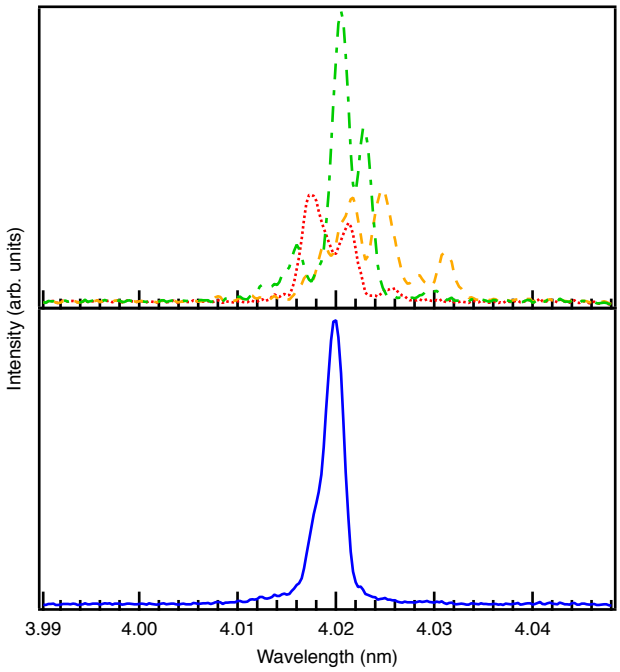

Figure 6.6: Spectral profile of FEL pulses. Typical spectra of pulses removed by filtering (top, dashed lines) vs. pulses remaining after filtering (bottom, blue).

Theoretical Methods

First-principles density functional theory (DFT) [293, 294] simulations were carried out using the `exciting` [288] all-electron full-potential computer package which employs (linearized) augmented planewave + local orbital [(L)APW+lo] methods. In order to investigate second harmonic generation at the (0001) surface of graphite, a supercell comprising of an 8-layer slab of AB stacked hexagonal graphite was set up (see Figure 6.3d). The slab model was generated via a 1x1x4 repetition of a unit cell of AB stacked graphite with the experimentally determined [295] in-plane and out-of-plane lattice parameters: 2.464 Å and 6.711 Å, respectively. A vacuum region of 10 Å was chosen to separate periodic images of the slab along the z direction perpendicular to the slab surface. No additional geometry optimization was carried out as previous DFT calculations [296] of the (0001) surface have indicated insignificant surface relaxation with interlayer separation at the surface very similar to the bulk value. The parameter rgkmax, which represents the product of the minimum muffin-tin radius and maximum length of $\mathbf{G}+\mathbf{k}$ vectors in the basis, was set to 7. The Brillouin zone of the two-dimensional slab was sampled using a 30x30x1 Γ-centered k-point grid. Exchange correlation effects within DFT were modeled at the level of the Perdew-Zunger Local Density Approximation (LDA) [297]. In order to facilitate response calculations near C K-edge frequencies, the *1s* core-orbitals of carbon were explicitly included in the valence self-consistent field treatment so that their Kohn-Sham eigenvalues and eigenvectors are self-consistently updated within the simulation.

To calculate the second-order susceptibility tensor relevant to SHG at the C K-edge, we employed the second-order response formalism from Sharma *et al.* [287], which is implemented within `exciting` [288]. Within this approach, the second-order susceptibility $X^{(2)}(2\omega, \omega, \omega)$ involves contributions arising from excitation energies resonant with ω as well as 2ω (see Equations 49-51 of Sharma *et al.*) [287]. We employ the independent particle approximation, wherein the excitation energy ω_{mn} between electronic states m and n ($m \neq n$) is given by $\omega_{mn} = \varepsilon_m - \varepsilon_n$ where ε_m, ε_n are their respective Kohn-Sham eigenvalues. The linear spectrum was calculated within the same non-interacting formalism to be consistent. Since C *1s* core-electrons are situated ∼280 eV below the Fermi energy, for excitation energies at the C K-edge, ω is roughly 280 eV. Therefore, in order to capture contributions to involving C *1s* excitations resonant near 2ω, we included 2400 empty Kohn-Sham eigenstates whose energies extend up to ∼320 eV above the Fermi energy. However, the electronic density of states (DOS) several hundred eV above the Fermi energy, calculated using finite k-point grids, exhibits a highly oscillatory structure which converges extremely slowly with k-point density. For realistic k-point densities, this in turn leads to very noisy response functions in which the underlying resonance structure is obscured, making the calculation of $X^{(2)}$ at high energies impractical. In reality, the energies of excited states high above the Fermi energy are characterized by significant lifetime broadening. This fact can be utilized to effectively smooth out the density of states and mitigate numerical noise in the response function calculation. Therefore, in the same spirit as the work of Klinkusch *et al.* [298] in the context of photoemission, we added a heuristic energy dependent imaginary part to the unoccupied Kohn-Sham energies to take into account lifetime broadening at high energies. Accordingly, we treat unoccupied Kohn-Sham eigenstates with eigenvalues above the Fermi energy (E_F) as quasiparticle energies and set:

$$\varepsilon_m \rightarrow \varepsilon_m + i\Gamma(\varepsilon_m) \; with \; \Gamma(E) = \frac{1}{\Lambda}\sqrt{E - E_F} \tag{6.3}$$

The imaginary part Γ(E) has a square root dependence on the energy and the λ parameter is related to the inelastic mean free path of electrons [299], which is ∼92 in graphite [300]. This yields a lifetime broadening of ∼0.35 eV for electronic states ∼280 eV above the Fermi energy. Incorporating the modified complex eigen-energies ε_m for the unoccupied states into the excitation frequencies ω_{mn} entering into the calculation of the second-order response functions [287] eliminates numerical noise at high energies and leads to numerical convergence of $X^{(2)}_{zzz}(2\omega, \omega, \omega)$ with k-point sampling density. The broadening in the calculated spectra only assumes lifetime (virtual state: 0.35 eV, core-hole: 0.1 eV) and thermal broadening (0.25 eV). The thermal broadening is based on the average fluctuations in the atomic positions from *ab initio* molecular dynamics simulations of an 8-layer graphite slab. Experimental spectra will be broadened significantly by sample imperfections, atomic motions and experimental conditions.

SHG generally requires inversion symmetry to be broken on the length scale of the incident radiation [68]. As bulk graphite has an inversion center, it should exhibit no second harmonic response. Inversion symmetry is broken at the surface of graphite however, and

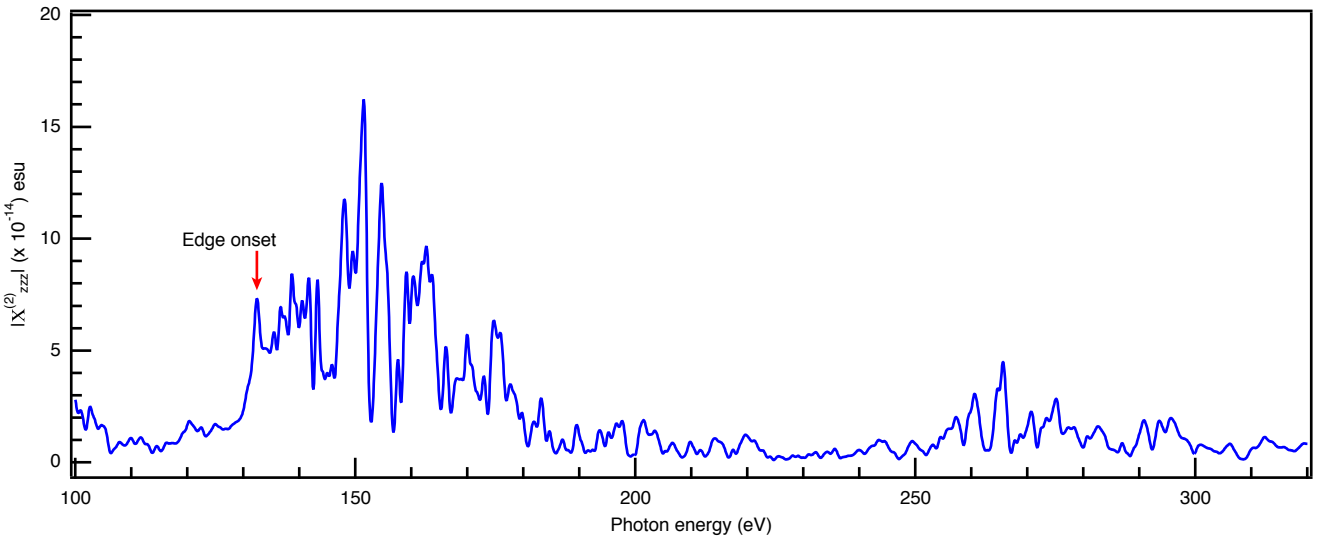

Figure 6.7: Extended Range SH response. Calculated C *1s* contribution to the absolute magnitude $|X^{(2)}_{zzz}(2\omega,\omega,\omega)|$ of the zzz component of the second harmonic susceptibility over an extended energy range. An edge onset is apparent in $|X^{(2)}_{zzz}|$ at ∼132 eV, which corresponds to half the Kohn-Sham C *1s* → conduction band excitation energy in graphite (∼264 eV in the theory). Note that for the theoretical spectra, presented in Figure 6.3, a rigid shift of 20 eV was applied.

we expect some SHG. In the real world experiment, on a sample of finite thickness, light is incident on the top surface of the sample and the bottom surface at the other end of the sample is effectively at infinity. Lack of inversion symmetry at the top surface which responds to the field leads to SHG. On the other hand, in the slab supercell set up considered here, the system effectively responds to a spatially homogeneous electric field that acts at both surfaces of the slab and the system as a whole exhibits inversion symmetry regardless of the number of graphene layers in the slab. The second-order response from one surface cancels that from the other surface leading to overall signal attenuation. Therefore, in order to describe SHG resulting from the loss of inversion symmetry at the top surface, only one of the two surfaces needs to be active in the simulation. This is achieved for the case of core-electron response by only considering the C *1s* electronic states on C atoms in the top four layers of the 8-layer slab explicitly in the valence self-consistent field procedure. For the bottom four layers, the C *1s* electronic states are treated implicitly by including them in the core; these states do not enter the second-order response calculation. In Figure 6.7, we show the C *1s* contribution to the absolute magnitude $|X^{(2)}_{zzz}(2\omega,\omega,\omega)|$ of the zzz component of the second harmonic susceptibility over an extended energy range. At ∼132 eV, which corresponds to half the Kohn-Sham C *1s* → conduction band excitation energy in graphite, an edge onset is apparent in $|X^{(2)}|$. Interestingly, although some signal enhancement is also observed near 270 eV, the magnitude of the SHG response is higher at ω near half the C

K-edge energy than near the edge itself. This suggests that in this instance, the contribution to from the 2ω resonance terms is stronger than the ω resonance terms [287]. Note that in LDA the C *1s* core-state binding energies are underestimated by roughly 20 eV. Therefore, in order to align the energy axis with experiment, a rigid shift of 20 eV is applied to the spectra shown in Figure 6.3. The exponential decay observed in the magnitude of the SHG response with increasing layer depth shown in Figure 6.3C indicates that an 8-layer slab is sufficient to simulate SHG at the graphite surface.

6.2 Two-Photon Absorption of Soft X-Ray Free Electron Laser Radiation by Graphite Near the Carbon K- Absorption Edge

Introduction

The development of ultrafast lasers capable of producing pulses with high energies and peak powers has enabled the general study of matter by nonlinear spectroscopic methods [59, 275]. While this field has heretofore been limited to optical wavelengths, extension to X-ray wavelengths could provide an element- and chemical-specific probe yielding vital new information [60, 61]. However, the lack of high peak power X-ray light sources with requisite spatio-temporal coherence has precluded the study of nonlinear effects at those energies [301]. Very recently, the advent of X-ray free electron lasers (FEL) has extended the field of nonlinear optics [302] to hard X-ray wavelengths and FELs have been used to further the understanding of X-ray induced lasing processes [271], transient gratings [273], and sum frequency generation [63].

Two-photon absorption (TPA), wherein two photons are absorbed simultaneously, is a fundamental third-order nonlinear optical process (shown schematically in the inset of Figure 6.8) [303]. Core-level transitions by two-photon absorption are very sensitive to the energy of the photon relative to the absorption edge, and exhibit increased efficiency under strong radiation fields [304]. This has been studied previously for core-level absorption in zirconium [64], germanium [304], and copper [274] solids as well as neon [305], helium [306], and hydrogen gases [307, 308]. These studies showed that TPA scales as Z^{-6} (where Z is the atomic number), with large increases in cross section as one approaches the absorption edge [309]. Here we demonstrate that soft X-ray two-photon absorption in carbon behaves as predicted by extrapolation from recent studies performed at hard X-ray energies.

Methods

A. Experimental Design

Soft X-ray transmission experiments were performed at EIS-TIMEX at the FERMI free electron laser in Trieste [279, 280, 284, 285].The FEL beam was propagated along the Photon Analysis, Delivery, and Reduction System (PADReS), which includes shot-to-shot photon diagnostics (I_0 monitor, PRESTO (Pulse-Resolved Energy Spectrometer (Transparent and Online))) and a gas attenuator (6 m, N_2, 1.7 mbar) to remove the seed laser radiation [292]. The pulses were then passed through a 2 mm iris to attenuate off-axis emission and focused by an ellipsoidal mirror to a spot size of $\sim$350 μm^2. The drain current from the ellipsoidal mirror served as an additional I_0 monitor. Photon energies of 260.49 eV, 284.18 eV, and 307.86 eV with a pulse duration $\sim$25 fs were used. At the laser focus, samples could be inserted (called 'sample' herein) or removed (called 'no sample' herein). Unsupported

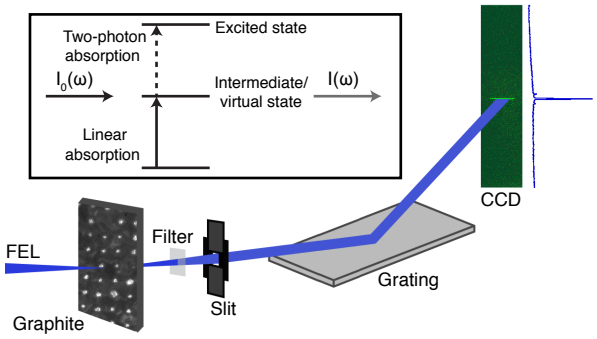

Figure 6.8: Experimental schematic. X-ray pulses from the FEL are focused and either intercepted by a sample or allowed to transmit, before being dispersed by a grating and imaged by a camera. This design permits a direct determination of the attenuation. Inset: Schematic of the dominant processes observed in this work, two-photon absorption. While linear (one-photon) absorption is always present, the rate of two-photon absorption is particularly sensitive to the absorption edge and the nature of the excited state. $I_0(\omega)$ and $I(\omega)$ represent the intensity of the input (I_{NS}) and transmitted beams I_S/I_{NS}, respectively.

nanocrystalline graphite films (thickness: 100, 300, 500 nm) mounted onto L1.0 rings (10 mm diameter) from Lebow company (Goleta, CA) were used as targets. The films were rastered between each laser shot to ensure that a pristine sample was probed. The transmitted beam was propagated through a 600 nm Al filter to prevent camera saturation, onto a grating in first order (Hitachi cod. 001-0450, 2400 gr/mm central groove density), and finally onto a Princeton Instruments PIXIS-XO 400 B CCD camera [286]. A single image was recorded for each pulse. The experimental design is shown schematically in Figure 6.8.

B. Data Analysis

Each dataset comprises hundreds of FEL pulses. The number of photons detected is calculated from the signal measured on the CCD, scaling for the transmission through the 600 nm Al filter and the spectrometer efficiency (entrance slits, grating, detector) [310]. The number of input photons is determined from the drain current measured from the ellipsoidal mirror immediately upstream of the sample. The points were binned and the ratio of the number of photons detected with and without samples is plotted against the X-ray intensity (photons/(cm^{2}s)).

The ratio of photons transmitted with a sample (S) and with no sample (NS) for a single photon event is given as

$$\frac{I_s}{I_{NS}} = e^{-\alpha c x} \tag{6.4}$$

where I_S is the signal intensity with a sample and I_{NS} is the signal intensity with no sample, α is the absorption coefficient, c is the density of the material, and x is the thickness. As the thickness of each sample is constant, the absorption ($A = \alpha c x$) should be constant for a

given sample. For two-photon events the ratio is given as

$$\frac{I_s}{I_{NS}} = \frac{1}{1 + \beta c x I_{NS}} \tag{6.5}$$

where β is the two-photon absorption coefficient. As β is constant for a given energy and the density and thickness do not change for a given sample, βcx will be constant for a given sample. Thus, when both one-photon and two-photon absorption occur, the total ratio should be

$$\frac{I_s}{I_{NS}} = \frac{a}{1 + bI_{NS}} \tag{6.6}$$

where $a = e^{-\alpha cx}$ (linear absorption) and $b = \beta cx$ (two-photon absorption) [303]. The two-photon absorption cross section was determined by following the literature procedure [274, 304].

Note that the two-photon absorption data are significantly less sensitive to the quality of the laser pulse than are other nonlinear processes (e.g., second harmonic generation), and so this effect can be seen without filtering based on lasing mode.

Results and Discussion

The ratio of photons transmitted with and without samples present at 260.49 eV, 284.18 eV, and 307.86 eV as a function of intensity are shown in Figure 6.9A, B, and C respectively. The sample thicknesses shown are 100 nm (green circle), 300 nm (blue diamond) and 500 nm (red square). The average value of the attenuation is shown as a dashed line, and a curve fit to Equation 6.6 is shown as a solid line. Aside from the expected higher attenuation, no significant effects are observed as a function of increasing sample thickness.

Transmission is sensitive to nonlinear processes both above and below the K-edge resonance. In both Figure 6.9A and 6.9C, the attenuation is roughly constant as a function of X-ray intensity. This implies that there are no significant nonlinear absorption effects at these energies (260.49 eV and 307.86 eV), suggesting that, at the power densities employed here, the current generation of soft X-ray FELs can be used off-resonance near the carbon K-edge as a probe of linear processes without concern for nonlinear processes affecting absorption cross sections.

The effects of two-photon absorption are observed, however, when the laser is on-resonance, just below the K-edge at 284.18 eV, as shown in Figure 6.9B. The shape of the curves matches well with that predicted for two-photon absorption (Equation 6.6) at both 300 nm and 500 nm sample thicknesses. The nonresonant two-photon absorption cross section as previously derived [304] would be

$$\sigma_{TPA}(Z) = 1.27 \cdot 10^{-50} Z^{-6} \text{ (cm}^4\text{s)} \tag{6.7}$$

where Z is the atomic number ($Z_{carbon} = 6$). The calculated value of $2.72 \cdot 10^{-55}$ cm^{4}s, as predicted by a simple Z^{-6} scaling, is 3 orders of magnitude smaller than the experimental

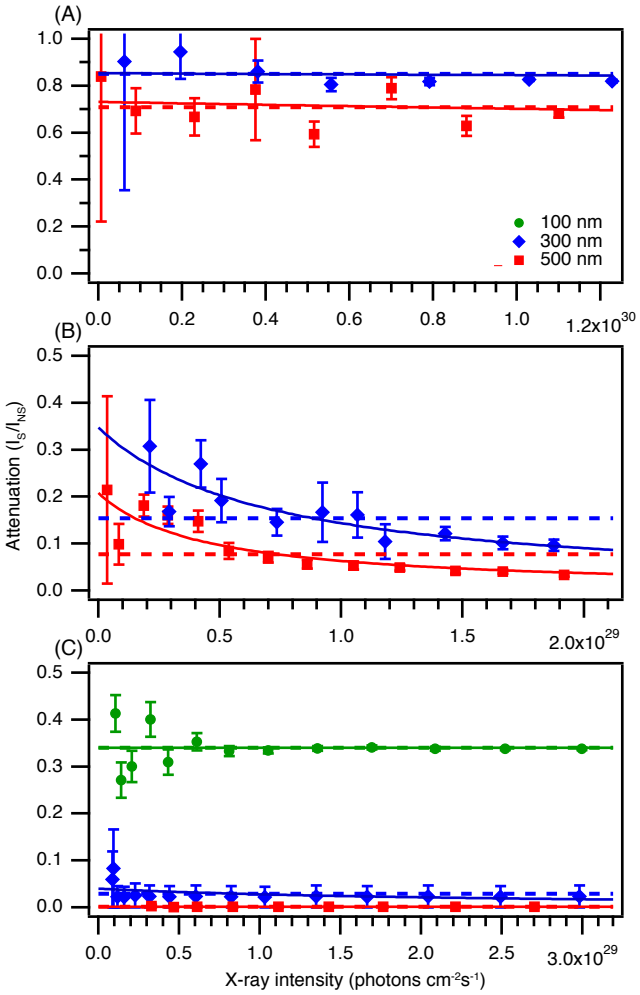

Figure 6.9: Plot of the attenuation versus X-ray beam intensity at (A) 260.49 eV, (B) 284.18 eV and (C) 307.86 eV. Different sample thicknesses are shown: 100 nm (green circle), 300 nm (blue diamond) and 500 nm (red square). Average values are shown as dashed lines, while the two-photon absorption fit discussed in the text is shown as a solid line. Only at 284.18 eV is a large difference seen between the average value and the fitted curve. This is due to two-photon absorption.

value found here ($\sim 3 \cdot 10^{-52}$ cm^{4}s). However, due to resonance effects, a more accurate cross section prediction would be

$$\sigma_{TPA}(Z, E_i) = 4 \cdot 10^{-52} Z^{-4} \frac{E_i}{E_i - E_1} \text{ (cm}^4\text{s)} \tag{6.8}$$

where E_1 is the binding energy – in this case 284.8 eV [311] – and E_i is the input photon energy [274]. This is due to the photon energy being very close to the absorption edge, as has been investigated in some detail for hard X-ray photons [274]. The predicted cross section at this energy, $1.4 \cdot 10^{-52}$ cm^{4}s, agrees well with our experimental values ($\sim 3 \cdot 10^{-52}$ cm^{4}s). The ratio of the linear to two-photon cross section is also similar to what is found in both the optical and the hard X-ray regimes [274]. The two-photon absorption cross section at 260.49 eV and 307.86 eV cannot be determined from these measurements due to low signal-to-noise ratios, but it is at least two orders of magnitude lower than what is observed at 284.18 eV.

Note that as we are monitoring transmission, the measurement is sensitive to a variety of nonlinear processes and can be used above the absorption edge. At energies well above the edge, X-ray induced transparency is another possible phenomenon [312]. This would manifest as an decrease in attenuation at high intensity in Figure 6.9C, but is not observed here.

Conclusions

Transmission measurements of soft X-ray free electron laser pulses were made near the carbon K-edge. At energies 25 eV above or below the K-edge, the FEL behaves largely as a linear absorption probe. Near the edge, significant two-photon absorption is observed, and is several orders of magnitude larger than would be predicted if not at resonance. The observed two-photon cross section ($\sim 3 \cdot 10^{-52}$ cm^{4}s) shows good agreement with the value predicted from previous work at hard X-ray energies.

Bibliography

1. Duffin, A. M. & Saykally, R. J. Electrokinetic Hydrogen Generation from Liquid Water Microjets. *J. Phys. Chem. C* **111,** 12031–12037 (2007).
2. Duffin, A. M. & Saykally, R. J. Electrokinetic Power Generation from Liquid Water Microjets. *J. Phys. Chem. C* **112,** 17018–17022 (2008).
3. Faubel, M. & Steiner, B. Strong Bipolar Electrokinetic Charging of Thin Liquid Jets Emerging from 10 μm PtIr Nozzles. *Ber. Bunsenges. Phys. Chem.* **96,** 1167–1172 (1992).
4. Holstein, W. L., Hayes, L. J., Robinson, E. M. C., Laurence, G. S. & Buntine, M. A. Aspects of Electrokinetic Charging in Liquid Microjets. *J. Phys. Chem. B* **103,** 3035–3042 (1999).
5. Groves, J. N. & Sears, A. R. Alternating Streaming Current Measurements. *J. Colloid Interface Sci.* **53,** 83–89 (1975).
6. Hummer, G., Rasaiah, J. C. & Noworyta, J. P. Water Conduction Through the Hydrophobic Channel of a Carbon Nanotube. *Nature* **414,** 188–190 (2001).
7. Yang, J., Lu, F. Z., Kostiuk, L. W. & Kwok, D. Y. Electrokinetic Microchannel Battery by Means of Electrokinetic and Microfluidic Phenomena. *J. Micromech. Microeng.* **13,** 963–970 (2003).
8. Siria, A. *et al.* Giant Osmotic Energy Conversion Measured in a Single Transmembrane Boron Nitride Nanotube. *Nature* **494,** 455–458 (2013).
9. Chang, C. C. & Yang, R. J. Electrokinetic Energy Conversion Efficiency in Ion-Selective Nanopores. *Appl. Phys. Lett.* **99,** 083102 (2011).
10. Van der Heyden, F. H. J., Bonthuis, D. J., Stein, D., Meyer, C. & Dekker, C. Power Generation by Pressure-Driven Transport of Ions in Nanofluidic Channels. *Nano Lett.* **7,** 1022–1025 (2007).
11. Van der Heyden, F. H. J., Bonthuis, D. J., Stein, D., Meyer, C. & Dekker, C. Electrokinetic Energy Conversion Efficiency in Nanofluidic Channels. *Nano Lett.* **6,** 2232–2237 (2006).

12. Delgado, A. V., González-Caballero, F., Hunter, R. J., Koopal, L. K. & Lyklema, J. Measurement and Interpretation of Electrokinetic Phenomena (IUPAC Technical Report). *Pure Appl. Chem.* **77,** 1753–1805 (2005).

13. Canning, J., Buckley, E., Huntington, S. & Lyytikäinen, K. Using Multi-Microchannel Capillaries for Determination of the Zeta Potential of a Microfluidic Channel. *Electrochim. Acta* **49,** 3581–3586 (2004).

14. Canning, J., Buckley, E. & Lyytikainen, K. Electrokinetic Air-Silica Structured Multi-Microchannel Capillary Batteries. *Electron. Lett.* **40,** 298–299 (2004).

15. Yang, J., Lu, F., Kostiuk, L. W. & Kwok, D. Y. Electrokinetic Microchannel Battery by Means of Electrokinetic and Microfluidic Phenomena. *J. Micromech. Microeng.* **13,** 963–970 (2003).

16. Werner, C., Körber, H., Zimmermann, R., Dukhin, S. & Jacobasch, H. J. Extended Electrokinetic Characterization of Flat Solid Surfaces. *J. Colloid Interface Sci.* **208,** 329–346 (1998).

17. Davidson, C. & Xuan, X. Effects of Stern Layer Conductance on Electrokinetic Energy Conversion in Nanofluidic Channels. *Electrophoresis* **29,** 1125–1130 (2008).

18. Werner, C., Zimmermann, R. & Kratzmüller, T. Streaming Potential and Streaming Current Measurements at Planar Solid/Liquid Interfaces for Simultaneous Determination of Zeta Potential and Surface Conductivity. *Colloids Surf. A Physicochem. Eng. Asp.* **192,** 205–213 (2001).

19. Lam, R. K., Gamlieli, Z., Harris, S. J. & Saykally, R. J. Thermally driven electrokinetic energy conversion with liquid water microjets. *Chem. Phys. Lett.* **640,** 172–174 (2015).

20. Schwierz, N. *et al.* Hydrogen and Electric Power Generation from Liquid Microjets: Design Principles for Optimizing Conversion Efficiency. *J. Phys. Chem. C* **120,** 14513–14521 (2016).

21. Faubel, M., Steiner, B. & Toennies, J. P. Measurement of He I Photoelectron Spectra of Liquid Water, Formamide and Ethylene Glycol in Fast-Flowing Microjets. *J. Electron. Spectrosc. Relat. Phenom.* **95,** 159–169 (1998).

22. Horio, T., Shen, H., Adachi, S. & Suzuki, T. Photoelectron Spectra of Solvated Electrons in Bulk Water, Methanol, and Ethanol. *Chem. Phys. Lett.* **535,** 12–16 (2012).

23. Shreve, A. T., Elkins, M. H. & Neumark, D. M. Photoelectron Spectroscopy of Solvated Electrons in Alcohol and Acetonitrile Microjets. *Chem. Sci.* **4,** 1633–1639 (4 2013).

24. Faubel, M., Schlemmer, S. & Toennies, J. P. A molecular beam study of the evaporation of water from a liquid jet. *Z. Phys. D: Atoms, Mol. Clust.* **10,** 269–277 (1988).

25. Faubel, M., Steiner, B. & Toennies, J. P. Photoelectron spectroscopy of liquid water, some alcohols, and pure nonane in free micro jets. *J. Chem. Phys.* **106,** 9013 (1997).

26. Wilson, K. R., Tobin, J. G., Ankudinov, A. L., Rehr, J. J. & Saykally, R. J. Extended X-Ray absorption fine structure from hydrogen atoms in water. *Phys. Rev. Lett.* **85,** 4289–92 (2000).
27. Wilson, K. R. *et al.* X-ray Spectroscopy of Liquid Water Microjets. *J. Phys. Chem. B* **105,** 3346–3349 (2001).
28. Shih, O. *et al.* Cation-cation contact pairing in water: guanidinium. *J. Chem. Phys.* **139,** 035104 (2013).
29. Smith, J. W. *et al.* Properties of aqueous nitrate and nitrite from x-ray absorption spectroscopy. *J. Chem. Phys.* **143,** 084503 (2015).
30. Smith, J. W. *et al.* X-Ray absorption spectroscopy of $LiBF_4$ in propylene carbonate: a model lithium ion battery electrolyte. *Phys. Chem. Chem. Phys.* **16,** 23568–23575 (2014).
31. Lam, R. K. *et al.* Electrokinetic detection for X-ray spectra of weakly interacting liquids: n-decane and n-nonane. *J. Chem. Phys.* **140,** 234202 (2014).
32. Lam, R. K., Smith, J. W. & Saykally, R. J. Communication: Hydrogen bonding interactions in water-alcohol mixtures from X-ray absorption spectroscopy. *J. Chem. Phys.* **144,** 191103 (2016).
33. Lam, R. K. *et al.* The hydration structure of aqueous carbonic acid from X-ray absorption spectroscopy. *Chem. Phys. Lett.* **614,** 282–286 (2014).
34. Lam, R. K. *et al.* The hydration structure of dissolved carbon dioxide from X-ray absorption spectroscopy. *Chem. Phys. Lett.* **633,** 214–217 (2015).
35. Lam, R. K. *et al.* Reversed interfacial fractionation of carbonate and bicarbonate evidenced by X-ray photoemission spectroscopy. *J. Chem. Phys.* **146,** 094703 (2017).
36. Butler, J. A. V., Thomson, D. W. & Maclennan, W. H. 173. The free energy of the normal aliphatic alcohols in aqueous solution. Part I. The partial vapour pressures of aqueous solutions of methyl, n-propyl, and n-butyl alcohols. Part II. The solubilities of some normal aliphatic alcohols in water. Part III. *J. Chem. Soc.* 674–686 (1933).
37. Frank, H. S. & Evans, M. W. Free Volume and Entropy in Condensed Systems. *J. Chem. Phys.* **13,** 507–532 (1945).
38. Laaksonen, A., Kusalik, P. G. & Svishchev, I. M. Three-Dimensional Structure in Water–Methanol Mixtures. *J. Phys. Chem. A* **5639,** 5910–5918 (1997).
39. Van Erp, T. S. & Meijer, E. J. Ab initio molecular dynamics study of aqueous solvation of ethanol and ethylene. *J. Chem. Phys.* **118,** 8831 (2003).
40. Tanaka, H. & Gubbins, K. E. Structure and thermodynamic properties of water–methanol mixtures: Role of the water–water interaction. *J. Chem. Phys.* **97,** 2626 (1992).

41. England, A. H. *et al.* On the hydration and hydrolysis of carbon dioxide. *Chem. Phys. Lett.* **514,** 187–195 (2011).

42. Adamczyk, K., Premont-Schwarz, M., Pines, D., Pines, E. & Nibbering, E. T. J. Real-Time Observation of Carbonic Acid Formation in Aqueous Solution. *Science* **326,** 1690–1694 (2009).

43. Eigen, M. Proton Transfer, Acid-Base Catalysis, and Enzymatic Hydrolysis. Part I: ELEMENTARY PROCESSES. *Angew. Chem. Int. Ed. Engl.* **3,** 1–19 (1964).

44. Putnis, A. Why Mineral Interfaces Matter. *Science* **343,** 1441–1442 (2014).

45. Al-Hosney, H. A. & Grassian, V. H. Carbonic Acid: An Important Intermediate in the Surface Chemistry of Calcium Carbonate. *J. Am. Chem. Soc.* **126,** 8068–8069 (2004).

46. Ridgwell, A. & Zeebe, R. E. The role of the global carbonate cycle in the regulation and evolution of the Earth system. *Earth Planet. Sci. Lett.* **234,** 299–315 (2005).

47. Silverman, D. N. & McKenna, R. Solvent-Mediated Proton Transfer in Catalysis by Carbonic Anhydrase. *Acc. Chem. Res.* **40,** 669–675 (2007).

48. Kurtz, I., Kraut, J., Ornekian, V. & Nguyen, M. K. Acid-base analysis: a critique of the Stewart and bicarbonate-centered approaches. *Am. J. Physiol. - Ren. Physiol.* **294,** F1009–F1031 (2008).

49. Silverman, D. N. & Lindskog, S. The catalytic mechanism of carbonic anhydrase: implications of a rate-limiting protolysis of water. *Acc. Chem. Res.* **21,** 30–36 (1988).

50. Falcke, H. & Eberle, S. H. Raman spectroscopic identification of carbonic acid. *Water Res.* **24,** 685–688 (1990).

51. Wang, X., Conway, W., Burns, R., McCann, N. & Maeder, M. Comprehensive Study of the Hydration and Dehydration Reactions of Carbon Dioxide in Aqueous Solution. *J. Phys. Chem. A* **114,** 1734–1740 (2010).

52. Johnson, C. M., Tyrode, E., Baldelli, S., Rutland, M. W. & Leygraf, C. A Vibrational Sum Frequency Spectroscopy Study of the Liquid-Gas Interface of Acetic Acid-Water Mixtures: 1. Surface Speciation. *J. Phys. Chem. B* **109,** 321–328 (2005).

53. Vaikuntanathan, S., Shaffer, P. R. & Geissler, P. L. Adsorption of solutes at liquid-vapor interfaces: insights from lattice gas models. *Faraday Discuss.* **160,** 63–74 (2013).

54. Otten, D. E., Shaffer, P. R., Geissler, P. L. & Saykally, R. J. Elucidating the mechanism of selective ion adsorption to the liquid water surface. *Proc. Natl. Acad. Sci. U. S. A.* **109,** 701–705 (2012).

55. Noah-Vanhoucke, J. & Geissler, P. L. On the fluctuations that drive small ions toward, and away from, interfaces between polar liquids and their vapors. *Proc. Natl. Acad. Sci. U. S. A.* **106,** 15125–15130 (2009).

56. Tarbuck, T. L. & Richmond, G. L. Adsorption and Reaction of CO_2 and SO_2 at a Water Surface. *J. Am. Chem. Soc.* **128,** 3256–3267 (2006).

57. Du, H., Liu, J., Ozdemir, O., Nguyen, A. V. & Miller, J. D. Molecular features of the air/carbonate solution interface. *J. Colloid Interface Sci.* **318,** 271–277 (2008).

58. Hua, W., Chen, X. & Allen, H. C. Phase-Sensitive Sum Frequency Revealing Accommodation of Bicarbonate Ions, and Charge Separation of Sodium and Carbonate Ions within the Air/Water Interface. *J. Phys. Chem. A* **115,** 6233–6238 (2011).

59. Shen, Y. R. *The Principles of Nonlinear Optics* (Wiley, New York, 1984).

60. Stöhr, J. *NEXAFS Spectroscopy* (Springer Berlin Heidelberg, Berlin, Heidelberg, 1992).

61. Mukamel, S. *Principles of nonlinear optical spectroscopy* eng, 543 (Oxford Univ. Press, New York, 2009).

62. Shwartz, S. *et al.* X-Ray Second Harmonic Generation. *Phys. Rev. Lett.* **112,** 163901 (2014).

63. Glover, T. E. *et al.* X-ray and optical wave mixing. *Nature* **488,** 603–608 (2012).

64. Tamasaku, K. *et al.* X-ray two-photon absorption competing against single and sequential multiphoton processes. *Nat. Photonics* **8,** 313–316 (2014).

65. Fuchs, M. *et al.* Anomalous nonlinear X-ray Compton scattering. *Nat. Phys.* **11,** 964–970 (2015).

66. Vartanyants, I. A. *et al.* Coherence Properties of Individual Femtosecond Pulses of an X-Ray Free-Electron Laser. *Phys. Rev. Lett* **107,** 144801 (2011).

67. Yu, L.-H. *et al.* High-Gain Harmonic-Generation Free-Electron Laser. *Science* **289,** 932 LP –934 (2000).

68. Nazarkin, A., Podorov, S., Uschmann, I., Förster, E. & Sauerbrey, R. Nonlinear optics in the angstrom regime: Hard-x-ray frequency doubling in perfect crystals. *Phys. Rev. A* **67,** 41804 (2003).

69. Miao, J., Ercius, P. & Billinge, S. J. L. Atomic electron tomography: 3D structures without crystals. *Science* **353,** aaf2157 (2016).

70. *Water Energy Nexus: Challenges and Opportunities* tech. rep. (2014).

71. Lyklema, J. Surface conduction. *J. Phys. Condens. Matter* **13,** 5027 (2001).

72. Miljkovic, N., Preston, D. J., Enright, R. & Wang, E. N. Electrostatic charging of jumping droplets. *Nat. Commun.* **4** (2013).

73. Miljkovic, N., Preston, D. J., Enright, R. & Wang, E. N. Jumping-droplet electrostatic energy harvesting. *Appl. Phys. Lett.* **105,** 013111 (2014).

74. Saykally, R. J., Duffin, A. M., Wilson, K. R. & Rude, B. S. *Method and apparatus for electrokinetic co-generation of hydrogen and electric power from liquid water microjets* 2013.

75. Xie, Y. *et al.* High-Efficiency Ballistic Electrostatic Generator using Microdroplets. *Nat. Commun.* **5** (2014).

76. Kelly, D. N., Lam, R. K., Duffin, A. M. & Saykally, R. J. Exploring Solid/Aqueous Interfaces with Ultradilute Electrokinetic Analysis of Liquid Microjets. *J. Phys. Chem. C* **117,** 12702–12706 (2013).

77. Huang, D. M., Cottin-Bizonne, C., Ybert, C. & Bocquet, L. Ion-Specific Anomalous Electrokinetic Effects in Hydrophobic Nanochannels. *Phys. Rev. Lett.* **98,** 177801 (17 2007).

78. White, F. M. in. 4th (McGraw-Hill, Boston, 1999).

79. Davies, J. T. & Rideal, E. K. in. 2nd (Academic Press, New York, 1961).

80. Rouse, H. & Howe, J. W. in. 2nd (John Wiley & Sons, Inc., London, 1953).

81. Evans, D. F. & Wennerström, H. in. 2nd (Wiley-VCH, New York, 1999).

82. Bocquet, L. & Charlaix, E. Nanofluidics, from Bulk to Interfaces. *Chem. Soc. Rev.* **39,** 1073–1095 (2010).

83. Bocquet, L. & Barrat, J. L. Flow Boundary Conditions from Nano- to Micro-Scales. *Soft Matter* **3,** 685–693 (6 2007).

84. Huang, D. M., Sendner, C., Horinek, D., Netz, R. R. & Bocquet, L. Water Slippage versus Contact Angle: A Quasiuniversal Relationship. *Phys. Rev. Lett.* **101,** 226101 (2008).

85. Sendner, C., Horinek, D., Bocquet, L. & Netz, R. R. Interfacial Water at Hydrophobic and Hydrophilic Surfaces: Slip, Viscosity, and Diffusion. *Langmuir* **25,** 10768–10781 (2009).

86. Bonthuis, D. J. & Netz, R. R. Unraveling the Combined Effects of Dielectric and Viscosity Profiles on Surface Capacitance, Electro-Osmotic Mobility, and Electric Surface Conductivity. *Langmuir* **28,** 16049–16059 (2012).

87. Bonthuis, D. J. *et al.* Theory and Simulations of Water Flow through Carbon Nanotubes: Prospects and Pitfalls. *J. Phys. Condens. Matter* **23,** 184110 (2011).

88. Majumder, M., Chopra, N., Andrews, R. & Hinds, B. J. Nanoscale Hydrodynamics: Enhanced Flow in Carbon Nanotubes. *Nature* **438,** 44 (2005).

89. Luo, G. *et al.* Ion Distributions Near a Liquid-Liquid Interface. *Science* **311,** 216–218 (2006).

90. Boström, M. *et al.* Why Forces Between Proteins Follow Different Hofmeister Series for pH Above and Below Pi. *Biophys. Chem.* **117,** 217–224 (2005).

91. Schwierz, N. & Netz, R. R. Effective Interaction between Two Ion-Adsorbing Plates: Hofmeister Series and Salting-In/Salting-Out Phase Diagrams from a Global Mean-Field Analysis. *Langmuir* **28,** 3881–3886 (2012).

92. Schwierz, N., Horinek, D., Sivan, U. & Netz, R. R. Reversed Hofmeister Series - the Rule rather than the Exception. *Curr. Opin. Colloid Interface Sci.* **23,** 10–18 (2016).

93. Schwierz, N., Horinek, D. & Netz, R. R. Anionic and Cationic Hofmeister Effects on Hydrophobic and Hydrophilic Surfaces. *Langmuir* **29,** 2602–2614 (2013).

94. Borukhov, I., Andelman, D. & Orland, H. Polyelectrolyte Solutions between Charged Surfaces. *Europhys. Lett.* **32,** 499–504 (1995).

95. Borukhov, I., Andelman, D. & Orland, H. Steric Effects in Electrolytes: A Modified Poisson-Boltzmann Equation. *Phys. Rev. Lett.* **79,** 435–438 (3 1997).

96. Pegram, L. M. & Record, M. T. Partitioning of Atmospherically Relevant Ions Between Bulk Water and the Water/Vapor Interface. *Proc. Natl. Acad. Sci. U. S. A.* **103,** 14278–14281 (2006).

97. Schwierz, N., Horinek, D. & Netz, R. R. Reversed Anionic Hofmeister Series: The Interplay of Surface Charge and Surface Polarity. *Langmuir* **26,** 7370–7379 (2010).

98. Saykally, R. J. Air/Water Interface: Two Sides of the Acid-Base Story. *Nat. Chem.* **5,** 82–84 (2013).

99. Pegram, L. M. & Record Jr., M. T. Quantifying Accumulation or Exclusion of H^+, HO^-, and Hofmeister Salt Ions Near Interfaces. *Chem. Phys. Lett.* **467,** 1–8 (2008).

100. Mucha, M. *et al.* Unified Molecular Picture of the Surfaces of Aqueous Acid, Base, and Salt Solutions. *J. Phys. Chem. B* **109,** 7617–7623 (2005).

101. Buch, V., Milet, A., Vcha, R., Jungwirth, P. & Devlin, J. P. Water Surface is Acidic. *Proc. Natl. Acad. Sci.* **104,** 7342–7347 (2007).

102. Tse, Y. L. S., Chen, C., Lindberg, G. E., Kumar, R. & Voth, G. A. Propensity of Hydrated Excess Protons and Hydroxide Anions for the Air-Water Interface. *J. Am. Chem. Soc.* **137,** 12610–12616 (2015).

103. Petersen, P. B. & Saykally, R. J. Is the Liquid Water Surface Basic or Acidic? Macroscopic vs. Molecular-scale Investigations. *Chem. Phys. Lett.* **458,** 255–261 (2008).

104. Yamaguchi, S., Kundu, A., Sen, P. & Tahara, T. Communication: Quantitative Estimate of the Water Surface pH using Heterodyne-detected Electronic Sum Frequency Generation. *J. Chem. Phys.* **137,** 151101 (2012).

105. Winter, B., Faubel, M., Vcha, R. & Jungwirth, P. Behavior of Hydroxide at the Water/Vapor Interface. *Chem. Phys. Lett.* **474,** 241–247 (2009).

106. Takahashi, M. ζ Potential of Microbubbles in Aqueous Solutions: Electrical Properties of the Gas-Water Interface. *J. Phys. Chem. B* **109,** 21858–21864 (2005).

107. Beattie, J. K., Djerdjev, A. M. & Warr, G. G. The Surface of Neat Water is Basic. *Faraday Discuss.* **141,** 31–39 (0 2009).

108. Mishra, H. *et al.* Brønsted Basicity of the Air-Water Interface. *Proc. Natl. Acad. Sci. U. S. A.* **109,** 18679–18683 (2012).

109. Baer, M. D., Kuo, I. F. W., Tobias, D. J. & Mundy, C. J. Toward a Unified Picture of the Water Self-Ions at the Air-Water Interface: A Density Functional Theory Perspective. *J. Phys. Chem. B* **118,** 8364–8372 (2014).

110. Behrens, S. H. & Grier, D. G. The Charge of Glass and Silica Surfaces. *J. Chem. Phys.* **115,** 6716–6721 (2001).

111. Schwierz, N., Horinek, D. & Netz, R. R. Specific Ion Binding to Carboxylic Surface Groups and the pH Dependence of the Hofmeister Series. *Langmuir* **31,** 215–225 (2015).

112. De Gennes, P. G. On Fluid/Wall Slippage. *Langmuir* **18,** 3413–3414 (2002).

113. Golnak, R. *et al.* Local electronic structure of aqueous zinc acetate: oxygen K-edge X-ray absorption and emission spectroscopy on micro-jets. *Phys. Chem. Chem. Phys.* **15,** 8046–8049 (2013).

114. Lange, K. M. & Aziz, E. F. Electronic structure of ions and molecules in solution: a view from modern soft X-ray spectroscopies. *Chem. Soc. Rev.* **42,** 6840–6859 (2013).

115. Weinhardt, L. *et al.* Resonant X-ray emission spectroscopy of liquid water: Novel instrumentation, high resolution, and the "map" approach. *J. Electron Spectrosc. Relat. Phenom.* **177,** 206–211 (2010).

116. Lange, K. M. *et al.* High resolution X-ray emission spectroscopy of water and aqueous ions using the micro-jet technique. *Chem. Phys.* **377,** 1–5 (2010).

117. Wilson, K. R. *et al.* Investigation of volatile liquid surfaces by synchrotron x-ray spectroscopy of liquid microjets. *Rev. Sci. Instrum.* **75,** 725–736 (2004).

118. Kelly, D. N. *et al.* Communication: Near edge x-ray absorption fine structure spectroscopy of aqueous adenosine triphosphate at the carbon and nitrogen K-edges. *J. Chem. Phys.* **133,** 101103 (2010).

119. Cappa, C. D., Smith, J. D., Messer, B. M., Cohen, R. C. & Saykally, R. J. Effects of cations on the hydrogen bond network of liquid water: new results from X-ray absorption spectroscopy of liquid microjets. *J. Phys. Chem.. B* **110,** 5301–9 (2006).

120. Winter, B. & Faubel, M. Photoemission from Liquid Aqueous Solutions. *Chem. Rev.* **106,** 1176–1211 (2006).

121. Brown, M. A. *et al.* Electronic Structures of Formic Acid (HCOOH) and Formate ($HCOO^-$) in Aqueous Solutions. *J. Phys. Chem. Letters* **3,** 1754–1759 (2012).

122. Wilson, K. R. *et al.* Characterization of hydrogen bond acceptor molecules at the water surface using near-edge x-ray absorption fine-structure spectroscopy and density functional theory. *J. Phys. Condens. Matter* **14,** L221–L226 (2002).

123. Cappa, C. D., Smith, J. D., Wilson, K. R. & Saykally, R. J. Revisiting the total ion yield x-ray absorption spectra of liquid water microjets. *J. Phys. Condens. Matter* **20,** 205105 (2008).

124. Cappa, C. D., Smith, J. D., Messer, B. M., Cohen, R. C. & Saykally, R. J. The electronic structure of the hydrated proton: a comparative X-ray absorption study of aqueous HCl and NaCl solutions. *J. Phys. Chem.. B* **110,** 1166–71 (2006).

125. Aziz, E. F. *et al.* Cation-Specific Interactions with Carboxylate in Amino Acid and Acetate Aqueous Solutions: X-ray Absorption and ab initio Calculations. *J. Phys. Chem. B* **112,** 12567–12570 (2008).

126. Aziz, E. F., Freiwald, M., Eisebitt, S. & Eberhardt, W. Steric hindrance of ion-ion interaction in electrolytes. *Phys. Rev. B* **73,** 75120 (2006).

127. Lange, K. M., Kothe, A. & Aziz, E. F. Chemistry in solution: recent techniques and applications using soft X-ray spectroscopy. *Phys. Chem. Chem. Phys.* **14,** 5331–5338 (2012).

128. Chandler, D., Weeks, J. D. & Anderson, H. C. Van der Waals Picture of Liquids, Solids, and Phase Trasformations. *Science* **220,** 787–794 (1983).

129. Venturi, G. *et al.* Structure of liquid n-hexane. *J. Chem. Phys.* **131,** 034508 (2009).

130. Mondello, M. & Grest, G. S. Molecular dynamics of linear and branched alkanes. *J. Chem. Phys.* **103,** 7156–7165 (1995).

131. Griesbaum, K. *et al.* in *Ullmann's Encyclopedia of Industrial Chemistry* (Wiley-VCH Verlag GmbH & Co. KGaA, 2000). ISBN: 9783527306732.

132. Fuchs, O. *et al.* A liquid flow cell to study the electronic structure of liquids with soft X-rays. *Nucl. Instrum. Methods Phys. Res. A* **585,** 172–177 (2008).

133. Nagasaka, M., Hatsui, T., Horigome, T., Hamamura, Y. & Kosugi, N. Development of a liquid flow cell to measure soft X-ray absorption in transmission mode: A test for liquid water. *J. Electron Spectrosc. Relat. Phenom.* **177,** 130–134 (2010).

134. Jiang, P. *et al.* In situ soft X-ray absorption spectroscopy investigation of electrochemical corrosion of copper in aqueous $NaHCO_3$ solution. *Electrochem. Commun.* **12,** 820–822 (2010).

135. Bambynek, W. *et al.* X-Ray Fluorescence Yields, Auger, and Coster-Kronig Transition Probabilities. *Rev. Mod. Phys.* **44,** 716–813 (1972).

136. Krause, M. O. Atomic Radiative and Radiationless Yields for K and L Shells. *J. Phys. Chem. Ref. Data* **8,** 307–327 (1979).

137. Pfaff, J., Begemann, M. H. & Saykally, R. J. An investigation of the laser optogalvanic effect for atoms and molecules in recombination-limited plasmas. *Mol. Phys.* **52,** 541–566 (1984).

138. Begemann, M. H. & Saykally, R. J. Color center laser optogalvanic spectroscopy of lithium, barium, neon and argon Rydberg states in hollow cathode discharges. *Opt. Commun.* **40,** 277–282 (1982).

139. Bekker, H. *et al. GROMACS: A parallel computer for molecular dynamics simulations* in *Physics Computing* **92** (World Scientific publishing company, Singapore, 1993), 252–256.

140. Berendsen, H. J. C., van der Spoel, D. & van Drunen, R. GROMACS: A message-passing parallel molecular dynamics implementation. *Comput. Phys. Commun.* **91,** 43–56 (1995).

141. Lindahl, E., Hess, B. & van der Spoel, D. GROMACS 3.0: a package for molecular simulation and trajectory analysis. English. *Mol. Model. Annu.* **7,** 306–317 (2001).

142. Van Der Spoel, D. *et al.* GROMACS: Fast, flexible, and free. *J. Comput. Chem.* **26,** 1701–1718 (2005).

143. Hess, B., Kutzner, C., van der Spoel, D. & Lindahl, E. GROMACS 4: Algorithms for Highly Efficient, Load-Balanced, and Scalable Molecular Simulation. *J. Chem. Theory. Comput.* **4,** 435–447 (2008).

144. Jorgensen, W. L., Maxwell, D. S. & Tirado-Rives, J. Development and Testing of the OPLS All-Atom Force Field on Conformational Energetics and Properties of Organic Liquids. *J. Am. Chem. Soc.* **118,** 11225–11236 (1996).

145. Kaminski, G. A., Friesner, R. A., Tirado-Rives, J. & Jorgensen, W. L. Evaluation and Reparametrization of the OPLS-AA Force Field for Proteins via Comparison with Accurate Quantum Chemical Calculations on Peptides. *J. Phys. Chem. B* **105,** 6474–6487 (2001).

146. Price, M. L. P., Ostrovsky, D. & Jorgensen, W. L. Gas-phase and liquid-state properties of esters, nitriles, and nitro compounds with the OPLS-AA force field. *J. Comput. Chem.* **22,** 1340–1352 (2001).

147. Siu, S. W. I., Pluhackova, K. & Bockmann, R. A. Optimization of the OPLS-AA Force Field for Long Hydrocarbons. *J. Chem. Theory. Comput.* **8,** 1459–1470 (2012).

148. Prendergast, D. & Galli, G. X-Ray Absorption Spectra of Water from First Principles Calculations. *Phys. Rev. Lett.* **96,** 215502 (2006).

149. Giannozzi, P. *et al.* QUANTUM ESPRESSO: a modular and open-source software project for quantum simulations of materials. *J. Phys. Condens. Matter* **21,** 395502 (2009).

150. Perdew, J. P., Burke, K. & Ernzerhof, M. Generalized Gradient Approximation Made Simple. *Phys. Rev. Lett.* **77,** 3865–3868 (1996).

151. Momma, K. & Izumi, F. VESTA: a three-dimensional visualization system for electronic and structural analysis. *J. Appl. Crystallogr.* **41,** 653–658 (2008).

152. Rayleigh, L. On The Instability Of Jets. *Proc. London Math. Soc.* **10,** 4–13 (1878).

153. Rayleigh, L. XVI. On the instability of a cylinder of viscous liquid under capillary force. *Philos. Mag. Ser. 5* **34,** 145–154 (1892).

154. Cappa, C. D. *et al.* Effects of alkali metal halide salts on the hydrogen bond network of liquid water. *J. Phys. Chem. B* **109,** 7046–52 (2005).

155. Guo, J. H. *et al.* Molecular Structure of Alcohol-Water Mixtures. *Phys. Rev. Lett.* **91,** 157401 (2003).

156. Kashtanov, S. *et al.* Chemical and electronic structures of liquid methanol from x-ray emission spectroscopy and density functional theory. *Phys. Rev. B* **71,** 104205 (2005).

157. Sun, H. COMPASS: An ab Initio Force-Field Optimized for Condensed-Phase Applications s Overview with Details on Alkane and Benzene Compounds. *J. Phys. Chem. B* **102,** 7338–7364 (1998).

158. Jorgensen, W. L., Madura, J. D. & Swenson, C. J. Optimized Intermolecular Potential Functions for Liquid Hydrocarbons. *J. Am. Chem. Soc.* **106,** 6638–6646 (1984).

159. Mutoru, J. W., Smith, W., O'Hern, C. S. & Firoozabadi, A. Molecular dynamics simulations of diffusion and clustering along critical isotherms of medium-chain n-alkanes. *J. Chem. Phys.* **138,** 024317 (2013).

160. Wilson, K. R. *et al.* X-ray absorption spectroscopy of liquid methanol microjets: bulk electronic structure and hydrogen bonding network. *J. Phys. Chem. B* **109,** 10194–203 (2005).

161. Lama, R. F. & Lu, B. C. Y. Excess Thermodynamic Properties of Aqueous Alcohol Solutions. *J. Chem. Eng. Data* **10,** 216–219 (1965).

162. Chowdhuri, S. & Chandra, A. Dynamics of ionic and hydrophobic solutes in water-methanol mixtures of varying composition. *J. Chem. Phys.* **123,** 234501 (2005).

163. Behrends, R., Fuchs, K., Kaatze, U., Hayashi, Y. & Feldman, Y. Dielectric properties of glycerol/water mixtures at temperatures between 10 and 50 degrees C. *J. Chem. Phys.* **124,** 144512 (2006).

164. Day, T. J. F. & Patey, G. N. Ion solvation dynamics in water-methanol and water-dimethylsulfoxide mixtures. *J. Chem. Phys.* **110,** 10937 (1999).

165. Hsieh, W. P. & Chien, Y. H. High pressure Raman spectroscopy of H_2O-CH_3OH mixtures. *Sci. Rep.* **5,** 8532 (2015).

166. Matsumoto, M., Takaoka, Y. & Kataoka, Y. Liquid-vapor interface of water-methanol mixture. I. Computer simulation. *J. Chem. Phys.* **98,** 1464 (1993).

167. Meng, E. C. & Kollman, P. A. Molecular Dynamics Studies of the Properties of Water around Simple Organic Solutes. *J. Phys. Chem.* **100,** 11460–11470 (1996).

168. Ono, T. *et al.* Dynamic properties of methanol–water mixtures at the temperatures up to 476.2 K and at high pressures via molecular dynamics simulation. *Fluid Phase Equilib.* **420,** 30–35 (2016).

169. Teorica, F., Messina, U., Haughney, M., Mcdonald, I. R. & Klein, M. L. Molecular-dynamics simulation of aqueous mixtures : Methanol, acetone, and ammonia. *J. Chem. Phys.* **93,** 5156–5166 (1990).

170. Mallamace, F. *et al.* Dynamical properties of water-methanol solutions. *J. Chem. Phys.* **144,** 064506 (2016).

171. Ono, T. *et al.* Measurements and correlations of density and viscosity for short chain (C1–C3) n-alcohol–water mixtures in the temperature range from 350.7K to 476.2K at pressures up to 40MPa. *Fluid Phase Equilib.* **407,** 198–208 (2016).

172. Ghoufi, A., Artzner, F. & Malfreyt, P. Physical Properties and Hydrogen-Bonding Network of Water–Ethanol Mixtures from Molecular Dynamics Simulations. *J. Phys. Chem. B* **120,** 793–802 (2016).

173. Pascal, T. A. & Goddard, W. A. Hydrophobic Segregation, Phase Transitions and the Anomalous Thermodynamics of Water/Methanol Mixtures. *J. Phys. Chem. B* **116,** 13905–13912 (2012).

174. Allison, S., Fox, J., Hargreaves, R. & Bates, S. Clustering and microimmiscibility in alcohol-water mixtures: Evidence from molecular-dynamics simulations. *Phys. Rev. B* **71,** 024201 (2005).

175. Benson, S. P. & Pleiss, J. Incomplete mixing versus clathrate-like structures: A molecular view on hydrophobicity in methanol–water mixtures. *J. Mol. Model.* **19,** 3427–3436 (2013).

176. Matisz, G., Kelterer, A. M., Fabian, W. M. F. & Kunsagi-Mate, S. Structural properties of methanol-water binary mixtures within the quantum cluster equilibrium model. *Phys. Chem. Chem. Phys.* **17,** 8467–8479 (2015).

177. Palinkas, G., Hawlicka, E. & Heinzinger, K. Molecular dynamics simulations of water-methanol mixtures. *Chem. Phys.* **158,** 65–76 (1991).

178. Wakisaka, A., Abdoul-Carime, H., Yamamoto, Y. & Kiyozumi, Y. Non-ideality of binary mixtures Water-methanol and water-acetonitrile from the viewpoint of clustering structure. *J. Chem. Soc., Faraday Trans.* **94,** 369–374 (1998).

179. Woods, K. N. & Wiedemann, H. The influence of chain dynamics on the far-infrared spectrum of liquid methanol. *J. Chem. Phys.* **123,** 134507 (2005).

180. Micali, N., Trusso, S., Vasi, C., Blaudez, D. & Mallamace, F. Dynamical properties of water-methanol solutions studied by depolarized Rayleigh scattering. *Phys. Rev. E* **54,** 1720–1724 (1996).

181. Dixit, S., Crain, J., Poon, W. C. K., Finney, J. L. & Soper, A. K. Molecular segregation observed in a concentrated alcohol-water solution. *Nature* **416,** 829–32 (2002).

182. Dougan, L. *et al.* Methanol-water solutions: a bi-percolating liquid mixture. *J. Chem. Phys.* **121,** 6456–62 (2004).

183. Soper, A. K., Dougan, L., Crain, J. & Finney, J. L. Excess entropy in alcohol-water solutions: a simple clustering explanation. *J. Phys. Chem. B* **110,** 3472–6 (2006).

184. Soper, A. K. & Finney, J. L. Hydration of methanol in aqueous solution. *Phys. Rev. Lett.* **71,** 4346–4349 (1993).

185. Nishi, N. *et al.* Hydrogen-Bonded Cluster Formation and Hydrophobic Solute Association in Aqueous Solutions of Ethanol. *J. Phys. Chem.* **99,** 462–468 (1995).

186. Bako, I., Jedlovszky, P. & Palinkas, G. Molecular clusters in liquid methanol: a Reverse Monte Carlo study. *J. Mol. Liq.* **87,** 243–254 (2000).

187. Nagasaka, M., Mochizuki, K., Leloup, V. & Kosugi, N. Local Structures of Methanol–Water Binary Solutions Studied by Soft X-ray Absorption Spectroscopy. *J. Phys. Chem. B* **118,** 4388–4396 (2014).

188. Sato, T., Chiba, A. & Nozaki, R. Composition-dependent dynamical structures of 1-propanol–water mixtures determined by dynamical dielectric properties. *J. Chem. Phys.* **113,** 9748 (2000).

189. Sato, T., Chiba, A. & Nozaki, R. Hydrophobic hydration and molecular association in methanol–water mixtures studied by microwave dielectric analysis. *J. Chem. Phys.* **112,** 2924 (2000).

190. Sato, T. & Buchner, R. The cooperative dynamics of the H-bond system in 2-propanol/water mixtures: Steric hindrance effects of nonpolar head group. *J. Chem. Phys.* **119,** 10789 (2003).

191. Sato, T., Chiba, A. & Nozaki, R. Dynamical aspects of mixing schemes in ethanol–water mixtures in terms of the excess partial molar activation free energy, enthalpy, and entropy of the dielectric relaxation process. *J. Chem. Phys.* **110,** 2508 (1999).

192. Corsaro, C. *et al.* Clustering Dynamics in Water/Methanol Mixtures: A Nuclear Magnetic Resonance Study at 205 K $<$ T $<$ 295 K. *J. Phys. Chem. B* **112,** 10449–10454 (2008).

193. Ishihara, Y., Okouchi, S. & Uedaira, H. Dynamics of hydration of alcohols and diols in aqueous solutions. *J. Chem. Soc., Faraday Trans.* **93,** 3337–3342 (1997).

194. Rankin, D. M., Ben-Amotz, D., van der Post, S. T. & Bakker, H. J. Contacts Between Alcohols in Water Are Random Rather than Hydrophobic. *J. Phys. Chem. Lett.* **6,** 688–692 (2015).

195. Perera, P. N. *et al.* Observation of water dangling OH bonds around dissolved nonpolar groups. *Proc. Natl. Acad. Sci. U. S. A.* **106,** 12230–12234 (2009).

196. Rezus, Y. L. A. & Bakker, H. J. Observation of Immobilized Water Molecules around Hydrophobic Groups. *Phys. Rev. Lett.* **99,** 148301 (2007).

197. Fileti, E. E., Chaudhuri, P. & Canuto, S. Relative strength of hydrogen bond interaction in alcohol–water complexes. *Chem. Phys. Lett.* **400,** 494–499 (2004).

198. Reddy, S. K. & Balasubramanian, S. Carbonic acid: molecule, crystal and aqueous solution. *Chem. Commun.* **50,** 503–514 (2014).

199. Terlouw, J. K., Lebrilla, C. B. & Schwarz, H. Thermolysis of NH_4HCO_3–A Simple Route to the Formation of Free Carbonic Acid (H_2CO_3) in the Gas Phase. *Angew. Chem. Int. Ed. Engl.* **26,** 354–355 (1987).

200. Mori, T., Suma, K., Sumiyoshi, Y. & Endo, Y. Spectroscopic detection of isolated carbonic acid. *J. Chem. Phys.* **130,** 204308 (2009).

201. Mori, T., Suma, K., Sumiyoshi, Y. & Endo, Y. Spectroscopic detection of the most stable carbonic acid, cis-cis H_2CO_3. *J. Chem. Phys.* **134,** 044319 (2011).

202. Moore, M. H. & Khanna, R. K. Infrared and mass spectral studies of proton irradiated $H_2O + CO_2$ ice: Evidence for carbonic acid. *Spectrochim. Acta A: Mol. Spectrosc.* **47,** 255–262 (1991).

203. Moore, M. H., Khanna, R. & Donn, B. Studies of proton irradiated $H_2O + CO_2$ and $H_2O + CO$ ices and analysis of synthesized molecules. *J. Geophys. Res. Planets* **96,** 17541–17545 (1991).

204. Hage, W., Hallbrucker, A. & Mayer, E. Carbonic acid: synthesis by protonation of bicarbonate and FTIR spectroscopic characterization via a new cryogenic technique. *J. Am. Chem. Soc.* **115,** 8427–8431 (1993).

205. Hage, W., Liedl, K. R., Hallbrucker, A. & Mayer, E. Carbonic acid in the gas phase and its astrophysical relevance. *Science* **279,** 1332–1335 (1998).

206. Bernard, J., Huber, R. G., Liedl, K. R., Grothe, H. & Loerting, T. Matrix Isolation Studies of Carbonic Acid–The Vapor Phase above the β-Polymorph. *J. Am. Chem. Soc.* **135,** 7732–7737 (2013).

207. Yamabe, S. & Kawagishi, N. A computational study on the relationship between formation and electrolytic dissociation of carbonic acid. English. *Theor. Chem. Acc.* **130,** 909–918 (2011).

208. Gallet, G. A., Pietrucci, F. & Andreoni, W. Bridging Static and Dynamical Descriptions of Chemical Reactions: An ab Initio Study of CO_2 Interacting with Water Molecules. *J. Chem. Theory. Comput.* **8,** 4029–4039 (2012).

209. Galib, M. & Hanna, G. Mechanistic Insights into the Dissociation and Decomposition of Carbonic Acid in Water via the Hydroxide Route: An Ab Initio Metadynamics Study. *J. Phys. Chem. B* **115,** 15024–15035 (2011).

210. Sham, T. K., Yang, B. X., Kirz, J. & Tse, J. S. K-edge near-edge x-ray-absorption fine structure of oxygen- and carbon-containing molecules in the gas phase. *Phys. Rev. A* **40,** 652–669 (1989).

211. Bader, M., Hillert, B., Puschmann, A., Haase, J. & Bradshaw, A. M. Surface Carbonate on Ag{110}: an X-Ray Absorption Fine-Structure Study. *EPL (Europhysics Lett.)* **5,** 443 (1988).

212. Brandes, J. A., Wirick, S. & Jacobsen, C. Carbon K-edge spectra of carbonate minerals. *J. Synchrotron Radiat.* **17,** 676–682 (2010).

213. Horikawa, Y. *et al.* The electronic structure of carbonate ion in aqueous solution studied by soft X-ray emission spectroscopy. *J. Mol. Liq.* **189,** 9–12 (2014).

214. Case, D. A. *et al. Amber 9* (San Francisco, 2006).

215. Kumar, P. P., Kalinichev, A. G. & Kirkpatrick, R. J. Hydrogen-Bonding Structure and Dynamics of Aqueous Carbonate Species from Car-Parrinello Molecular Dynamics Simulations. *J. Phys. Chem. B* **113,** 794–802 (2008).

216. England, A. H. *X-ray Spectroscopy and Pulse Radiolysis of Aqueous Solutions* English. PhD thesis (Ann Arbor, 2011), 95. ISBN: 9781267227928.

217. Rustad, J. R., Nelmes, S. L., Jackson, V. E. & Dixon, D. A. Quantum-Chemical Calculations of Carbon-Isotope Fractionation in CO_2(g), Aqueous Carbonate Species, and Carbonate Minerals. *J. Phys. Chem. A* **112,** 542–555 (2008).

218. Leung, K., Nielsen, I. M. B. & Kurtz, I. Ab Initio Molecular Dynamics Study of Carbon Dioxide and Bicarbonate Hydration and the Nucleophilic Attack of Hydroxide on CO_2. *J. Phys. Chem. B* **111,** 4453–4459 (2007).

219. Kikeri, D., Zeidel, M. L., Ballermann, B. J., Brenner, B. M. & Hebert, S. C. pH regulation and response to AVP in A10 cells differ markedly in the presence vs. absence of CO_2-HCO_3^-. *Am. J. Physiol.* **259,** C471–C483 (1990).

220. Abe, Y., Iizuka, A., Nagasawa, H., Yamasaki, A. & Yanagisawa, Y. Dissolution rates of alkaline rocks by carbonic acid: Influence of solid/liquid ratio, temperature, and CO_2 pressure. *Chem. Eng. Res. Des.* **91,** 933–941 (2013).

221. Dash, R. K. & Bassingthwaighte, J. B. Simultaneous Blood–Tissue Exchange of Oxygen, Carbon Dioxide, Bicarbonate, and Hydrogen Ion. English. *Ann. Biomed. Eng.* **34,** 1129–1148 (2006).

222. Maher, K. & Chamberlain, C. P. Hydrologic Regulation of Chemical Weathering and the Geologic Carbon Cycle. *Science* **343,** 1502–1504 (2014).

223. Garcia-Rios, M., Cama, J., Luquot, L. & Soler, J. M. Interaction between CO_2-rich sulfate solutions and carbonate reservoir rocks from atmospheric to supercritical CO_2 conditions: Experiments and modeling. *Chem. Geol.* **383,** 107–122 (2014).

224. Choi, Y.-S., Nesic, S. & Young, D. Effect of Impurities on the Corrosion Behavior of CO_2 Transmission Pipeline Steel in Supercritical CO_2–Water Environments. *Environ. Sci. Technol.* **44,** 9233–9238 (2010).

225. Haugan, P. M. & Drange, H. Effects of CO_2 on the ocean environment. *Energy Convers. Manage.* **37,** 1019–1022 (1996).

226. Hoegh-Guldberg, O. *et al.* Coral Reefs Under Rapid Climate Change and Ocean Acidification. *Science* **318,** 1737–1742 (2007).

227. Orr, J. C. *et al.* Anthropogenic ocean acidification over the twenty-first century and its impact on calcifying organisms. *Nature* **437,** 681–686 (2005).

228. Caldeira, K. & Wickett, M. Oceanography: Anthropogenic carbon and ocean pH. *Nature* **425,** 365 (2003).

229. Buytendyk, F. J. J., Brinkman, R. & Mook, H. W. A Study of the System Carbonic Acid, Carbon Dioxide and Water. *Biochem. J.* **21,** 576–584 (1927).

230. Soli, A. L. & Byrne, R. H. CO_2 system hydration and dehydration kinetics and the equilibrium CO_2/H_2CO_3 ratio in aqueous NaCl solution. *Mar. Chem.* **78,** 65–73 (2002).

231. Pocker, Y. & Bjorkquist, D. W. Stopped-flow studies of carbon dioxide hydration and bicarbonate dehydration in water and water-d2. Acid-base and metal ion catalysis. *J. Am. Chem. Soc.* **99,** 6537–6543 (1977).

232. Abbott, T. M., Buchanan, G. W., Kruus, P. & Lee, K. C. 13C nuclear magnetic resonance and Raman investigations of aqueous carbon dioxide systems. *Can. J. Chem.* **60,** 1000–1006 (1982).

233. Baltrusaitis, J. & Grassian, V. H. Carbonic Acid Formation from Reaction of Carbon Dioxide and Water Coordinated to Al(OH)3: A Quantum Chemical Study. *J. Phys. Chem. A* **114,** 2350–2356 (2010).

234. Tautermann, C. S. *et al.* Towards the Experimental Decomposition Rate of Carbonic Acid (H_2CO_3) in Aqueous Solution. *Chemistry* **8,** 66–73 (2002).

235. Patel, R. C., Boe, R. J. & Atkinson, G. The CO_2-water system. I. Study of the slower hydration-dehydration step. English. *J. Solut. Chem.* **2,** 357–372 (1973).

236. Peterson, K. I. & Klemperer, W. Structure and internal rotation of H_2O–CO_2, HDO–CO_2, and D_2O–CO_2 van der Waals complexes. *J. Chem. Phys.* **80,** 2439 (1984).

237. Stirling, A. HCO_3^- Formation from CO_2 at High pH: Ab Initio Molecular Dynamics Study. *J. Phys. Chem. B* **115,** 14683–14687 (2011).

238. In Het Panhuis, M., Patterson, C. H. & Lynden-Bell, R. M. A molecular dynamics study of carbon dioxide in water: diffusion, structure and thermodynamics. *Mol. Phys.* **94,** 963–972 (1998).

239. Moin, S. T. *et al.* Carbon dioxide in aqueous environment–A quantum mechanical charge field molecular dynamics study. *Int. J. Quantum Chem.* **111,** 1370–1378 (2011).

240. Moin, S. T., Weiss, A. K. H. & Rode, B. M. Ionized CO_2 and SO_2 in aqueous environment: Ab initio QMCF-MD studies. *Comput. Theor. Chem.* **1034,** 85–93 (2014).

241. Vchirawongkwin, V., Pribil, A. B. & Rode, B. M. Ab Initio quantum mechanical charge field study of hydrated bicarbonate ion: Structural and dynamical properties. *J. Comput. Chem.* **31,** 249–257 (2010).

242. Prakash, M., Subramanian, V. & Gadre, S. R. Stepwise Hydration of Protonated Carbonic Acid: A Theoretical Study. *J. Phys. Chem. A* **113,** 12260–12275 (2009).

243. Vanderbilt, D. Soft self-consistent pseudopotentials in a generalized eigenvalue formalism. *Phys. Rev. B* **41,** 7892–7895 (1990).

244. Humphrey, W., Dalke, A. & Schulten, K. VMD: Visual molecular dynamics. *J. Mol. Graph.* **14,** 33–38 (1996).

245. Sreenivasulu, B., Gayatri, D. V., Sreedhar, I. & Raghavan, K. V. A journey into the process and engineering aspects of carbon capture technologies. *Renewable and Sustainable Energy Rev.* **41,** 1324–1350 (2015).

246. Cameron, F. K. & Seidell, A. Solubility of Calcium Carbonate in Aqueous Solutions of Certain Electrolytes in Equilibrium with Atmospheric Air. *J. Phys. Chem.* **6,** 50–56 (1902).

247. Garand, E. *et al.* Infrared Spectroscopy of Hydrated Bicarbonate Anion Clusters: $HCO_3^-(H_2O)_{1-10}$. *J. Am. Chem. Soc.* **132,** 849–856 (2009).

248. G. Capewell, S., Buchner, R., Hefter, G. & M. May, P. Dielectric relaxation of aqueous Na_2CO_3 solutions. *Phys. Chem. Chem. Phys.* **1,** 1933–1937 (1999).

249. Nguyen, M. T. *et al.* Mechanism of the Hydration of Carbon Dioxide: Direct Participation of H_2O versus Microsolvation. *J. Phys. Chem. A* **112,** 10386–10398 (2008).

250. Wang, B. & Cao, Z. How water molecules modulate the hydration of CO_2 in water solution: Insight from the cluster-continuum model calculations. *J. Comput. Chem.* **34,** 372–378 (2013).

251. Ottosson, N., Faubel, M., Bradforth, S. E., Jungwirth, P. & Winter, B. Photoelectron spectroscopy of liquid water and aqueous solution: Electron effective attenuation lengths and emission-angle anisotropy. *J. Electron Spectrosc. Relat. Phenom.* **177,** 60–70 (2010).

252. Siegbahn, H. Electron spectroscopy for chemical analysis of liquids and solutions. *J. Phys. Chem.* **89,** 897–909 (1985).

253. Ghosal, S. *et al.* Electron spectroscopy of aqueous solution interfaces reveals surface enhancement of halides. *Science* **307,** 563–6 (2005).

254. Brown, M. A., Winter, B., Faubel, M. & Hemminger, J. C. Spatial Distribution of Nitrate and Nitrite Anions at the Liquid/Vapor Interface of Aqueous Solutions. *J. Am. Chem. Soc.* **131,** 8354–8355 (2009).

255. Margarella, A. M. *et al.* Dissociation of Sulfuric Acid in Aqueous Solution: Determination of the Photoelectron Spectral Fingerprints of H_2SO_4, HSO_4^-, and SO_4^{2-} in Water. *J. Phys. Chem. C* **117,** 8131–8137 (2013).

256. Perrine, K. A. *et al.* Characterization of the Acetonitrile Aqueous Solution/Vapor Interface by Liquid-Jet X-ray Photoelectron Spectroscopy. *J. Phys. Chem. C* **118,** 29378–29388 (2014).

257. Werner, J. *et al.* Surface Behavior of Hydrated Guanidinium and Ammonium Ions: A Comparative Study by Photoelectron Spectroscopy and Molecular Dynamics. *J. Phys. Chem. B* **118,** 7119–7127 (2014).

258. Brown, M. A., Lee, M.-T., Kleibert, A., Ammann, M. & Giorgi, J. B. Ion Spatial Distributions at the Air– and Vacuum–Aqueous K_2CO_3 Interfaces. *J. Phys. Chem. C* **119,** 4976–4982 (2015).

259. Bluhm, H. *et al.* Soft X-ray microscopy and spectroscopy at the molecular environmental science beamline at the Advanced Light Source. *J. Electron Spectrosc. Relat. Phenom.* **150,** 86–104 (2006).

260. Winter, B. *et al.* Full Valence Band Photoemission from Liquid Water Using EUV Synchrotron Radiation. *J. Phys. Chem. A* **108,** 2625–2632 (2004).

261. Onsager, L. & Samaras, N. N. T. The Surface Tension of Debye-Hückel Electrolytes. *J. Chem. Phys.* **2,** 528 (1934).

262. Conway, B. The state of water and hydrated ions at interfaces. *Adv. Colloid Interface Sci.* **8,** 91–211 (1977).

263. Weissenborn, P. K. & Pugh, R. J. Surface Tension of Aqueous Solutions of Electrolytes: Relationship with Ion Hydration, Oxygen Solubility, and Bubble Coalescence. *J. Colloid Interface Sci.* **184,** 550–563 (1996).

264. Jungwirth, P. & Tobias, D. J. Ions at the Air/Water Interface. *J. Phys. Chem. B* **106,** 6361–6373 (2002).

265. Jungwirth, P. & Tobias, D. J. Specific Ion Effects at the Air/Water Interface. *Chem. Rev.* **106,** 1259–1281 (2006).

266. Petersen, P. B. & Saykally, R. J. Probing the Interfacial Structure of Aqueous Electrolytes with Femtosecond Second Harmonic Generation Spectroscopy. *J. Phys. Chem. B* **110,** 14060–14073 (2006).

267. Rizzuto, A. M., Irgen-Gioro, S., Eftekhari-Bafrooei, A. & Saykally, R. J. Broadband Deep UV Spectra of Interfacial Aqueous Iodide. *J. Phys. Chem. Lett.* **7,** 3882–3885 (2016).

268. Lewis, T. *et al.* Does Nitric Acid Dissociate at the Aqueous Solution Surface? *J. Phys. Chem. C* **115,** 21183–21190 (2011).

269. Baer, M. D., Tobias, D. J. & Mundy, C. J. Investigation of Interfacial and Bulk Dissociation of HBr, HCl, and HNO_3 Using Density Functional Theory-Based Molecular Dynamics Simulations. *J. Phys. Chem. C* **118,** 29412–29420 (2014).

270. Kett, P. J. N., Casford, M. T. L. & Davies, P. B. Sum Frequency Generation (SFG) Vibrational Spectroscopy of Planar Phosphatidylethanolamine Hybrid Bilayer Membranes under Water. *Langmuir* **26,** 9710–9719 (2010).

271. Rohringer, N. *et al.* Atomic inner-shell X-ray laser at 1.46 nanometres pumped by an X-ray free-electron laser. *Nature* **481,** 488–491 (2012).

272. Bencivenga, F. *et al.* Nonlinear optics with coherent free electron lasers. *Phys. Scr.* **T169,** 014003 (2016).

273. Bencivenga, F. *et al.* Four-wave mixing experiments with extreme ultraviolet transient gratings. *Nature* **520,** 205–208 (2015).

274. Szlachetko, J. *et al.* Establishing nonlinearity thresholds with ultraintense X-ray pulses. *Sci. Rep.* **6,** 33292 (2016).

275. Franken, P. A., Hill, A. E., Peters, C. W. & Weinreich, G. Generation of Optical Harmonics. *Phys. Rev. Lett.* **7,** 118–119 (1961).

276. Eisenthal, K. B. Equilibrium and Dynamic Processes at Interfaces by Second Harmonic and Sum Frequency Generation. *Annu. Rev. Phys. Chem.* **43,** 627–661 (1992).

277. Shen, Y.-R. *Fundamentals of sum-frequency spectroscopy* ISBN: 131647304X (Cambridge University Press, 2016).

278. Wang, H.-F., Gan, W., Lu, R., Rao, Y. & Wu, B.-H. Quantitative spectral and orientational analysis in surface sum frequency generation vibrational spectroscopy (SFG-VS). *Int. Rev. Phys. Chem.* **24,** 191–256 (2005).

279. Allaria, E. *et al.* Highly coherent and stable pulses from the FERMI seeded free-electron laser in the extreme ultraviolet. *Nat. Photonics* **6,** 699–704 (2012).

280. Allaria, E. *et al.* Two-stage seeded soft-X-ray free-electron laser. *Nat. Photonics* **7,** 913–918 (2013).

281. Galayda, J. The new LCLS-II project: Status and challenges. *Linac14, Geneva, Switzerland* (2014).

282. Song, M. *et al.* Wakefields studies for the SXFEL user facility. *Nucl. Sci. Tech.* **28,** 90 (2017).

283. Shwartz, S. *et al.* X-Ray Parametric Down-Conversion in the Langevin Regime. *Physical Review Letters* **109,** 13602 (2012).

284. Simoncig, A. *et al. The EIS beamline at the seeded free-electron laser FERMI* in *Proc. SPIE* (eds Klisnick, A. & Menoni, C. S.) **10243** (2017), 102430L.

285. Masciovecchio, C. *et al.* EIS: the scattering beamline at FERMI. *Journal of Synchrotron Radiation* **22,** 553–564 (2015).

286. Poletto, L. *et al.* Spectrometer for X-ray emission experiments at FERMI free-electron-laser. *Rev. Sci. Instrum.* **85,** 103112 (2014).

287. Sharma, S. & Ambrosch-Draxl, C. Second-Harmonic Optical Response from First Principles. *Phys. Scr.* **T109,** 128 (2004).

288. Gulans, A. *et al.* exciting: a full-potential all-electron package implementing density-functional theory and many-body perturbation theory. *J. Phys. Condens. Matter* **26,** 363202 (2014).

289. Velasco-Velez, J.-J. *et al.* The structure of interfacial water on gold electrodes studied by x-ray absorption spectroscopy. *Science* **346,** 831 LP –834 (2014).

290. Morita, A. & Hynes, J. T. A theoretical analysis of the sum frequency generation spectrum of the water surface. *Chem. Phys.* **258,** 371–390 (2000).

291. Finetti, P. *et al.* Pulse Duration of Seeded Free-Electron Lasers. *Phys. Rev. X* **7,** 21043 (2017).

292. Zangrando, M. *et al.* Recent results of PADReS, the Photon Analysis Delivery and REduction System, from the FERMI FEL commissioning and user operations. *J. Synchrotron Radiat.* **22,** 565–570 (2015).

293. Hohenberg, P. & Kohn, W. Inhomogeneous Electron Gas. *Phys. Rev.* **136,** B864–B871 (1964).

294. Kohn, W. & Sham, L. J. Self-Consistent Equations Including Exchange and Correlation Effects. **140,** A1133–A1138 (1965).

295. Trucano, P. & Chen, R. Structure of graphite by neutron diffraction. *Nature* **258,** 136–137 (1975).

296. Ooi, N., Rairkar, A. & Adams, J. B. Density functional study of graphite bulk and surface properties. *Carbon* **44,** 231–242 (2006).

297. Perdew, J. P. & Zunger, A. Self-interaction correction to density-functional approximations for many-electron systems. *Phys. Rev. B* **23,** 5048–5079 (1981).

298. Klinkusch, S., Saalfrank, P. & Klamroth, T. Laser-induced electron dynamics including photoionization: A heuristic model within time-dependent configuration interaction theory. *J. Chem. Phys.* **131,** 114304 (2009).

299. Sorini, A. P., Kas, J. J., Rehr, J. J., Prange, M. P. & Levine, Z. H. Ab initio calculations of electron inelastic mean free paths and stopping powers. *Phys. Rev. B* **74,** 165111 (2006).

300. Kunz, C. *et al.* Relative electron inelastic mean free paths for diamond and graphite at 8keV and intrinsic contributions to the energy-loss. *J. Electron Spectros. Relat. Phenomena* **173,** 29–39 (2009).

301. Als-Nielsen, J. & McMorrow, D. *Elements of Modern X-ray Physics* (John Wiley & Sons, Inc., Hoboken, NJ, USA, 2011).

302. Bostedt, C. *et al.* Linac Coherent Light Source: The first five years. *Rev. Mod. Phys.* **88,** 15007 (2016).

303. Tkachenko, N. V. *Optical spectroscopy: methods and instrumentations* (Elsevier, 2006).

304. Ghimire, S. *et al.* Nonsequential two-photon absorption from the K shell in solid zirconium. *Phys. Rev. A* **94,** 43418 (2016).

305. Doumy, G. *et al.* Nonlinear Atomic Response to Intense Ultrashort X Rays. *Phys. Rev. Lett.* **106,** 83002 (2011).

306. Hasegawa, H., Takahashi, E. J., Nabekawa, Y., Ishikawa, K. L. & Midorikawa, K. Multiphoton ionization of He by using intense high-order harmonics in the soft-x-ray region. *Phys. Rev. A* **71,** 23407 (2005).

307. Karule, E. On the evaluation of transition matrix elements for multiphoton processes in atomic hydrogen. *J. Phys. B At. Mol. Phys.* **4,** L67–L70 (1971).

308. Klarsfeld, S. Two-photon ionization of atomic hydrogen in the ground state. *Lett. al Nuovo Cim.* **3,** 395–398 (1970).

309. Zernik, W. Two-Photon Ionization of Atomic Hydrogen. *Phys. Rev.* **135,** A51–A57 (1964).

310. Henke, B. L., Gullikson, E. M. & Davis, J. C. X-Ray Interactions: Photoabsorption, Scattering, Transmission, and Reflection at E = 50-30,000 eV, Z = 1-92. *At. Data Nucl. Data Tables* **54,** 181–342 (1993).

311. Jeong, H.-K. *et al.* X-ray absorption spectroscopy of graphite oxide. *EPL* **82,** 67004 (2008).

312. Nagler, B. *et al.* Turning solid aluminium transparent by intense soft X-ray photoionization. *Nat. Phys.* **5,** 693–696 (2009).